Founded 1905

ADVANCED SERVO CONTROL FOR HARD DISK DRIVES IN MOBILE APPLICATIONS

BY

JINGLIANG ZHANG
(BEng, MEng)

A THESIS SUBMITTED

FOR THE DEGREE OF DOCTOR OF PHILOSOPHY

DEPARTMENT OF ELECTRICAL & COMPUTER ENGINEERING
NATIONAL UNIVERSITY OF SINGAPORE

2011

I dedicate this dissertation to my lovely children: Jerry, Jenny and Jessie.

Acknowledgements

I would especially like to thank Professor Shuzhi Sam Ge, my supervisor, for his many suggestions, constant support and guidance throughout this research. I would also like to express my gratitude to Professor Frank Lewis for his kind help.

I express my sincere gratitude to the Data Storage Institute of Singapore for its support of my part-time Ph.D. program.

Of course, I am grateful to my family for their patience and *love*. Without them this work would never have come into existence literally.

Finally, I wish to thank the following colleagues: Linlin Thi (for her patience and hardworking in developing hardware and firmware for the experiment setup together with me), Dr. Chunling Du and Dr. Fan Hong (for the endless chatter about control theory and controller design), Dr. Qingwei Jia (for his friendship and kind support).

Jingliang Zhang

December 27, 2010

Contents

List of Figures

List of Tables

Abstract

This thesis provided solutions to the following three major problems that HDD servo system encountered in the application of mobile consumer devices: acoustic noise and residual vibrations problem induced from track seeking, smooth settling problem during mode-switching, and disturbances rejection problem for high precision tracking accuracy. To reduce the seeking acoustic noise, a pseudo sinusoidal current profile for any seeking span was designed for the 2DOF seeking controller with consideration of driver saturation, and a design method was derived to chose a set of proper values of the parameters for the current profile such that the residual vibrations due to the dominant structural resonances can be minimized. To achieve the smooth and fast settling for dual stage servo systems which are the servo mechanism for next generation high density HDD, a feedforward compensator was proposed based on zero phase error tracking control. This feedforward compensator can be used to cancel the undesired transitions due to the non-zero initial states of VCM actuators, and hence achieve smooth and fast settling while switching from seeking mode to following mode. To achieve better tracking accuracy, an approach combining the KYP lemma together with H_2 optimal method was proposed. This method can be used to shape the sensitivity function of the HDD servo loop to attenuate a few dominant disturbances at a specific frequency range and achieve the minimization of overall track misregistration of the servo system.

Chapter 1

Introduction

1.1 Background of HDD and Magnetic Recording

Magnetic hard disk drives (HDD) are non-volatile random access storage devices which store digitally encoded data on rapidly rotating platters using a motor-driven spindle in a protective enclosure. In 1957, IBM first introduced HDD as a data storage device for IBM accounting computer. With the rapid progresses of magnetic recording related technologies in servo, mechanics, signal processing, magnetic recording physics, media materials, recoding head processing, and tribology, the data storage areal density of HDD has been increasing dramatically at the average compound growth rate of around 60% per year through the 1990's, as shown in Figure 1.1. Today, the areal density has achieved around 400 Gbits/in^2, and the corresponding track density is around 300,000 tracks per inch (TPI), with a data transfer rate of more than 125 MBytes/second. Therefore, the market applications of HDDs have expanded from general purpose computers to most computing applications including a lot of consumer applications, like digital video recorders, digital audio players, personal digital assistants, digital cameras, and video game consoles, etc.

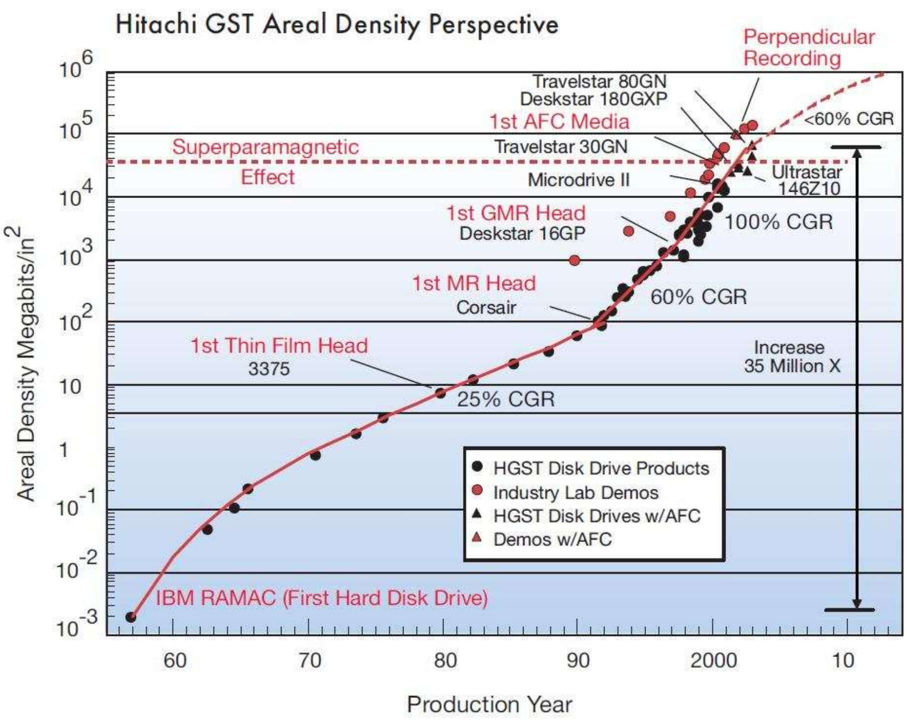

Figure 1.1: Data storage density for disk drives versus time [1].

Areal density, also sometimes called bit density, refers to the amount of data that can be stored in a given amount of hard disk platter. Areal density is a measure of the number of bits that can be stored in a unit of area. It is usually expressed in bits per square inch (BPSI).

Being a two-dimensional measure, areal density is computed as the product of two other one-dimensional density measures:

1. Track density: This is a measure of how tightly the concentric tracks on the disk are packed. It is specified by tracks per inch (TPI), which tells how many tracks can be placed down in one inch of radius on the platters.

2. Linear or recording density: This is a measure of how tightly the bits are packed within a length of track. It is specified by bits per inch (BPI), which tells how many bits can be written along one inch of track.

There are two ways to increase areal density: increase the linear density by packing the bits on each track closer together so that each track holds more data; or increase the track density so that each platter holds more tracks. Typically new generation drives improve both measures. It's important to realize that increasing areal density leads to drives that are not just bigger, but also faster. The reason is that the areal density of the disk impacts both of the key hard disk performance factors: the track to track positioning speed and data transfer rate.

Increasing the areal density of disks is a difficult task that requires many technological advances and changes to various components of the hard disk [2]. As the data is packed closer and closer together, problems result with interference between bits. This is often dealt with by reducing the strength of the magnetic signals stored on the disk, but then this creates other problems such as ensuring that the signals are stable on the disk and that the read/write (R/W) heads are sensitive and close enough to the surface to pick them up. Changes to the media layer on the platters, actuators, control electronics and other components are made to continually improve areal density. Every few years a R/W head technology breakthrough enables a significant jump in density, which is why hard disks have been doubling in size so frequently, as shown in Figure 1.1 .

1.2 Servo Control Issues in HDD

The HDD servo systems play a vital role in the demand of increasingly high track density and high performance HDDs. In HDDs, the servo system provides two major functions: track seeking and track following. The track seeking servo moves R/W head from one track to another in minimal time, which is seeking time. The less the seeking time is, the faster the data can transfer. The track following servo maintains the R/W head position over the center of a target track. The measured deviation of R/W head from the center of the track is called position error signal

(PES). It is the performance of track following servo that limits the achievable track density. The tracking accuracy of HDD servo is often measured by a 3σ number of PES, assuming a Gaussian distribution. This performance measure is also called as track misregistration (TMR). Typical TMR is 12% of the track width, which matches with the off-track-reading-capability (OTRC) of the coding channel. OTRC is a measure of the R/W system's ability to read previously-written data as a function of servo tracking-error, and proximity of an adjacent data-track. If TMR is larger than 12%, the data reading channel will have unrecoverable error. In general, the HDDs have top performance if TMR is less than 5% of track 99.7% of the time.

The track-following control in HDDs is an inherently difficult problem, as the plant is marginally stable and it becomes unstable in the presence of delays due to sampling and computation. Besides this, the HDD servo system is non-collocated, as sensors are placed at the read head while control is applied at the voice-coil-motor (VCM) [3] [4]. Furthermore, the servo system in HDD is non-minimum phase system, which imposes limits on tracking performance [5]. The servo robustness and tracking accuracy are limited by the following factors: (1) resonance and gain variations between heads, at different radius, ages, and temperatures; (2) excessive three-dimensional vibrations; (3) mechanical constraints (e.g. form factor) limit the dynamic properties of the plant, which in turn place limitations on the controller performance; (4) uncertainties, and nonlinearities, such as friction due to near contact recording and pivot, and backlash/hysteresis of micro-actuator/milli-actuator.

Traditionally, HDD servos are designed using linear control theory. Current disk drive utilizes typical linear feedback digital control systems based on error signal, PES. The PES is demodulated from the position information that is encoded onto the disks during the manufacturing process. PID controllers were used initially, and they are subsequently augmented with notch filters to suppress the mechanical resonant modes, thereby increasing the bandwidth. The performances of these methods are limited by the effects of Bode Integral Theorem [6]. As a consequence of this theory, servo loop will amplify vibrations at other frequencies [7], if the servo sensitivity transfer function is designed to reject more vibrations in some frequencies. This is also known as waterbed effect.

Another formidable challenge for track-following controller is to achieve precise tracking accuracy so as to satisfy the requirement for ultra-high track density higher than 500k TPI, despite the presence of uncertainties in the dynamic model. PES demodulation noise in HDD is scaled with signal to noise ratio (SNR) of head and media, and used to be the major TMR sources. However, for high density HDD in mobile applications, disturbances are no longer limited to PES noise, but also disk motion, air flow, and external vibration, etc. Although external sensors, such as accelerometers, can be used in the suppression of external vibrations in order to maintain the tracking accuracy [8] [9] [10] [11], the relationship between XY acceleration and PES may be highly nonlinear, which results in further difficulties in the design of feed forward controllers. In addition, some nonlinearities currently being neglected or simplified in control system design must be taken into account for a system with such a high accuracy requirement. The nonlinearities preventing the system accuracy of a hard disk drive from further improvement include ribbon flexibility and nonlinear friction of the actuator pivot of a HDD [12] [13] [14]. Furthermore, inconsistencies of system parameters between units are prevalent as HDDs are mass-produced products. These parameters vary with age and thermal effects, although the time scales are usually sufficiently large such that they can be considered to be slowly-varying or even time-invariant.

Therefore, the track-following servo controller are designed with two kinds of fundamental trade off, performance trade-off due to bode integration, and performance trade-off with system robustness due to uncertainties of plant dynamic and disturbances. The performance versus robustness trade-off is an important aspect of the development of H_∞ control theory [15] [16]. Many papers are published on the loop-shaping design methods to look for the reasonable trade-off between robustness and performance [17] [18] [19].

A few researchers have investigated the feasibility of applying adaptive or learning algorithms like neural network and fuzzy control. In [20] [21] [22] [23], an adaptive neural network controller is designed to compensate for the pivot nonlinearity. In [24], a model-based adaptive controller is added to a linear time invariant (LTI) stabilizing controller to minimize the tracking error of the read/write head. In [25], an adaptive robust controller was developed, which is applicable to both track-seeking and track-following. In [26] [27] [28] [29], an adaptive notch filter was designed to compensate for the resonant modes with uncertain frequencies. However, most of the adaptive algorithms are not feasible in HDD servo due to either robustness, or degraded performance with existence of noise and disturbances, or the slow convergence of adaptation.

In a traditional HDD servo system, nonlinear controllers such as proximate time-optimal servo (PTOS) [30] [31] [32] are widely used for track-seeking. Other efforts include designing a unified control structure for both track-seeking and following, such as two-degree-of freedom (2DOF) servo mechanism with adaptive robust control and zero phase error tracking techniques [33] [34] [35]. Most of these works focus on reducing seeking and settling time. But for the HDDs application in consumer electronics where the quietness is essential, such as home entertainment system, car navigation and digital video recorder, HDD acoustic noise is one of the key performance indices most concerned. Another challenge for the seeking/settling controller is the residual vibrations induced in the transition switching from seeking to track-following [36] [37] [38]. The residual vibrations are not only one of the significant TMR sources, but may also induce acoustic noise.

1.3 Outline of Chapters

The contributions presented in this dissertation include the following: (1) Proposed an advanced systematic loop shaping method using Kalman-Yakubovic-Popov (KYP) Lemma to optimize the track-following controller with considerations of the spectrum models of input disturbances, output disturbances and sensing noise. The method was experimentally validated in our servo writing platform; (2) Proposed a method to design an optimal seek current profile for the seeking controller to reduce acoustic noise and residual vibrations; (3) Proposed and experimentally validated a novel settling controller for dual-stage servo system to achieve fast and smoothly settling on target track.

The dissertation is organized as follows. In Chapter 2, the mechanical components used in current HDDs are described. It details the possible sources of TMR during normal operation and when the HDD is subjected to external shock and vibrations. It also provides the modeling of the typical VCM actuator, piezoelectric (PZT) micro-actuator, disturbances and noises.

In Chapter 3, the seeking process in HDDs is detailed. We propose a direct approach to design the pseudo-sinusoidal seek current profile, which is able to reduce both the acoustic noise and residual vibrations. With consideration of both current saturation limit and maximum seeking velocity limit, the saturation period, frequency of sinusoidal wave, and coasting time can be optimally designed for arbitrary seeking span to reduce residual vibrations.

In Chapter 4, the dual-stage servo system in HDD is first introduced. We formulate the problem due to the initial values of states in the transition from track-seeking to track-following. After a brief discussion of the conventional initial value compensation (IVC) method, we describe the new proposed method initial error shaping (IES) basing on the zero-phase error tracking (ZPET), followed by the experimental results.

In Chapter 5, a general KYP-method is introduced to shape the sensitivity function and suppress the disturbances at certain frequencies. With the spectrum model of disturbances and noises, an H_2 optimal method is introduced to design an optimal feedback control to achieve overall an optimal tracking performance. A systematic procedure is then presented to design an optimal track-following controller combining KYP-lemma with H_2 optimal control. We introduce the servo loops in the servo writing experimental platform and present experimental results to verify the performances of controller designed with different approaches.

In the final chapter, Chapter 6, the major results and achievements of this research are summarized. Further, a recommendation for future work is also outlined.

Chapter 2

HDD Servo Mechanism and Modeling

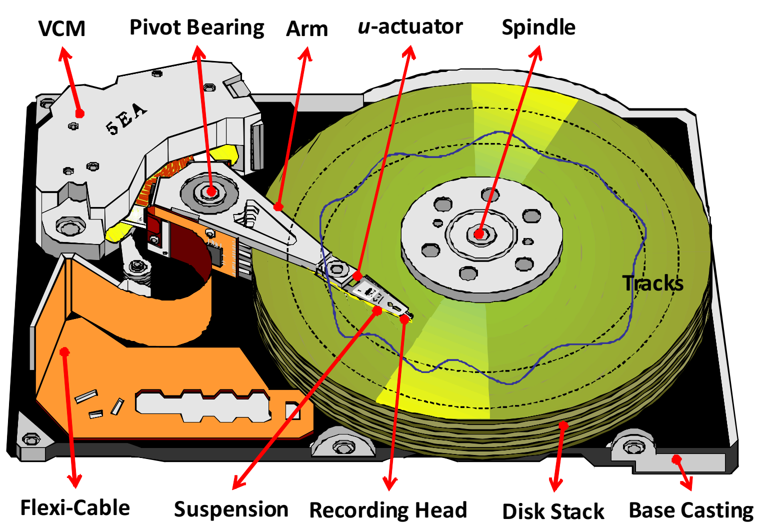

Figure 2.1: The mechanism inside a conventional HDD.

Figure 2.1 shows an overview of the mechanism inside a HDD. The major components in a modern HDD include: 1) device enclosure, which usually consists of a base plate and a cover to provide supports to the spindle, actuator, and electronics card; 2) disk stack assembly, where several disks are stacked on the spindle motor shaft and rotate at up to 15,000 rotations per minute (RPM) in high end 3.5-inch drives and 5,400 - 7,200 RPM in 2.5-inch drives. On the surface of a disk, several hundred thousand data tracks are magnetically recorded, and the latest track pitch is about 80 nm; 3) head stack assembly which contains of a voice coil motor (VCM), actuator arm, suspension and gimbal assembly. A slider is supported by a suspension and a carriage, and is suspended at less than ten nanometers above the disk surface. The VCM actuates the carriage and moves the slider on a desired track. To increase the servo bandwidth to improve positioning accuracy for higher track density drives, dual-stage servo using a suspension-driven PZT microactuator has been commercially applied to HDD; 4) electronics circuit board which involves drivers for spindle motor and VCM, read/write (R/W) electronics, servo channel demodulator, a micro processor/digital signal processor (DSP) for servo control and the interface to host computer. The position signals are recorded magnetically on each disk using a servo track writer (STW). The position signals are recorded in a certain time interval on each track. Consequently, the PES between the head and the reference track center can be detected directly by reading the position signal.

2.1 The Servo Loop in HDD

The head-positioning servomechanism in HDD is a control system that moves the R/W head from current track near to another target track (track-seeking), and re-positions the R/W head over a desired track center with minimum statistical deviation from the track center (track-following). A settling controller is used in between the above seeking and following modes. Figure 2.2 shows the typical functional block diagram where plants involve VCM and PZT actuators for the dual-stage servo system in HDD. The plant dynamics $(P(s) + \Delta P(s))$ include the dynamic of arm, suspension, and driver, and y is the position of R/W head (it is the sum of VCM and PZT output for dual-stage HDD). y_r is the reference input of the desired track center. pes_t is the true PES signal which tells exactly how well the R/W head follows the reference track center. n is measurement noise

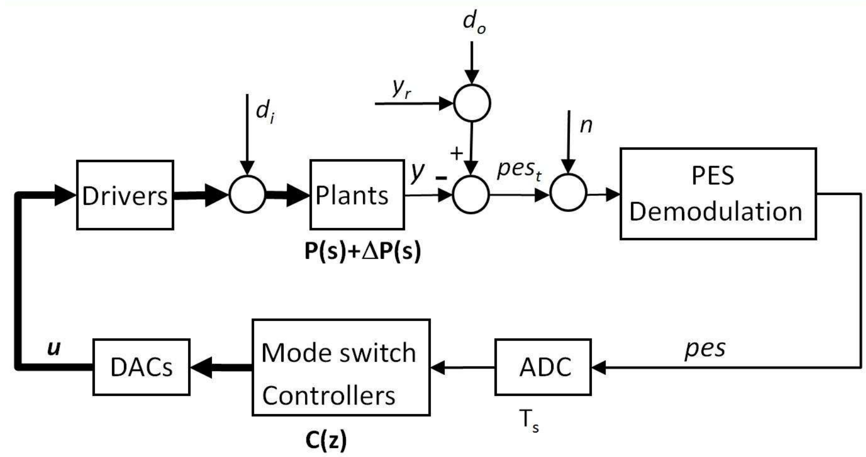

Figure 2.2: A typical servo loop in HDD.

which includes the electronic noise of demodulation circuit, head noise, and media noise. pes is the measured error for feedback control. d_i is the input disturbance which includes torque disturbances and external shock disturbances. d_o is the output disturbance which includes the disk vibrations,slider vibrations, suspension vibrations, and spindle vibrations. T_s is the sampling time, which is decided by the sector number in one revolution and the rotation speed of spindle.

Figure 2.2 shows that the HDD servo has four features:(a) typical error feedback controller (b) sampled digital servo control (c) disturbance suppression control including high servo bandwidth design, and (d) transient response control such as mode-switching control (MSC).

For the single-stage servo in track-following mode, we have

$$pes_t(k) = -P(z)S(z)d_i(k) + S(z)d_o(k) - S(z)P(z)C(z)n(k), \tag{2.1.1}$$

from Figure 2.2. where $P(z)$ is the transfer function of the discretized plant model $P(s)$, $C(z)$ is the track-following controller, and the sensitivity function or error rejection function is given by

$$S(z) = \frac{1}{1 + P(z)C(z)}. \tag{2.1.2}$$

which is shown as in Figure 2.3.

(2.1.1) tells that the servo tracking accuracy ($3\sigma(pes_t)$) is limited by the disturbance rejection capability of sensitivity function and the distribution of disturbances in frequency domain. An improved mechanical design is expected to have less internal structural vibrations and provides the actuator with better dynamic performance. On the other hand, a good closed-loop servo system is expected to be able to reject more disturbances. This typically demands a high servo bandwidth, which requires actuators to be of better dynamic performance. A low hump with amplification of less than 6 dB in error transfer function will also be observed.

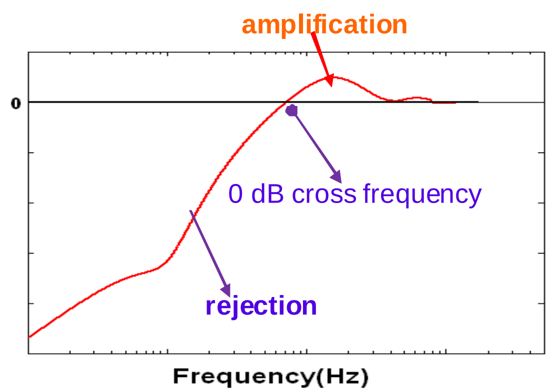

Figure 2.3: The bode plot of a typical sensitivity function.

2.2 Mechanical Structural Resonances

2.2.1 Spindle Motor

The structures of ball bearing and fluid dynamic bearing motors are shown in Figure 2.4 [1]. Fluid dynamic bearing (FDB) motors provide improved acoustics over traditional ball bearing spindle motors. The source of acoustic noise in the HDD is the dynamic motion of the disk and spindle motor components. The sound components are generated from the motor magnet, stator, bearings, and

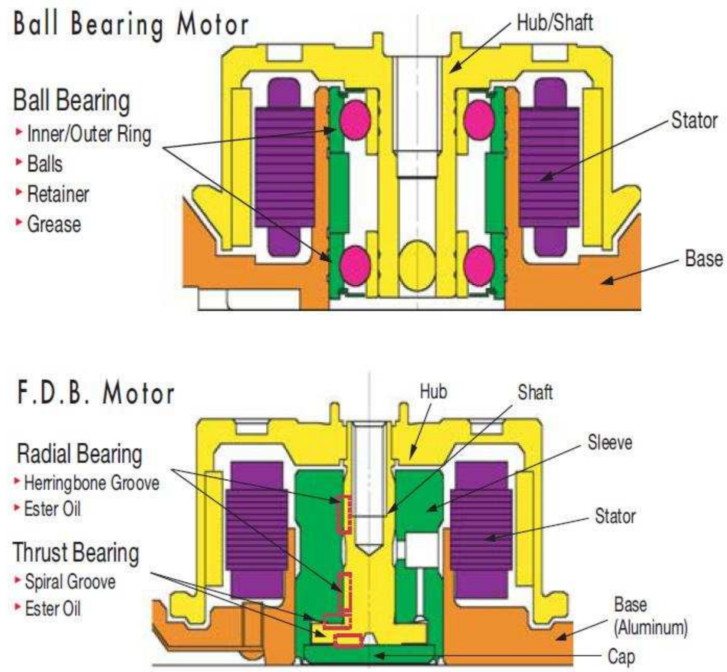

Figure 2.4: The structure of ball bearing and fluid dynamic bearing.

disks. These sound components are all transmitted through the spindle motor to the HDD base casting and top cover. Eliminating the bearing noise by the use of FDB spindle motors reduces one area of the noise component that contributes to acoustic noise. In addition, the damping effect of the lubricant film further attenuates any noise contributed from the spindle motor components. This results in lower acoustic noise from HDDs employing FDB spindle motors. Industrial data has shown a 4 dB or more decrease in idle acoustic noise for some HDD designs [1].

Spindle speed ranges from around 3600 RPM to 15k RPM. A higher RPM causes a higher data transfer rate, but larger vibrations generated by disks and spindle as shown in Figure 2.5.

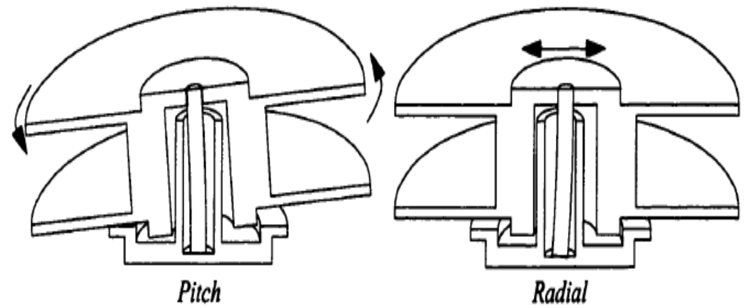

Figure 2.5: The spindle resonant modes: pitch and radial.

2.2.2 Disks Platter

The disk platters have significant mechanical resonant modes which are excited by the turbulent air flow over the disk surface [39]. Many vibration modes exist with its inner diameter clamped. The modes are denoted as (m, n), where m denotes the number of nodal circles and n denotes the number of nodal diameter in the mode [39]. Figure 2.6 shows the typical disk modes shape. Most these modes have a large contribution to the output disturbances d_o [40] [41].

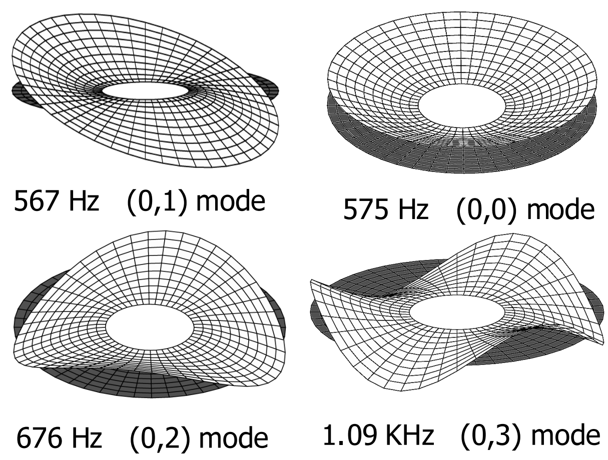

Figure 2.6: The typical eigenmodes of disk.

2.2.3 Suspension and Arm

The arm and suspension are the linkage between VCM (actuation part, control input) and slider (the sensor part, system output). The dynamic modes of suspension and arm make the servo system more non-collocated, thus degrading their performance. Figure 2.7 shows the typical four eigenmodes of suspension. The

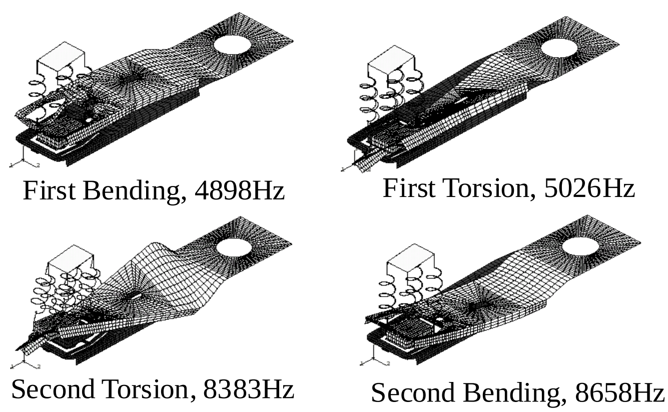

Figure 2.7: The eigenmodes of suspension.

bending mode impacts less on the tracking accuracy as it is out-of-plane. The first torsion mode usually is small in amplitude, but is easily excited by air flow. As such, it has a significant contribution to the out disturbance d_o.

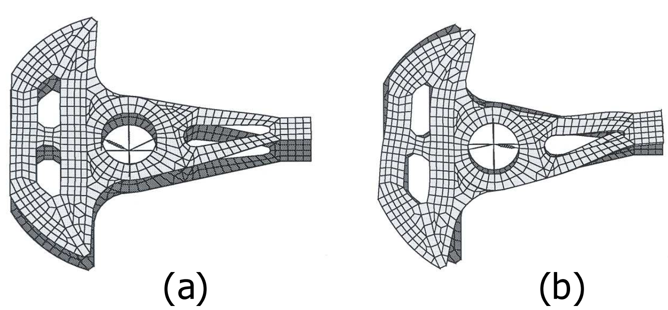

Figure 2.8: The typical arm mode shapes: (a) lateral QR mode and (b) lateral bending mode.

Figure 2.8 shows the typical mode shapes of an arm, the lateral quasi-rigid (QR) body mode at around 5.23 kHz and lateral in-plane bending mode at around 11.5

kHz. QR mode is typically the first mode which limits the servo bandwidth, and it is usually compensated with phase-stable design, notch filters, or active damping [3].

2.3 Modeling of Servo System

2.3.1 Modeling of VCM Actuator

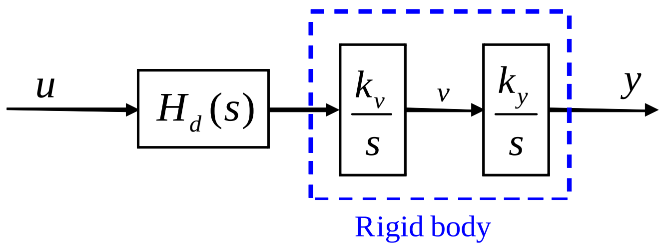

Figure 2.9: The block diagram of VCM model.

The VCM is a rotatory actuator. It contains a coil which is rigidly attached to the actuator arm. The coil is suspended in a magnetic field generated by a pair of permanent magnets. When current passes through the coil, a torque is produced which accelerates the actuator radially inward or outward, depending on the direction of the current. The dynamic of VCM can be modeled as a rigid body model (double integrator) and flexi-body resonances [30], as shown in Figure 2.9. The dynamics of the VCM can be expressed as,

$$y = \frac{k_v k_y}{s^2} H_d(s) u, \tag{2.3.3}$$

$$k_v = K_t/m, \tag{2.3.4}$$

where u is the current input to the actuator. y and v are the displacement and the velocity of the R/W head. k_y is the position measurement gain. m is the actuator mass, and k_t is the torque constant. The resonant modes $H_d(s)$ can be modeled as

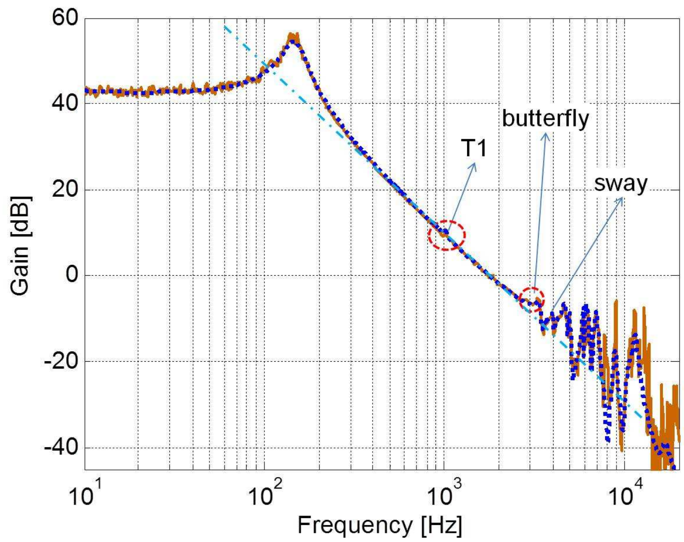

Figure 2.10: Bode plots of frequency response for VCM. (solid line: measured; dotted: identified; dash-dotted: double integrator)

the following transfer function

$$H_d(s) = \sum_{k=1}^{n} \frac{b_{2k}\omega_k s + b_{2k-1}\omega_k^2}{s^2 + 2\xi_k\omega_k s + \omega_k^2}, \tag{2.3.5}$$

which is a parallel combination of n resonances. For typical lightly damped resonance, $0.005 \leq \xi_k \leq 0.05$. Note that, the $H_d(s)$ includes the resonant modes of both the suspension and the arm.

In Figure 2.10, the solid line is the measured frequency response of a VCM actuator. Its deviation from the double-integrator model at low frequencies is due to the nonlinearities of pivot friction. By curve fitting of each resonant mode, one can obtain the parameters of the transfer function as the dotted line shown in Figure 2.10.

2.3.2 Modeling of Micro-actuator

Conventional HDDs with single stage VCM actuator have limits to the tracking accuracy since the source of actuation is the voice coil which is at one end of the

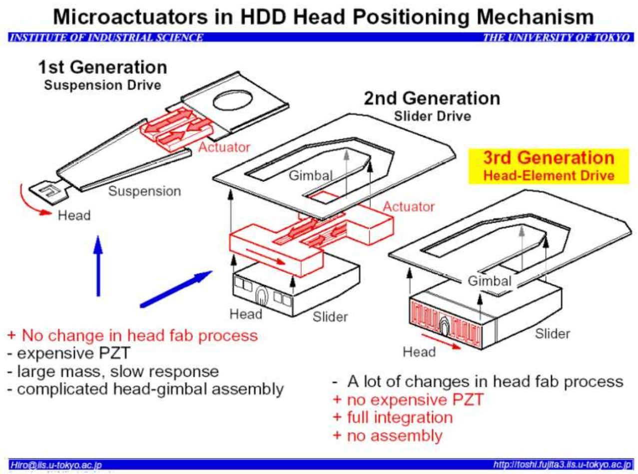

Figure 2.11: The technology evolution for micro-actuator.

actuator, while the magnetic heads are on the other end. This implies a non-collocated system.

Dual stage actuation places a fine positioning actuator close to the recording heads in order to complement the coarse motion of the voice coil using smaller motion closer to the recording head. The secondary actuator typically uses piezoelectric devices that move the heads across a narrow range in order to provide higher precision motion control and offer a higher track density than that is achievable using a single stage actuator.

As shown in Figure 2.11, there are three major popular types of micro-actuator [42]. They are suspension-driven (first generation), slider-driven (2^{nd} generation), and head-driven micro-actuator (3^{rd} generation). But the 2^{nd} generation needs complicated head-gimbal assembly (HGA) and 3^{rd} generation needs a lot of changes in head fabrication process. At present, only the first generation is commercially used in HDDs. For example, Seagate released the first commercial drive (Cheetah 10K7) with suspension-driven micro-actuator as shown in Figure 2.12.

A piezoelectric-based microactuator located on the suspension as shown in Figure 2.13 is considered in this section. The mechanical operation of the microactuator

Figure 2.12: The dual-stage actuator inside Seagate Cheetah 10K7 HDD.

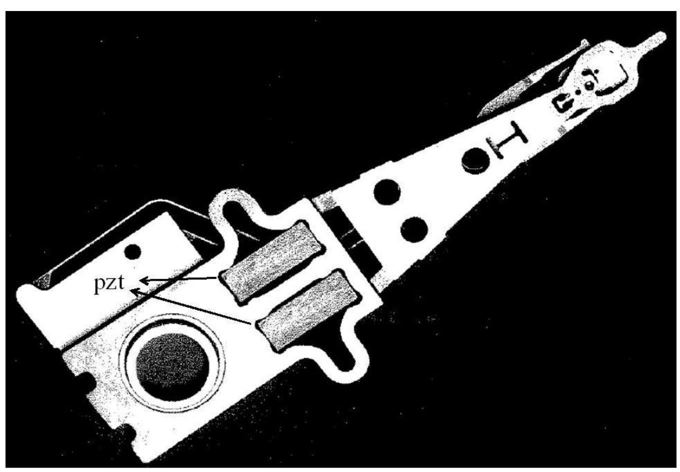

Figure 2.13: A PZT actuated suspension.

can be understood via an equivalent spring-mass system. The compliance of the base plate is simplified as a single spring K_b, and the compliance of the flex hinge elements is simplified as a single rotational spring K_r.

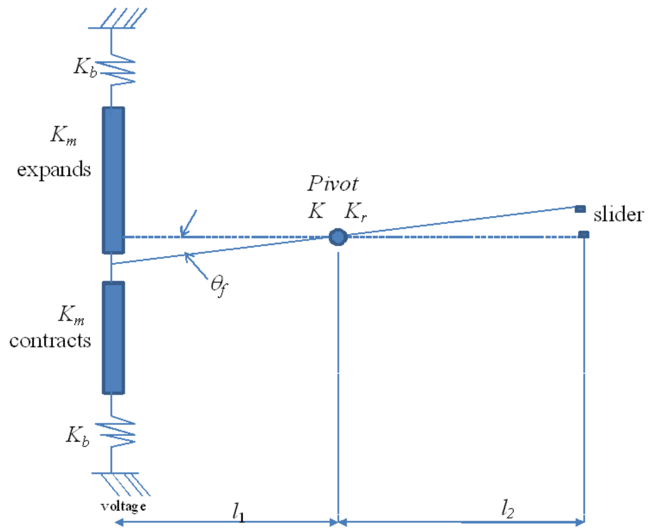

Figure 2.14: Equivalent spring mass system of PZT microactuator.

An important point for PZT microactuator modeling is that the PZT element acts in series with the base plate springs. Thus, the displacement of the PZT element results in displacements of the springs. The PZT and the base plate with spring constants K_m and K_b can be equivalent to a single spring with spring constant

$$K_T = \frac{2}{\frac{1}{K_m} + \frac{1}{K_b}}. \tag{2.3.6}$$

The model is derived by applying forces at the interface of the piezo element and the base plate spring and by summing moments about the pivot point. The free expansion of the piezoelectric element is expressed as

$$\theta_f = \frac{L_m d_{exp} V}{c l_1}, \tag{2.3.7}$$

where L_m is the length of the piezo element, d_{exp} is the piezo expansion coefficient, V is the voltage, c is the thickness of piezo element, and l_1 is the length as indicated in Figure 2.14.

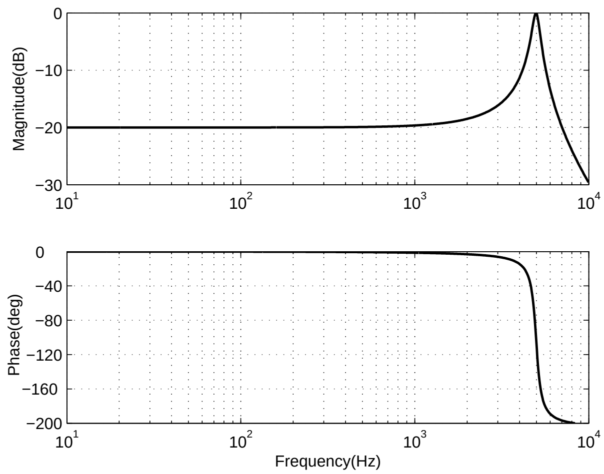

Figure 2.15: A typical frequency response of PZT microactuator.

The following second order differential equation can be derived to capture the dynamic behavior of the micro-actuator [43]

$$K\frac{d^2\theta}{dt} + C\frac{d\theta}{dt} + (K_r + K_T l_1^2)\theta = \frac{K_T L_m d_{exp} l_1}{c}V, \tag{2.3.8}$$

where K is the torsional inertia, C is the damping factor, and K_r is the torsional spring rate. A typical frequency response of PZT microactuator from voltage input to PZT output is shown in Figure 4.4.

Note that the frequency response of suspension-driven PZT from its voltage input to the head position should include the dynamics of the suspension as shown in Figure 2.7. The resonances can be modeled with the same formula as (2.3.5) excluding the resonant modes of arm.

2.3.3 Modeling of Disturbances

In modeling of HDDs, plant dynamics modeling and disturbance modeling are important. A high servo bandwidth does not always achieve better positioning accuracy due to existing disturbances. As will be shown in Chapter 3, disturbance model can be used for servo loop shaping to achieve better tracking accuracies.

Vibrations in disk drives cause the deviation of the R/W head positioning from the desired track center. It is the combination of the repeatable runout (RRO) and the non-repeatable runout (NRRO). Runout that is the same for every revolution of the disk is called RRO. Hence RRO has identical magnitude at each servo wedge of a track. Since RRO is synchronized with the frequency of rotation of spindle, its spectrum is distributed only at the fundamental frequency of spindle rotation and its harmonics. Disk slip is one of the major causes of RRO. Another major source of RRO occurs during servo-writing. Servo-writing is the process of writing servo patterns onto the magnetic disk. Any tracking errors during servo-writing are permanently written onto each servo pattern and become RRO during the normal operation of HDD. Other sources of RRO arise from imperfections in the spindle bearing and magnetic imbalance in the spindle motor. NRRO has many periodic components as well, but they are not synchronous to the spindle rotation. The major sources of NRRO are PES demodulation noise, disk vibrations, actuator arm vibrations, disk enclosure vibrations, and windage [4]. As the repeatable runout is compensated by iterative adaptive feedforward [44] [45] [46], we focus on the model of NRRO.

Figure 2.16 shows a simplified block-diagram of disk drive servo loop. y is the position of the R/W head and e is the position error signal. The signal d_1 represents all the torque disturbances to the system. Such disturbances include any torque due to air-turbulence force on the actuator, the suspension, and the slider. The effects of the torque disturbances are dominant at frequencies that are relatively low as compared to the servo bandwidth. The signal d_2 represents output disturbances that are due to non-repeatable motions of the disk and motor, which are directly added to the relative position of the R/W head and the reference track. The sensing noises n includes media noise, head noise, electric noise, and A/D quantization noise in the PES demodulation circuit. Therefore it is reasonable to model the sensing noise signal n as a broad-band white noise.

With closed-loop servo system, the PES ($e(k)$) can be measured and collected with synchronization of the track index. From Figure 2.16,

$$e(k) = -P(z)S(z)d_1(k) - S(z)d_2(k) + S(z)n(k), \tag{2.3.9}$$

where $P(z)$ is the transfer function of the discretized plant model $P(s)$ and the sensitivity function $S(z)$ is given by

$$S(z) = \frac{1}{1 + P(z)C(z)}. \tag{2.3.10}$$

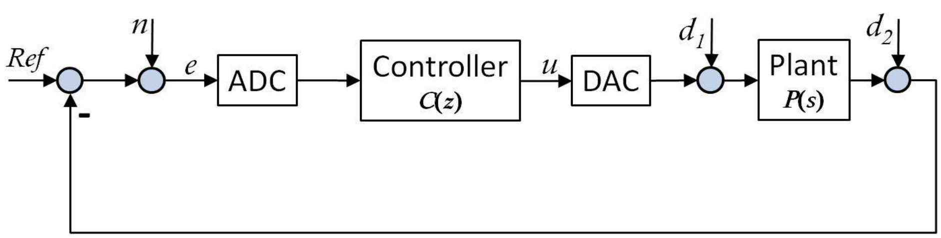

Figure 2.16: Block diagram of closed-loop with disturbances

Assuming that d_1, d_2, and n are uncorrelated, the power spectrum denoted by S_e of the error signal e is given by,

$$S_e = |P(z)S(z)|^2 S_{d_1} + |S(z)|^2 S_{d_2} + |S(z)|^2 S_n \tag{2.3.11}$$

where S_{d_1}, S_{d_2}, and S_n are spectrum of d_1, d_2, and n respectively.

The spectrum of NRRO component can be calculated from the collected PES data [47]. Figure 2.17 shows the NRRO spectrum of PES measured in a commercial HDD. Two humps are obviously observed in the baseline curve. One is in the frequency range at around 300 Hz, the other one is at around 1500 Hz. As we know that d_2 includes disk vibrations and suspension vibrations which are caused by the resonant modes of disks and suspension, they appear as spikes in the spectrum domain as shown in Figure 2.18. We also know that n, sensing noise, can be looked as a white noise. As such, its contribution to PES spectrum, $|S(z)|^2 S_n$, has the same shape as $|S(z)|^2$, which is very small at low frequencies around 300

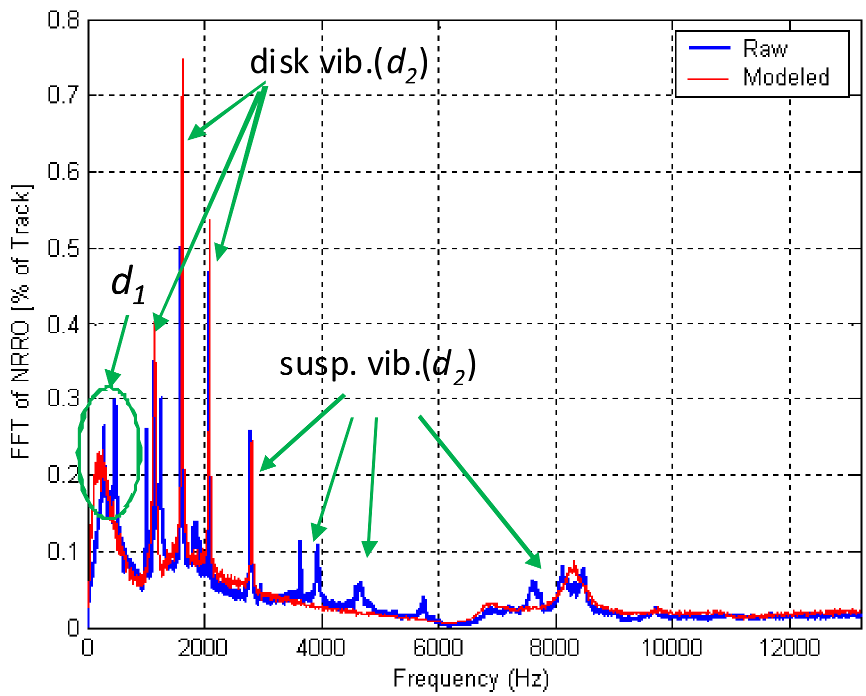

Figure 2.17: The NRRO spectrum measured in a commercial HDD.

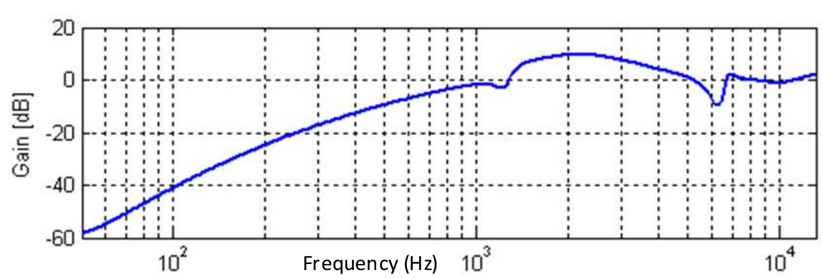

Figure 2.18: The bode plot of sensitivity function for a commercial HDD.

Hz. The torque disturbances, d_1, is usually distributed at low frequencies because it is caused by external environmental vibrations and air-flow turbulence force on VCM arm. With consideration of (2.3.11) and the distribution of $S(z)$, S_{d_1}, S_{d_2}, and S_n, we know that the second hump in Figure 2.18 is caused by $S(z)$ through $|S(z)|^2 S_n$, and the first hump is due to d_1 through $P(z)S(z)$ with a hump in a lower frequency range. Therefore S_{d_1}, S_{d_2}, and S_n can be decoupled from the PES NRRO spectrum by fitting weighted versions of $P(z)S(z)$ and $S(z)$ to the baseline curve of the spectrum and the spikes are considered as the effect of d_2. As such, the steps to obtain S_{d_1}, S_{d_2}, and S_n are

Step 1) Find $S_b(j)$, the base line of PES spectrum,

$$S_b(j) = \min_{i=1+(j-1)q}^{jq} S_e(i), \quad j = 1, 2, \cdots, L/q, \tag{2.3.12}$$

where L is the length of S_e and q is as small as possible.

Step 2) Compute S_{d_1} given by

$$S_{d_1} = W_L(z) S_b / |P(z)S(z)|^2, \tag{2.3.13}$$

where W_L is a low-pass filter used as weighting function to select S_b in low frequency range.

Step 3) Compute S_n with

$$S_n = W_H S_b / |S(z)|^2, \tag{2.3.14}$$

where W_H is the high-pass filter used as weighting function to select S_b in high frequency range.

Step 4) The baseline curve S_b can be fit well by the identified S_{d_1} and S_n. The remaining part of the spectrum is regarded as S_{d_2}. Thus,

$$S_{d_2} = \{S_e - [|P(z)S(z)|^2 |D_1(z)|^2 + |S(z)|^2 |N(z)|^2]\} / |S(z)|^2. \tag{2.3.15}$$

Step 5) Find stable $D_1(z)$, $D_2(z)$, and $N(z)$ such that

$$|D_1(z)|^2 = S_{d_1}, \tag{2.3.16}$$

$$|D_2(z)|^2 = S_{d_2}, \tag{2.3.17}$$

$$|N(z)|^2 = S_n. \tag{2.3.18}$$

Step 6) Calculate the models $D_1(s)$, $D_2(s)$, and $N(s)$ from $D_1(z)$, $D_2(z)$, and $N(z)$ using the bilinear approximation method [48].

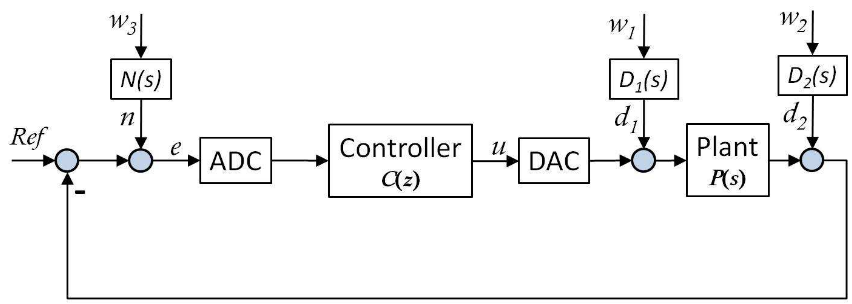

Figure 2.19: Control system with augmented disturbance and noise models.

In Figure 2.17, the thin gray line is the PES spectrum calculated from disturbances model, which matches well with the measured one (thick black line). The servo control system can be augmented with disturbance model as shown in Figure 2.19, where w_i $(i = 1,\ 2,\ 3)$ are independent white noises with unity variance.

Chapter 3

Design Pseudo-sine Current Profile for Smooth Seeking

Hard disk drive is widely used in consumer electronics where acoustic noise is becoming a more important performance index. Quiet seeking is required since seeking noise is one of the major source of acoustic noise. Residual vibrations are a significant factor not only to the acoustic problem, but also to the tracking performance of HDD.

In HDDs, the servo system moves R/W head from one track to another target track during track seeking. Conventionally, nonlinear controllers such as proximate time-optimal servo (PTOS) mechanism [30] [31] [32] are widely used for track-seeking. Other efforts include designing a unified control structure for both track-seeking and following, such as two-degree-of freedom (2DOF) servo mechanism with adaptive robust control or zero phase error tracking techniques [33] [34] [35][49]. For most of these works, the current profile as shown in Figure 3.1 is designed to compromise between the seek time and smooth switching from seeking to tracking. In Figure 3.1, the actuator is accelerated at maximum positive control effort until it reaches the maximum velocity. It is kept moving at constant velocity for a certain period, then it is decelerated at maximum negative control effort until it reaches close to target track at almost zero velocity. Finally, it switches to the linear track-following mode. In the procedure of seeking, the current profile is not continuously smooth,and is named as “jerk”-the rate of change in acceleration. This kind of “jerk” generates significant acoustic noise, and also excites the structural resonant modes of the servo mechanism such that ripples appear in the current profile after switching to track-following. The ripples existed in the control effort and/or in the position output is so called “residual vibrations”. The residual vibrations causes longer time for the R/W head to settle down on reference track to operate properly, it is also one significant source of TMR.

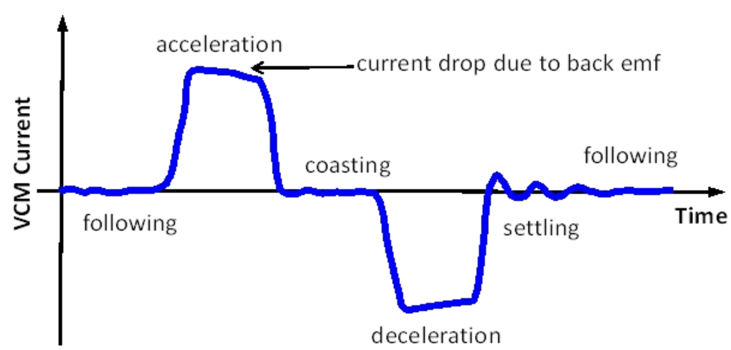

Figure 3.1: The current profile for conventional seeking controller.

In [50], ramped sinusoids was proposed to design the seek current profile to reduce residual vibrations. However, the effect was not sufficient and the tuning process was not straightforward. [51] [52] presented a method to design velocity trajectory for seeking based on minimizing the jerk together with a seek controller based on velocity control. This method can effectively suppress the high harmonics of the actuator acceleration and the residual vibrations after seek operation. But it is only applicable to short-span seek.

In this chapter, a systematic method is proposed to design a seek current profile which is able to reduce both acoustic noise and residual vibrations. Unlike the conventional seek profile, which usually excites the mechanical resonances and generates acoustic noise, a pseudo-sinusoidal wave is used to design a smooth current profile without "jerk". The current saturation limit and maximum velocity limit are also considered in the design of current profile to achieve arbitrary seek-length. A systematic method with a set of design parameters is proposed to minimize the residual vibrations caused by the most significant resonant mode.

3.1 Problem Formulation for Track-seeking

The rigid model VCM plant in Figure 2.9 can be expressed in state space as,

$$\begin{aligned} \dot{X} &= A_p X + B_p u \\ y &= C_p X \end{aligned} \tag{3.1.1}$$

where

$$A_p = \begin{bmatrix} 0 & k_y \\ 0 & 0 \end{bmatrix}, B_p = \begin{bmatrix} 0 \\ k_v \end{bmatrix}, C_p = \begin{bmatrix} 1 & 0 \end{bmatrix}, X = \begin{bmatrix} y & v \end{bmatrix}^T$$

The objective of seeking controller is to move actuator from initial state $[0 \quad 0]^T$ to target state $[y_0 \quad 0]^T$. The time optimal controller [30] problem is to minimize the cost function in (3.1.2) to achieve the fastest seeking, which results maximum acceleration and deceleration in the velocity profile.

$$J = \int_0^{t_f} 1dt, \quad when\ |u| \leq u_m. \tag{3.1.2}$$

The time optimal controller will cause chattering at switching point in existence of noise. PTOS [30] introduces a linear region for switching to overcome chattering problem.

3.1.1 Minimum Jerk Seeking

For consideration with acoustic noise, one more state $x_3 = \dot{u}$ is introduced, which is the rate of change in acceleration. For a typical seeking process, the initial states and terminating conditions are

$$\begin{bmatrix} x_1(0) \\ x_2(0) \\ x_3(0) \end{bmatrix} = \begin{bmatrix} x_1^0 \\ 0 \\ 0 \end{bmatrix}, and \begin{bmatrix} x_1(t_f) \\ x_2(t_f) \\ x_3(t_f) \end{bmatrix} = \begin{bmatrix} 0 \\ 0 \\ 0 \end{bmatrix},$$

respectively.

Note that t_f is fixed, and no constraint is placed for $u(t)$ for simplifying the problem. The control objective is to find an optimal $u^*(t), t \in [0, t_f]$ which minimizes the cost function J

$$J \quad = \int_0^{t_f} x_3^2(t)dt. \tag{3.1.3}$$

The optimal control for the minimum jerk seeking is [51],

$$u^*(t) = -\frac{120x_1^0}{t_f^5}t^3 + \frac{180x_1^0}{t_f^4}t^2 - \frac{60x_1^0}{t_f^3}t. \tag{3.1.4}$$

In Figure 3.2, the solid line shows the optimal current profile when $x_1^0 = -20,\ t_f = 2$, and it is very similar to the dashed line which is a sinusoidal curve.

The optimal current profile in (3.1.4) is derived when the current and velocity are not limited. It is only applicable for short-span seeking in practice. However, it infers that smooth sinusoidal current profile causes less jerk and generates less acoustic noise.

3.2 2DOF with Model Referenced Position and Current Feedforward Control

Figure 3.3 shows the block diagram of 2DOF structure with current and the model-referenced feedforward (MRF) control [35], where the VCM plant $P(s)$ is simplified as a double integrator plus resonant modes $H_d(s)$. k_v and k_y are scaling factors for velocity and position, respectively, and y_d is the target track. I_r is desired current profile which will be discussed in the next section. $C(z)$ is a nominal linear tracking

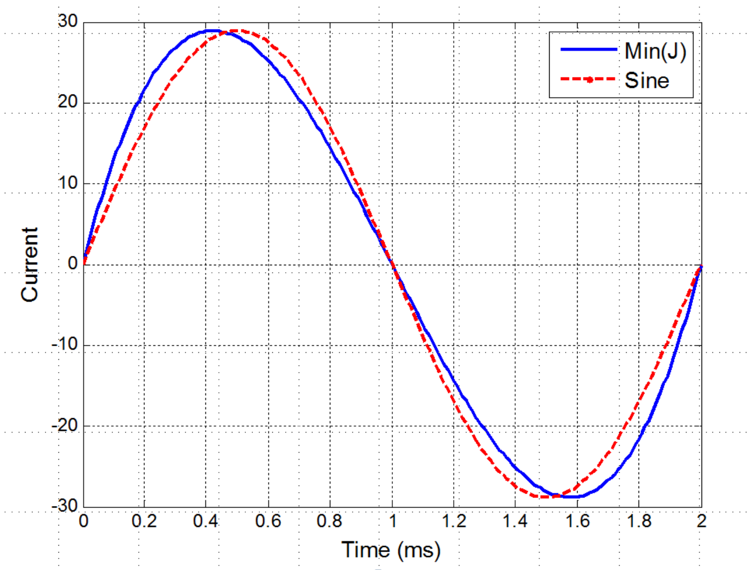

Figure 3.2: The optimal current profile for minimum jerk.

controller, and $\hat{P}(s)$ is the reference model to generate the position reference profile y_r.

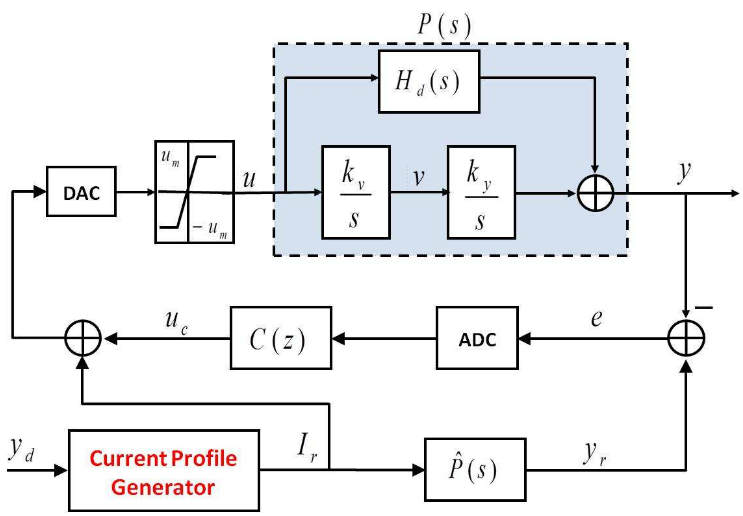

Figure 3.3: Block diagram of the model referenced feedforward control.

Assuming that $C(s)$ is the corresponding continuous controller, it can be obtained from Figure 3.3 that

$$y = \frac{P(s)/\hat{P}(s) + P(s)C(s)}{1 + P(s)C(s)}\hat{P}(s)I_r$$

$$= \frac{P(s)/\hat{P}(s) + P(s)C(s)}{1 + P(s)C(s)} y_r, \tag{3.2.5}$$

and

$$e = y_r - y = \frac{1 - P(s)/\hat{P}(s)}{1 + P(s)C(s)} y_r \tag{3.2.6}$$

(3.2.5) and (3.2.6) show that the output y will follow the reference track profile y_r exactly if the reference model $\hat{P}(s)$ is the same as the plant $P(s)$. The advantage of using the MRF lies in the fact that the VCM actuator can be driven directly by the feedforward current signal, whose profile can be customized by designers. Furthermore, the feedforward current loop is not limited by inherent sampling frequency of HDD servo system, which is determined by the number of servo sectors and spindle rotational speed. As such, a novel current profile can be designed to minimize the residual vibrations which is discussed in Section 3.3.

3.3 The Strategy to Design Pseudo-sine Current Profile

In HDD servo channel, the current driver can only provide limited value of current as shown in Figure 3.3. In addition, the maximum seeking velocity is also limited to keep the read/write head flying properly and to ensure reading back the full servo patterns in servo wedges. A proper current profile $I_r(t)$, as shown in Fig. 3.4, has acceleration (0 to t_1), coasting (t_1 to t_2), and deceleration (t_2 to t_5) stages. $I_1(t)$ is a current profile with no saturation and coasting for short-span seeking. The velocity of VCM increases until the maximum value reaches during the acceleration stage. During the coasting stage, the acceleration is zero and the velocity keeps at its maximum value. During the deceleration stage, the velocity of VCM is reduced from its maximum to zero before settling down on a target track. Both the acceleration and deceleration stages are divided into three segments: rising transition (S_1, S_4), saturation (maximum acceleration/deceleration), and falling transition (S_2, S_3).

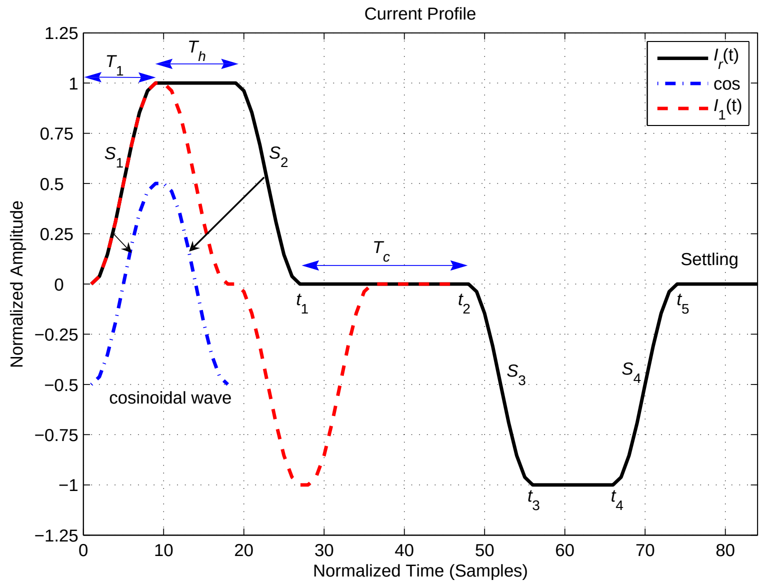

Figure 3.4: Pseudo sinusoidal current profile.

To reduce seeking noise, the VCM current should have a very smooth profile during seeking. Therefore, a perfect half period cosine wave is chosen to be the rising transition and falling transition. In Figure 3.4, S_1 and S_2 will form a cosine wave with offset of one. The amplitude is half of the saturation level, which ensures a smooth transition during saturating. The current profile is designed as

$$\frac{I_r(t)}{I_m/2} = \begin{cases} -\cos\omega_i t + 1, & 0 \le t < T_1 \\ 2, & T_1 \le t < T_1 + T_h \\ -\cos\omega_i(t - T_h) + 1, & T_1 + T_h \le t < t_1 \\ 0, & t_1 \le t < t_2 \\ \cos\omega_i(t - t_2) - 1, & t_2 \le t < t_3 \\ -2, & t_3 \le t < t_4 \\ -\cos\omega_i(t - t_4) - 1, & t_4 \le t < t_5 \\ 0, & t_5 \le t \end{cases} \tag{3.3.7}$$

with

$$T_1 = \frac{\pi}{\omega_i}, \qquad t_1 = T_h + 2T_1,$$

$$t_2 = t_1 + T_c, \qquad t_3 = t_2 + T_1,$$
$$t_4 = t_3 + T_h, \qquad t_5 = t_4 + T_1,$$

where ω_i is the frequency of cosine wave, T_h is saturation time, and T_c is coasting time. With the current profile and the reference model, we can derive the trajectory of the velocity and position. A rigid VCM plant model, a double integrator with velocity and position scaling factor k_v and k_y as shown in Fig. 3.3, is used as reference model in this chapter. The velocity and position reference trajectory can be derived from the current profile directly. In practical implementation, the position reference trajectory can be generated from reference model directly.

3.3.1 Pseudo-sine Current Profile Generation

Before deriving a proper current profile for seeking the target track y_d, the following parameters need to be specified:

1. The frequency of the sinusoidal wave (ω_i) with consideration of reducing acoustic noise:
   It determines the acceleration of current which will affect the amplitude of acoustic noise and seek time. The acoustic noise is mainly caused by the jerk in acceleration. As such, a low frequency will result in low acoustic noise but relatively long seek time. As the relationship in between seeking acoustic noise and frequency is not clearly known yet, the determination of the frequency is based on trial and error.
2. The maximum current (I_m):
   It is specified by current driver.
3. The maximum velocity ($V_{\max}$):
   It is set to ensure read/write head to fly properly [53] and to read back a full servo pattern properly.

According to the velocity and position trajectories generated from reference model, we can determine the velocity or reached target tracks at the following transitions:

1. V_{f1}: the velocity reached at the end of transition S_1;
2. $T_{hmax} = \frac{V_{max}-2V_{f1}}{k_v}$: the saturation time for actuator to reach the maximum velocity;
3. y_{d1}: the maximum target track reached using profile $I_1(t)$ without saturation and coasting;
4. y_{d2}: the target track reached using profile $I_r(t)$ with the maximum saturation time but without coasting.

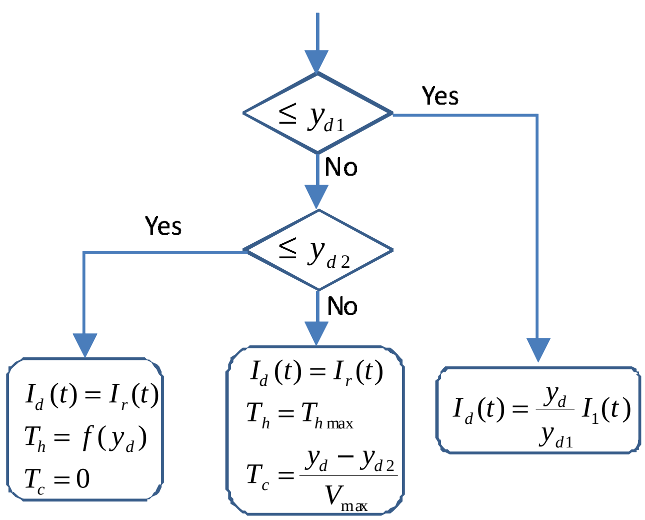

Figure 3.5: The process to generate current profile.

Having these parameters, the process to generate the current profile for y_d is shown in Figure 3.5. For cases when $y_{d1}<y_d\leq y_{d2}$, the value can be derived using look-up table for easy implementation.

3.3.2 Minimizing Residual Vibrations

The seeking residual vibrations are caused by the lightly-damped structural resonant modes of the actuator. The residual vibrations are actually the response of the resonant dynamics $H_d(s)$ (in Fig. 3.3) to the transients, such as S_1, S_2, S_3, and S_4 in the current profile.

According to the current profile shown in Fig. 3.4, we have,

$$S_2(t) = -S_1(t - T_1 - T_h), \tag{3.3.8}$$

$$S_4(t) = -S_3(t - T_1 - T_h). \tag{3.3.9}$$

Define $V_{ri}(t)$ as the response of $H_d(s)$ to $S_i(t)$ for $i=1,2,3,4$. Note that

$$V_{r2} = -V_{r1}(t - T_1 - T_h), \tag{3.3.10}$$

$$V_{r4} = -V_{r3}(t - T_1 - T_h). \tag{3.3.11}$$

The total residual vibrations due to S_1 and S_2 denoted by $V_{12}(t)$, and that due to S_3 and S_4 denoted by $V_{34}(t)$ can be calculated

$$V_{12}(t) \quad = V_{r1}(t) - V_{r1}(t - T_1 - T_h), \tag{3.3.12}$$

$$V_{34}(t) \quad = V_{r3}(t) - V_{r3}(t - T_1 - T_h), \tag{3.3.13}$$

respectively.

Since there is usually one dominant resonant mode in $H_d(s)$ whose frequency is ω_r, both V_{r1} and V_{r2} are slowly decayed periodical signals with period $T_r = \frac{2\pi}{\omega_r}$. If $T_1 + T_h = N \times T_r$ with N being an integer, V_{12} is minimized by using the response to S_2 to cancel the response to S_1. The same scenario is applied to V_{34}.

On the other hand for short-span seek where T_h is zero, T_1 needs to be multiples of T_r to minimize residual vibrations. In addition, as V_{34} can be regarded as $-V_{12}$ delayed by $(2T_1 + T_h + T_c)$, we can choose T_1, T_h, and T_c to be multiples of T_r to achieve minimum residual vibration for all cases.

Note that T_c and T_h are not arbitrary selected but calculated from y_d. When the calculated values are not multiples of T_r, the following strategy can be applied. First, set the value to the closest multiples of T_r by increasing the calculated values. As such, the reached target track will be different from y_d, e.g. $\hat{y_d}$. We can then scale the amplitude of current profile by the factor $\frac{y_d}{\hat{y_d}}$.

3.4 Simulation and Comparison with PTOS

Table 3.1: Parameters for resonant modes

$\omega_1(rad/s)$	ζ_1	b_{11}	b_{12}	$\omega_2(rad/s)$	ζ_2	b_{21}	b_{22}	k_v	k_y
$2\pi{\cdot}3400$	0.0258	1	0	$2\pi{\cdot}8300$	0.01	0	0.273	1.174e3	9.7677e4

In the simulation, two most significant resonant modes are considered. The plant dynamics are expressed as

$$P(s) = \frac{k_v k_y}{s^2} \cdot \left(\frac{b_{12}\omega_1 s + b_{11}\omega_1^2}{s^2 + 2\zeta_1 s + \omega_1^2} + \frac{b_{22}\omega_1 s + b_{21}\omega_2^2}{s^2 + 2\zeta_2 s + \omega_2^2}\right) \tag{3.4.14}$$

where the parameters are listed in Table 3.1.

The maximum current is I_m=0.25(A). The first resonant mode is dominant in causing residual vibrations. As such, ω_r=$2\pi{\cdot}3400$ (rad/sec). The sampling frequency chosen is 20.4k Hz. The frequency of the sinusoidal wave is chosen to be 850 Hz, which is one fourth of the first resonant frequency. As such, we have T_1=$2T_r$=$12T_s$.

For comparison, a PTOS controller [30] is designed as shown in Figure 3.6. It consists of a state estimator and a sliding surface. The state vector of the observer is $[\hat{y}\ \hat{v}\ \hat{d}]^T$, where disturbance $\hat{d}$ is an augmented state. y_{ref} is the reference track center, $\hat{y}$ is the estimated position of output from PES signal and track number. The gain of the observer is chosen as L=$[1.3083 \quad 0.01086 \quad 0.008]^T$. The sliding surface is designed as

$$e = y_r - \hat{y}, \tag{3.4.15}$$

$$u = sat(k_2(f(e) - \hat{v}) - \hat{d}), \tag{3.4.16}$$

$$f(e) = \begin{cases} \frac{k_1}{k_2}(e), & \text{for } |e| \leq y_l \\ sgn(e)[\sqrt{2\alpha I_m k_v |e|} - \frac{I_m}{k_2}], & \text{for } |e| > y_l \end{cases} \quad (3.4.17)$$

where $y_l = \frac{I_m}{k_1}$, k_1 and k_2 are chosen to be 0.032 and 2.7581, respectively.

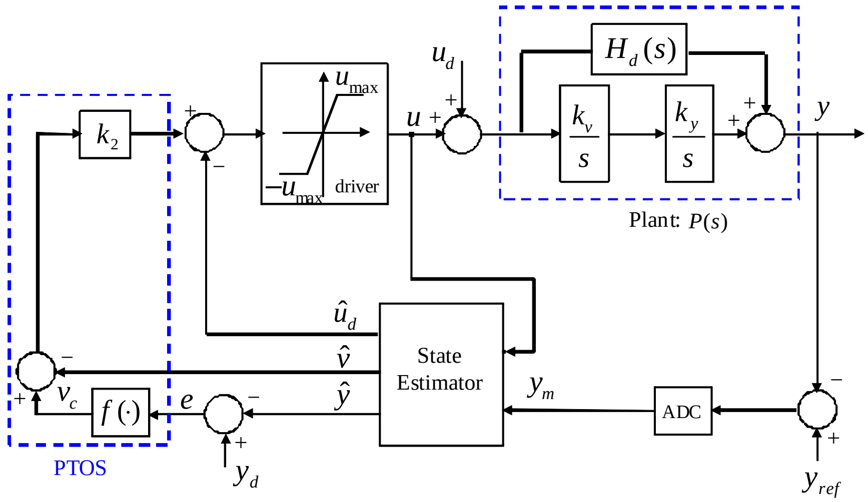

Figure 3.6: The block diagram of PTOS.

In MRF as shown in Figure 3.7, the controller $C(z)$ is the same as the linear tracking controller (state estimator and sate feedback) designed in PTOS.

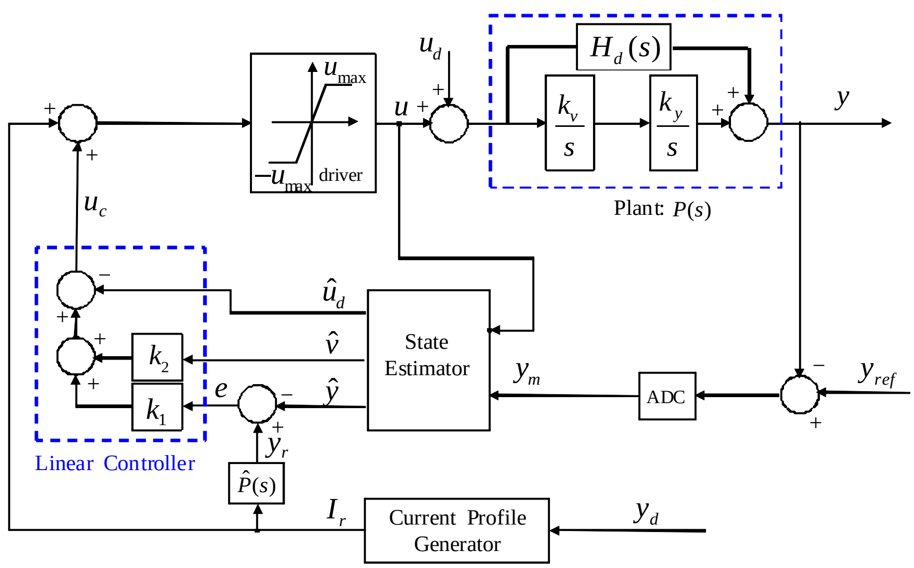

Figure 3.7: The block diagram of 2DOF with MRF.

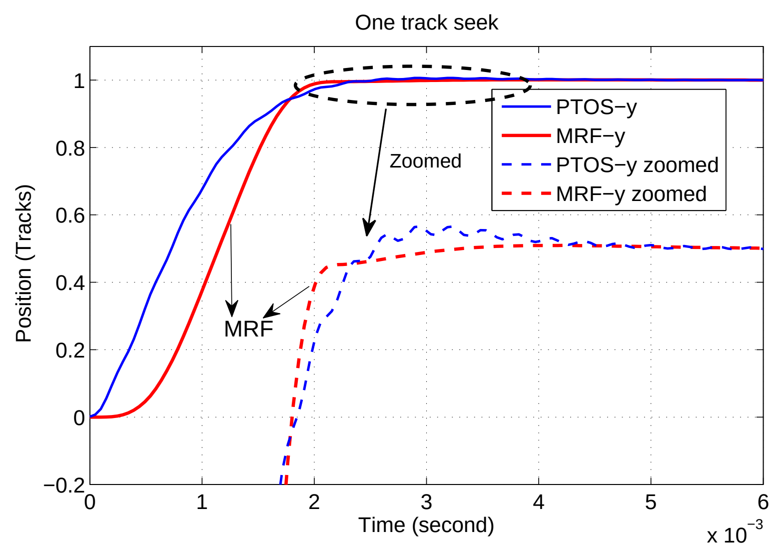

Figure 3.8: Position output for one track seeking.

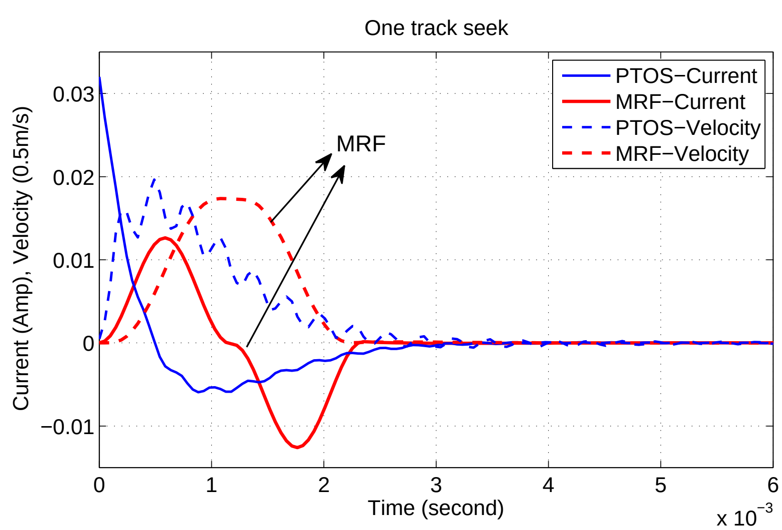

Figure 3.9: Velocity and current profile for one track seeking.

Figures. 3.8 and 3.9 show the position output, velocity, and current profiles for one track seeking, where thin lines are for PTOS and thick lines are for MRF. As the full-scaled current profile $I_1(t)$ shown in Figure 3.4 can reach 19.839 tracks, the feedforward current can be derived as $[I_1(t)/19.839]$. From the position curves, it can be seen that the residual vibration is significantly reduced in MRF, which is also confirmed in velocity trajectory. The seek time for MRF is even less than that for PTOS. Although the starting current and ending current in MRF are smaller than those in PTOS, the intermediate acceleration and deceleration in MRF are larger, which enable that the MRF scheme can provide rather smooth signal for starting and ending currents as well as faster seeking.

Figure 3.10 and Figure 3.11 show the results for fifty-track seek when saturation happens. Similar results are observed. For fifty-track seek, the calculated saturation time T_h is $9.5971 \cdot T_s$, and T_c=0. To attenuate residual vibrations, T_h is set to be $12T_s$ which is two times of T_r. However, such a full scaled current profile can reach 59.5171 tracks, so an appropriate feedforward current profile is $I_r(t)$ scaled by 50/59.5171 with T_h=$12T_s$.

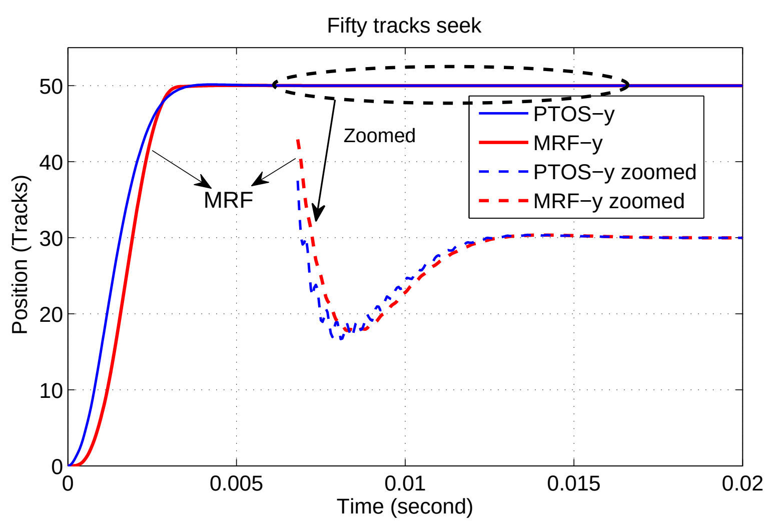

Figure 3.10: Position output for 50 tracks seeking.

Figure 3.12 shows the input current profiles for different T_1 without saturation and

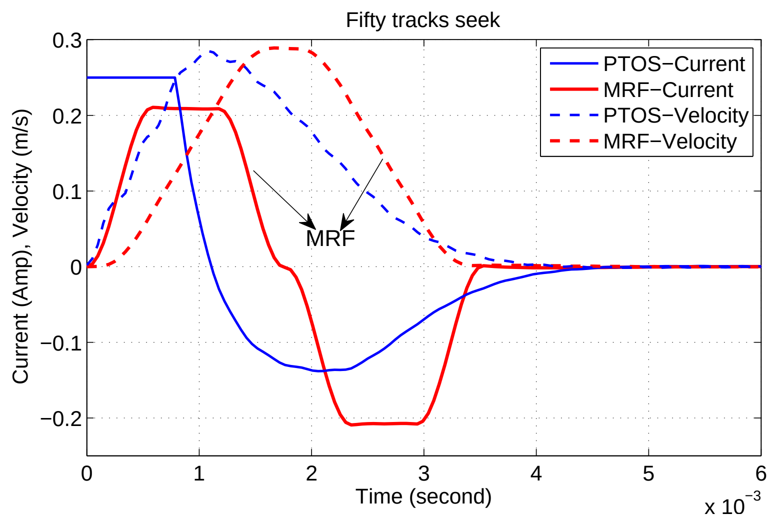

Figure 3.11: Velocity and current profile for 50 tracks seeking.

coasting. It shows clearly that when T_1=12T_s, i.e., twice of the period of resonant mode T_r, the input current has the least oscillations. Other cases show that the oscillation is significantly enlarged even when the frequency of sinusoidal wave is reduced i.e., T_1=13, 14T_s. Figure 3.13 shows the input current profiles for different

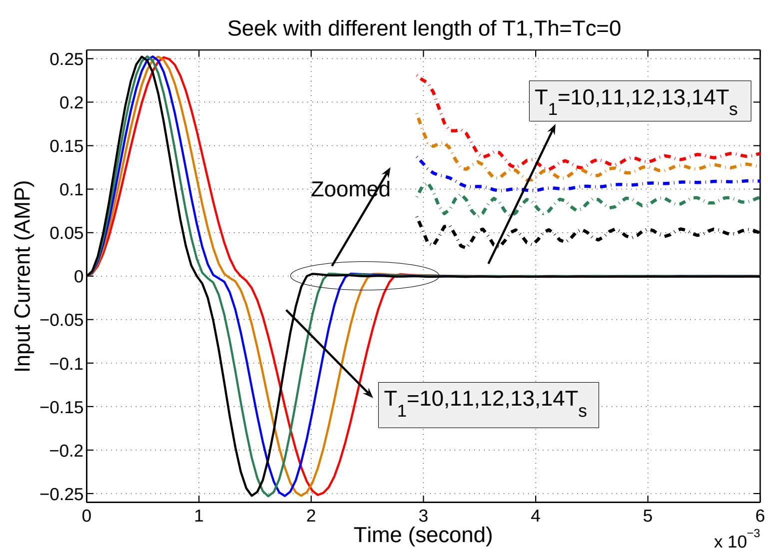

Figure 3.12: Input current while seeking with different T_1.

T_h with T_1=12T_s but without coasting. It shows clearly that when T_h=0T_s or 6T_s which is 0 or one time of T_r, the input current has less oscillations than other cases.

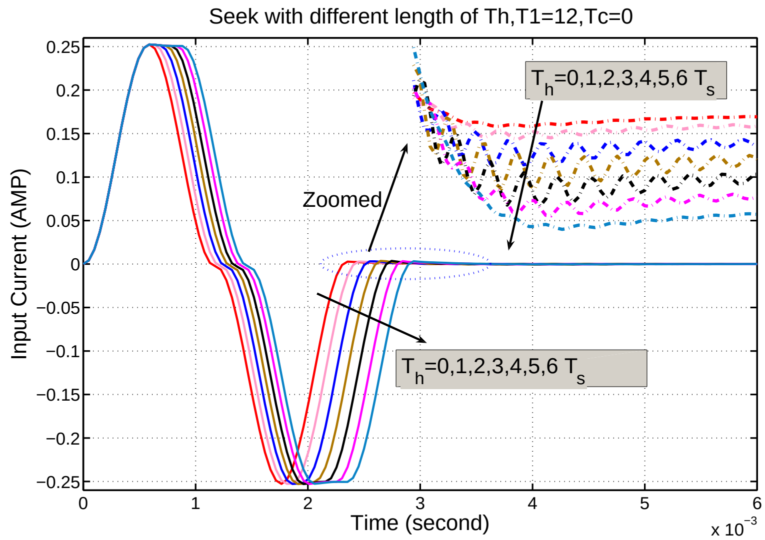

Figure 3.13: Input current while seeking with different T_h.

For coasting time, we can obtain the similar results as those shown in Figure 3.13. All the above analysis verifies the conclusion drawn in Section 3.3.2.

3.5 Conclusions

A smooth near optimal pseudo-sinusoidal seek current profile for arbitrary seek length has been proposed for minimizing the jerk to reduce seek acoustic noise. With the parameters for the current profile properly designed, residual vibrations due to the dominant resonant modes can be minimized. The simulation results have shown the advantage and performance improvement of the proposed method over PTOS method with respect to both the seek time and residual vibrations.

Chapter 4

IES Settling Controller for Dual-stage Servo System

Dual-stage servo system is one of the most obvious technologies to achieve the high servo performance [54] [55] [56] [40] [57] [58]. The design of tracking/seeking controller proposed in Chapter 3 and 4 can be applied to dual-stage servo systems for the requirements of HDD in consumer applications. In this chapter, a settling controller is proposed for dual-stage servo systems. There are a few algorithms developed to achieve fast and smooth settling in current literature. The most famous is initial value compensation (IVC) method [59] [60]. This method is quite effective for the single stage servo loop with voice coil motor (VCM). However, it will encounter problem if the servo system has double roots, which lead to a singular matrix whose inverse does not exist. Another method is command shaping [61] [62] method, which only considers initial value of displacement. In the method proposed in this chapter, the transient response of the position error due to the VCM nonzero initial states is taken into account, and a compensation signal is generated and injected at the controller input to shape the position error signal and thus cancel the undesired transitions due to the initial states. This is the called initial error shaping (IES) method. The IES method can be used to deal with transient problems caused by both initial position and initial velocity. With this method, only one feedforward controller is needed, and the implementation is straightforward using look up table

(LUT) without requirement of much computation resources.

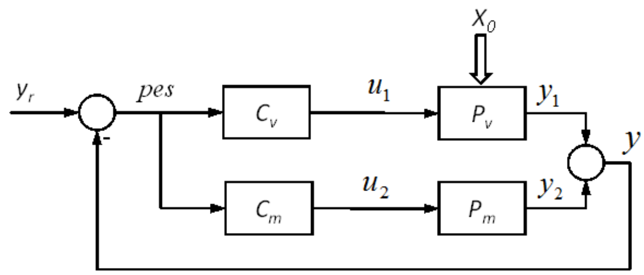

Figure 4.1: Parallel-type dual-stage servo system.

4.1 Settling Problem in Dual-stage Servo Systems

Figure 4.1 shows a typical parallel dual-stage servo structure in on-track mode. The seeking algorithm for dual-stage systems is the same as single-stage systems such as 2DOF scheme in [55], which uses the VCM actuator to achieve fast seeking. In on-track mode, dual-stage system responds to command much faster than single stage due to the boosted high servo bandwidth. The whole system has no obvious slow modes, since PZT is used to compensate the slow modes in VCM loop. However, it has a relatively large overshoot, as shown in section 4.4. Therefore, it is important to deal with the non-zero VCM states for smooth and fast settling when switching from seeking to track-following.

The major initial values of VCM states that need to be considered are the initial velocity and initial position. The other states due to resonances are not considered because it is difficult to estimate these states accurately and their impacts to the settling transition are relatively small in practice. Denote VCM plant as P_v: (A_v, B_v, C_v, D_v), where $D_v = 0$, and PZT plant as P_m: (A_m, B_m, C_m, D_m), where $D_m = 0$, using states X_v and X_m respectively. According to Figure 4.1, the dual-stage plant $P(s) = [P_v(s), P_m(s)]$ is described as,

$$X_p = \begin{bmatrix} X_v \\ X_m \end{bmatrix}, u = \begin{bmatrix} u_1 \\ u_2 \end{bmatrix},$$
$$\begin{cases} X_p(k+1) - \begin{bmatrix} X_0 \\ 0 \end{bmatrix} = A_p X_p(k) + B_p u(k) \\ y(k) = y_1(k) + y_2(k) = C_p X_p(k) \end{cases}, \tag{4.1.1}$$

where

$$A_p = \begin{bmatrix} A_v & 0 \\ 0 & X_m \end{bmatrix}, B_p = \begin{bmatrix} B_v & 0 \\ 0 & B_m \end{bmatrix}, C_p = \begin{bmatrix} C_v & C_m \end{bmatrix}. \tag{4.1.2}$$

The controller $C(z)^T = [C_v(z)\ C_m(z)]$ is written in state space as,

$$\begin{cases} X_c(k+1) = A_c X_c(k) + B_c(y_r(k) - y(k)), \\ u(k) = C_c X_c(k) + D_c(y_r(k) - y(k)). \end{cases} \tag{4.1.3}$$

The output of the closed-loop system is obtained as

$$y = [\frac{C \cdot adj(zI - A)B}{|zI - A|} + D]y_r + \frac{C \cdot adj(zI - A)z}{|zI - A|} \begin{bmatrix} X_0 \\ 0 \end{bmatrix}, \tag{4.1.4}$$

where

$$A = \begin{bmatrix} A_p - B_p D_c C_p & B_p C_c \\ -B_c C_p & A_c \end{bmatrix}, B = \begin{bmatrix} B_p \\ C_c \end{bmatrix}, C = \begin{bmatrix} C_p & 0 \end{bmatrix}, D = 0. \tag{4.1.5}$$

X_0 is the plant initial states including initial position y_0 and initial velocity v_0 of VCM actuator. y_r is the command reference signal. Given y_r being zero during tracking, we could deduce the transient response to the non-zero VCM actuator initial states y_0 and v_0 from (4.1.4) after mode-switching [63]. This transient response to non-zero initial states of VCM can lead to a longer settling time.

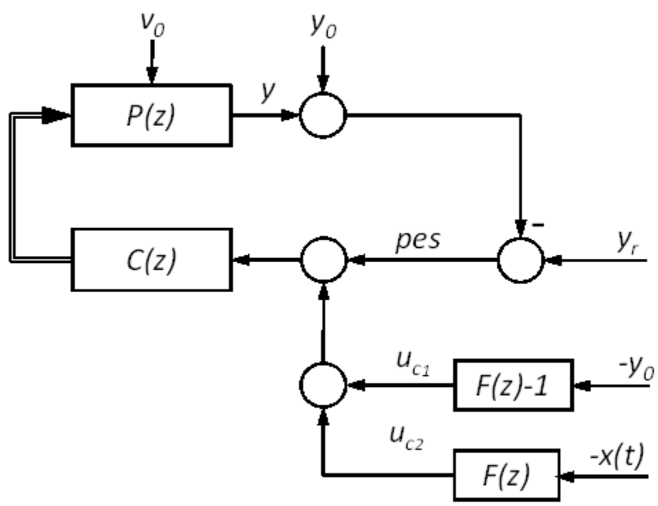

Figure 4.2: Equivalent closed-loop control system with IES for initial position and velocity.

4.2 IES for Dual-Stage Systems

Instead of designing the initial values for the controller states or injecting external signal at the plant input to cancel the transient response in the plant output due to the nonzero initial states of VCM actuator [59], a compensation signal will be designed and injected at the controller input to shape the position error signal due to nonzero VCM initial states before it is fed into the nominal on-track mode controller.

Figure 4.2 shows the system block diagram with IES, where the injected signals u_{c1} and u_{c2} are used to compensate initial position y_0 and initial velocity v_0, respectively. For the initial position y_0 of VCM, it is equivalent to applying a disturbance at the output as shown in Figure 4.2. Let $T_v(z)$ denote the transfer function from initial velocity v_0 to PES that can be derived from (4.1.4). From Figure 4.2, the PES is given as,

$$PES = PES|_{y_r} + PES|_{y_0} + PES|_{v_0} \tag{4.2.6}$$

where

$$PES|_{y_r} = T_c(z)y_r, \tag{4.2.7}$$

$$PES|_{y_0} = -y_0 + T_c(z)F(z)y_0, \tag{4.2.8}$$

$$PES|_{v_0} = T_c(z)F(z)x(t) + T_v(z)V_0, \tag{4.2.9}$$

where

$$T_c(z) = \frac{P(z)C(z)}{1 + P(z)C(z)}. \tag{4.2.10}$$

is the closed-loop transfer function.

The objective is to design a feedforward controller $F(z)$ and external injected signal $x(t)$ to improve the transients due to y_0 in (4.2.8) and v_0 in (4.2.9).

4.2.1 IES for Initial Position

If there is no IES compensation in (4.2.8), i.e. $F(z) = 1$, the transient state of PES in settling is the same as the transient part of step response of the closed-loop system. In order to improve the transient response in settling, the mode added by $F(z)$ should be the inverse of the transient response of the closed-loop system.

If the closed-loop transfer function $T_c(z)$ can be inverted, perfect settling can be achieved by setting $F(z)$ as

$$F(z) = \frac{1}{T_c(z)} = \frac{1 + P(z)C(z)}{P(z)C(z)}. \tag{4.2.11}$$

Generally, $F(z)$ is not invertible due to the existence of unstable zeros. For such a case, $F(z)$ can be designed as the following using ZPET method [64]. The closed-loop transfer function in (4.2.8) can be written as,

$$\frac{P(z)C(z)}{1 + P(z)C(z)} = \frac{B(z)}{A(z)}, \tag{4.2.12}$$

$$A(z) = a_0 + a_1 z + ... + a_n z^n, \tag{4.2.13}$$

$$B(z) = B^a(z)B^u(z) = b_0 + b_1 + ... + b_m z^m. \tag{4.2.14}$$

where $B^a(z)$ and $B^u(z)$ include stable and unstable zeros of $B(z)$ respectively. Stable zero means that the zeros are inside the unit circle in the complex plane. Let

$$B^u(z) = b_{u0} + b_{u1} + ... + b_{uq}z^q. \tag{4.2.15}$$

Define its complex conjugate as

$$B^{u^*}(z^{-1}) = b_{u0} + b_{u1}z^{-1} + ... + b_{uq}z^{-q}, \tag{4.2.16}$$

we can design $F(z)$ as

$$F(z) = \frac{A(z)B^{u^*}(z^{-1})}{z^{n-m+q}B^a(z)[B^u(1)]^2}. \tag{4.2.17}$$

Now from (4.2.8), we have

$$\begin{aligned} PES|_{y_0} = &\quad -y_0 + \frac{P(z)C(z)}{1+P(z)C(z)}F(z)y_0 \\ = &\quad -y_0 + \frac{B^a(z)B^u(z)}{A(z)}\frac{A(z)B^{u^*}(z^{-1})}{B^a(z)[B^u(1)]^2}z^{-n+m-q}y_0 \\ = &\quad -y_0 + \frac{B^u(z)B^{u^*}(z^{-1})}{[B^u(1)]^2}z^{-n+m-q}y_0. \end{aligned} \tag{4.2.18}$$

Note that $B^{u^*}(z^{-1})$ is the complex conjugate of $B^u(z)$. Thus, after $(n-m+q)$ steps delay, the second part in (4.2.18) is the moving average of y_0. Since y_0 is the initial value of position, its moving average is the same, which means that $PES|_{y_0}$ converges to zero after $(n-m+q)$ steps delay.

4.2.2 IES for Initial Velocity

Since $F(z)$ is designed as (4.2.17), (4.2.9) can be expressed as

$$PES|_{v_0} \quad = \quad \frac{B^u(z)B^{u^*}(z^{-1})}{[B^u(1)]^2}z^{-(n-m+q)}x(t) + T_v(z)v_0, \tag{4.2.19}$$

where $x(t)$ can be designed as

$$X(z) = z^{n-m+q}[-T_v(z)v_0]. \tag{4.2.20}$$

We have,

$$
\begin{aligned}
PES|_{v_0} &= \frac{B^u(z)B^{u^*}(z^{-1})}{[B^u(1)]^2} z^{-(n-m+q)} z^{n-m+q}[-T_v(z)v_0] + T_v(z)v_0 \\
&= \frac{B^u(z)B^{u^*}(z^{-1})}{[B^u(1)]^2}[-T_v(z)v_0] + T_v(z)v_0. \qquad (4.2.21)
\end{aligned}
$$

Notice again that $B^{u^*}(z^{-1})$ is the complex conjugate of $B^u(z)$, thus the first part of the above equation is the moving average of $-T_v(z)v_0$, which is very close to $-T_v(z)v_0$ due to the fact that $-T_v(z)v_0$ is the smooth transient response to slow decaying of energy stored in VCM. Thus, it cancels the $T_v(z)v_0$ due to the initial velocity.

4.3 More Considerations in Designing $F(z)$

In the previous section, all the stable zeros of $T_c(z)$ are treated as acceptable and are cancelled by the corresponding poles of $F(z)$. If the zero is close to the unit circle, and is not exactly cancelled by pole in the $F(z)$ due to model estimation error, oscillations will occur in the output and input current which is so-called as "acoustic" problem, as shown in section 4.4.

To avoid the acoustic problem, an acceptable circle inside unit circle will be defined with radius less than one. Generally, it is chosen as 0.96 (typical structural resonances with damping ratio of less than 0.1 are located outside this circle). The acceptable zeros located inside the acceptable circle will be cancelled by corresponding poles in $F(z)$, and others are cancelled by the corresponding conjugate zeros in $F(z)$.

Usually, the closed-loop transfer $T_c(z)$ for dual stage servo system is a high-order system. Some of its zeros are already cancelled by the poles nearby, and these poles and zeros can be neglected during designing $F(z)$ to reduce the order of $F(z)$. However, if the zero is located around the positive real axis near unit circle, it is a slow mode. For a slow mode zero, it should be included in the design of $F(z)$

even it has a corresponding pole around canceling it.

In conclusion, we can design the $F(z)$ according to the ZPET rule as the following steps:

1. Analyze the poles and zeros of the closed-loop transfer function. Ignore those poles and zeros that are matched well except the slow mode zeros;

2. Identify the acceptable and unacceptable zeros;

3. Cancel all the unmatched poles by placing the corresponding zeros into $F(z)$;

4. Cancel all the acceptable zeros by placing the corresponding poles into $F(z)$;

5. Cancel all the unacceptable zeros by placing the their complex conjugate zeros into $F(z)$. For example, if $a + bi$ is one unacceptable zero, then place a zero $\frac{a-bi}{a^2+b^2}$ into $F(z)$;

6. Place proper number of poles at 0 into $F(z)$ to balance the order between the denominator and numerator of $F(z)$;

7. Scale $F(z)$ such that it has unit gain.

Step 6 will increase order and delay. However, the delay induced is cancelled by designing $X(z) = z^{n-m+q}[-T_v(z)v_0]$ which includes corresponding steps advanced. The injected compensation signals $-F(z)X(z)$ and $y_0(1 - F(z))$ are precalculated in practical implementation using look-up table, thus the increased order will not increase the complexity of computation.

4.4 Design Example

The frequency responses of the VCM and PZT actuator are shown in Figure 4.3 and Figure 4.4, where the dotted line is the measured response while the solid line

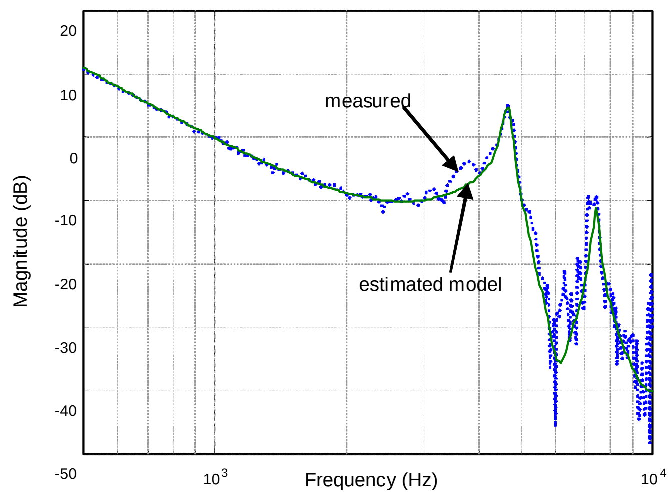

Figure 4.3: Frequency response of VCM actuator.

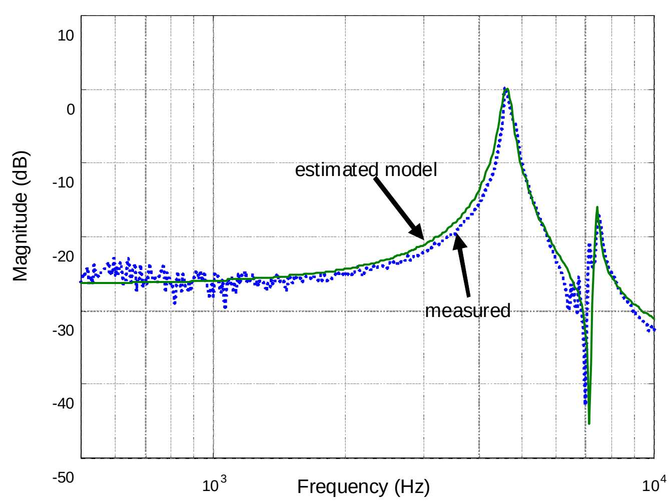

Figure 4.4: Frequency response of PZT micro-actuator.

is the modeled response with a sampling frequency of 20 kHz. The VCM plant model is identified with gain scaled as

$$P_v(z) = \frac{num_v(z)}{den_v(z)},$$

where

$$\begin{aligned} num_v(z) = & -0.002798z^7 + 0.1322z^6 + 0.9935z^5 + 1.989z^4 \\ & +1.533z^3 + 0.3883z^2 - 0.02272z - 0.006695, \\ den_v(z) = & \; z^8 - 0.5764z^7 - 0.09174z^6 + 0.04249z^5 - 1.182z^4 \\ & +0.5602z^3 - 0.2009z^2 - 0.1413z + 0.592. \end{aligned}$$

PZT plant is identified as

$$P_m(z) = \frac{-0.008044z^3 + 0.03511z^2 + 0.06053z + 0.01584}{z^3 + 1.176z^2 + 1.236z + 0.8588}.$$

The controllers (together with notch filter) for PZT and VCM are

$$\begin{aligned} C_v(z) = & \frac{1.063z^6 - 1.38z^5 + 1.828z^4 - 1.914z^3 + 1.071z^2 - 0.656z + 0.004298}{100(z^6 - 2.306z^5 + 2.298z^4 - 1.407z^3 + 0.4805z^2 - 0.06531z)}, \\ C_m(z) = & \frac{5.105z^3 - 1.002z^2 + 4.112z - 2.461}{z^3 - 1.769z^2 + 0.9234z - 0.1503}, \end{aligned}$$

respectively. Figure 4.5 shows the step response of the closed-loop system. As

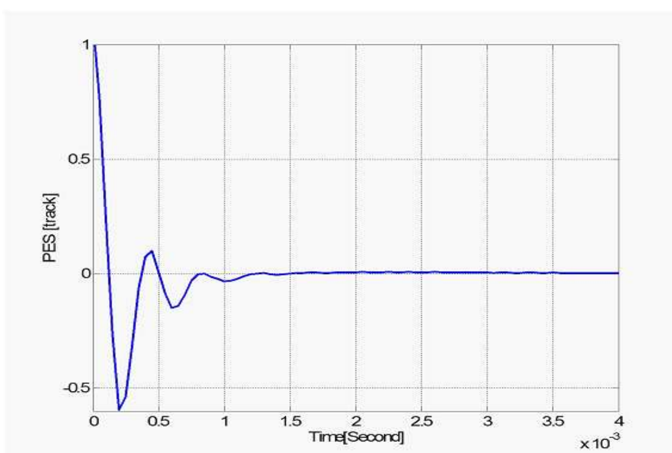

Figure 4.5: Step response of the dual-stage servo system.

Table 4.1: Characteristic of poles/zeros in tracking.

No.	poles	zeros	Remark
1	-0.9833 ± 0.040256i	-0.9833 ± 0.040256i	cancelled
2	-0.8541	-1.0422	not matched well
3	-0.1947±0.6855i	-0.1956±0.6855i	cancelled
4	-0.1710±0.5611i	-0.1204±0.8550i	not matched well
5	-0.1487±0.9779i	-0.1487±0.9779i	cancelled
6	-0.1472±0.9775i	-0.1531±0.9674i	almost cancelled (acoustic problem)
7	0.9997±0.0005i	0.9997±0.0005i	cancelled
8	0.9388±0.0151i	0.9473±0.0213i	almost cancelled (slow mode)
9	0.9917	0.9917	cancelled
10	0.5798±0.1152i	0.5318±0.1094i	almost cancelled
11	0.4647±0.5657i		not matched
12	0.3897±0.00000033i	0.38967±0.00000022i	cancelled
13	0.3222±0.8359i	0.3210±0.8176i	almost cancelled
14	0.3000±0.5777i	0.2523±0.5777i	almost cancelled
15	0.0004	0.0008	cancelled
16		-0.33412965418467	not matched
17		5.74196058627462	not matched

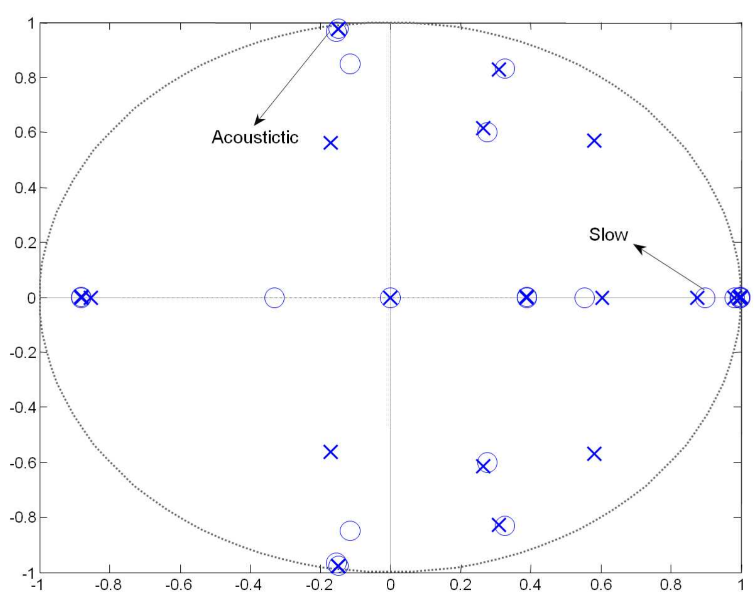

Figure 4.6: Poles/zeros map of the closed-loop system.

stated previously, it responds to the command reference fast but has a relatively large overshoot.

The pole/zero map of the closed-loop transfer function is depicted in Figure 4.6, and all poles/zeros are listed in Table 4.1. First, we treat all unmatched stable zeros as acceptable. Thus according to the above design procedure, a 7^{th} order $F(z)$ is designed. The simulation results are lines marked with "B" as shown in Figure 4.7 and Figure 4.8 with initial position $y_0 = 1$ track. The overshoot of the dotted curve is smaller with compensation. However, there is one slow transition left uncompensated which is due to the slow zero in Figure 4.6. In Figure 4.8 there is an obvious acoustic oscillation in the control effort. This is due to the acoustic zero, which is very close to the unit circle and can be seen in Figure 4.6.

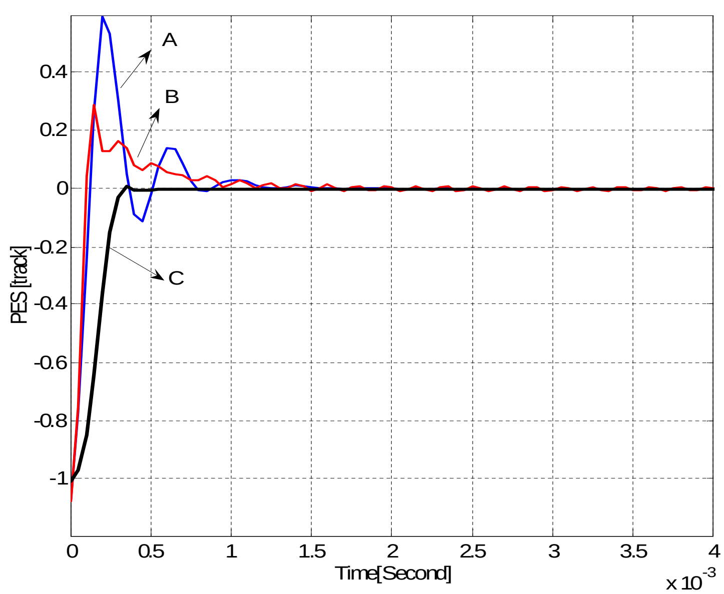

Figure 4.7: Settling transient due to initial position $y_0 = 1$ track (A: no compensation; B: with compensation and without considering acoustic and slow modes; C: with compensation considering acoustic and slow modes).

Next, the above acoustic zero is treated as unacceptable and $F(z)$ is redesigned. Meanwhile, the partially cancelled slow zero/pole, as indicated in Figure 4.6, is retained and considered into the design of $F(z)$. An $F(z)$ of 13^{th} order is derived as

$$
\begin{aligned}
F(z) = & \quad \frac{num_f(z)}{den_f(z)}, \\
num_f(z) = & \quad 0.1308z^{13} - 0.0278z^{12} + 0.0806z^{11} - 0.0854z^{10} - 0.1512z^9 + 0.0696z^8, \\
& \quad -0.1065z^7 + 0.0778z^6 - 0.0011z^5 - 0.0310z^4 + 0.0460z^3 - 0.0080z^2 \\
& \quad +0.0179z - 0.0031 \\
den_f(z) = & \quad z^8(z^5 - 1.319z^4 + 0.6345z^3 - 0.7997z^2 + 0.2697z + 0.2237).
\end{aligned}
$$

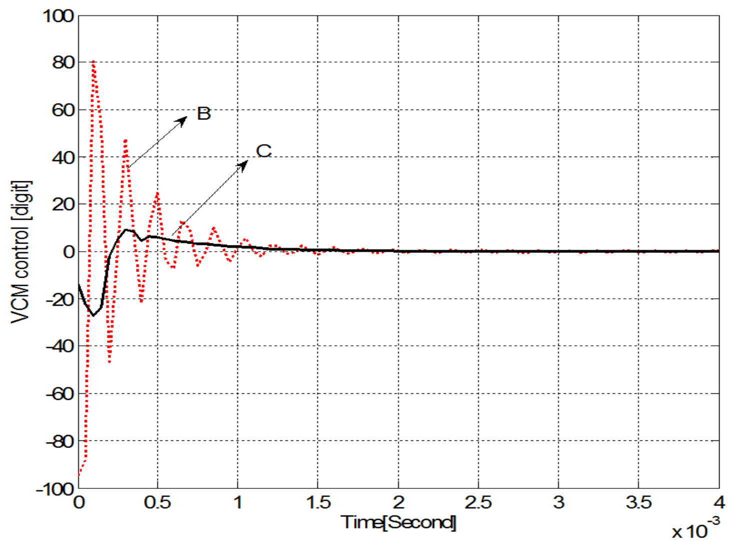

Figure 4.8: VCM controller output with initial position compensation (B: acoustic oscillation observed; C: no acoustic problem).

A smooth and fast settling within 0.3 ms is achieved as that is observed in the "C" curve in Figure 4.7. Also, there is no more acoustic problem observed in the "C" curve in Figure 4.8.

Figure 4.9 shows the result for compensating the transients due to initial velocity ($v_0 = 2000\ track/second$), where the curve "A" is the response of closed-loop system to the initial velocity, curve "B" is the injected signal (u_{c2}), curve "D" is the response of closed-loop system to injected signal only, and curve "C" is the

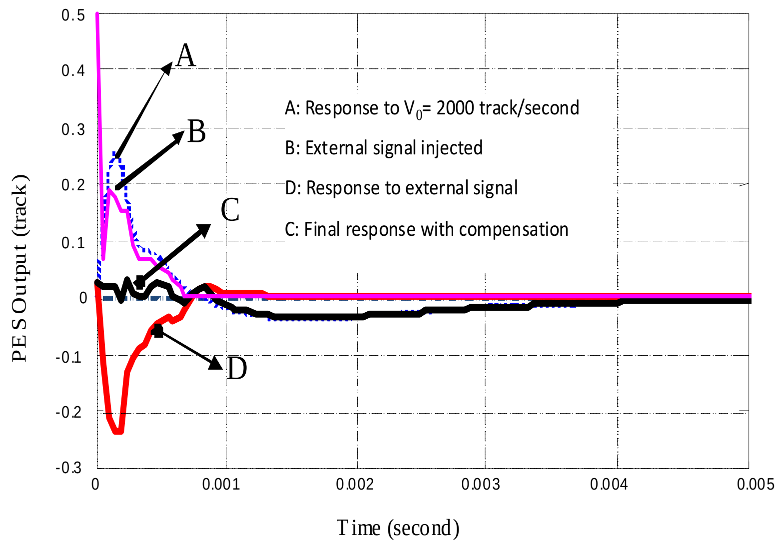

Figure 4.9: Settling transient due to initial velocity.

settling transition after compensation. It clearly shows that much faster settling is achieved with compensation.

4.5 Implementation Method

As shown in Figure 4.2 with $F(z)$ designed as (4.2.14) and $X(z)$ designed as (4.2.20), we know that

$$\begin{aligned} U_{c1}(z) &= (1 - F(z))y_0, \\ U_{c2}(z) &= z^{n-m+q}[F(z)T_v(z)]v_0. \end{aligned} \tag{4.5.22}$$

Both $F(z)$ and $T_v(z)$ are pre-designed or known. If initial values are estimated or measured, the injected u_{c1} and u_{c2} can be calculated. With the assumption that $r_p(k)$ is the time domain signal corresponding to $1 - F(z)$ and $r_v(k)$ is the time domain signal corresponding to $z^{n-m+q}[F(z)T_v(z)]$, the injected signal $u_c(k)$ when switching at (p_0, v_0) can be calculated according to superposition theory as

$$u_c(k) = y_0 \cdot r_y(k) + v_0 \cdot r_v(k). \tag{4.5.23}$$

Since $F(z)$ has a static gain of one, u_{c1} converges to zero. The static gain of $T_v(z)$ is zero, and hence u_{c2} also converges to zero as the curve "B" shown in Figure 4.9. For realtime implementation, only a finite number of $r_y(k)$ and $r_v(k)$ are stored into a look-up table for calculating the signal $u_c(k)$.

4.6 Switching Conditions

The above settling scheme is designed with consideration of improving the transient response of closed-loop system in track-following. During settling, the PZT cannot be in saturation. Otherwise, the servo system is no longer a linear system. It is therefore important to select proper switching conditions to avoid the saturation of PZT actuator.

Figure 4.10 shows the responses of PZT to different initial conditions shown as in Table 4.2. If the PZT is not saturated, the dual-stage system is a LTI system. For a general initial condition (V_0, P_0), the PZT output is,

$$f(t) \quad = \quad \frac{v_0}{1000} \times f_1(t) + p_0 \times f_3(t). \tag{4.6.24}$$

Table 4.2: PZT output at different initial conditions.

PZT output	Initial Velocity (track/second)	Initial Position (track)
$f_1(t)$	1000	0
$f_2(t)$	-1000	0
$f_3(t)$	0	1
$f_4(t)$	-2500	1
$f_5(t)$	1000	1

To avoid saturating PZT, $f(t)$ must be less than 1.25 tracks (track pitch is $0.25um$), which is full stroke for the PZT actuator corresponding to a output range of $\pm 8v$ for the PZT driver we used. From Figure 4.10, it can be seen that $f_4(t)$ and $f_5(t)$ are at the margin to saturate PZT. As such, v_0 must satisfy $-2500(track/s) \leq v_0 \leq 1000(track/s)$ to avoid saturating PZT if the p_0 is 1 track. Apparently, p_0

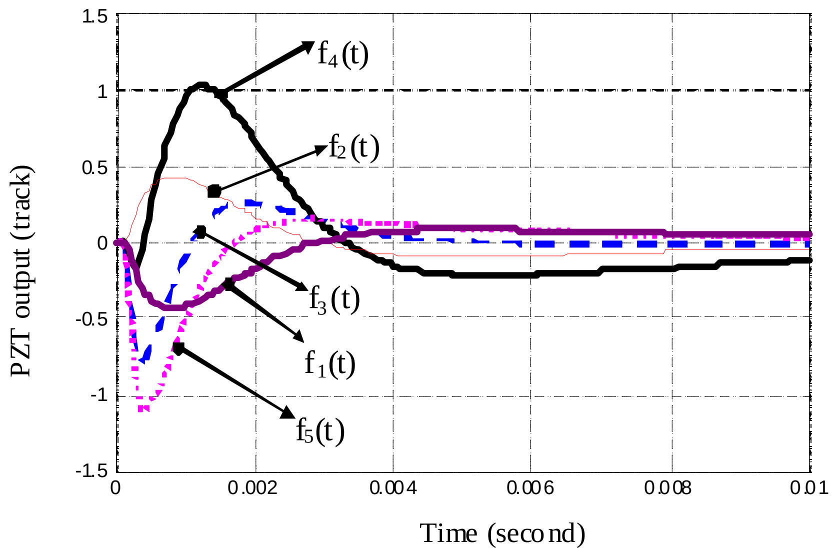

Figure 4.10: PZT output under different initial conditions with IES.

must be confined to be less than 1.25 tracks for the PZT of maximum stroke of 1.25 tracks. When the initial position error is smaller, the allowable initial velocity is also larger.

4.7 Experimental Setup and Results

In the experiment setup, as shown in Figure 4.11, the Laser Doppler Vibrometer (LDV) is used as a position sensor to measure the off-track position with laser shining at the side of slider. DSPACE, a real time development system, is used to implement the servo controllers, which includes a finite impulse response (FIR) filter as seeking controller with velocity estimator and dual-stage servo with IES. As shown in Figure 4.12, we first use the seeking controller to perform four tracks seeking. When head is arriving at the third track, we switch from seeking to tracking with/without enabling IES. Two LUTs are used in experimental implementation for IES, namely, one for initial velocity compensation and one for initial position compensation. The LUT is used to store the normalized values of u_{c1} and u_{c2} for

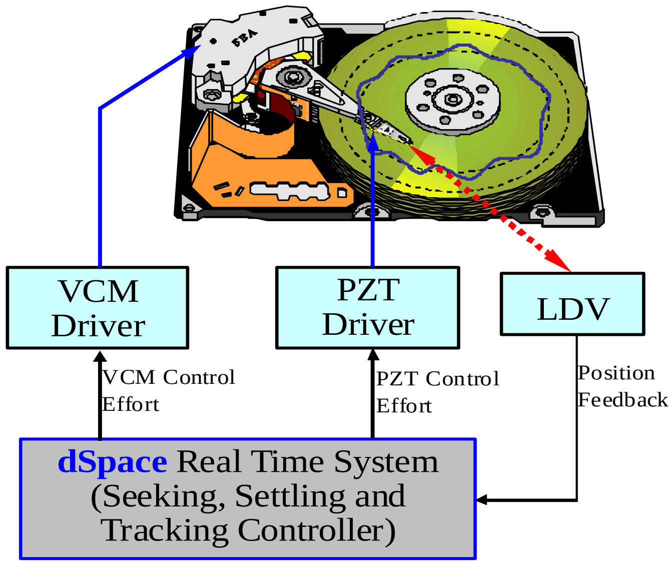

Figure 4.11: Experiment setup for dual-stage servo.

a short settling period. To implement online compensation, the values in LUT are scaled by the corresponding initial values of velocity/postion and injected into the nominal controller.

The experimental results are shown in Figure 4.13, where y_0 is 1 track, and v_0 is an estimated value around 1345 $tracks/second$ at the switching point from seeking to settling. It can be seen that the settling transient with IES (persistent curve B) is significantly improved, and a settling time of less than 0.35 ms is achieved.

4.8 Conclusions

In this chapter, an effective and easily implemented settling scheme has been presented to achieve fast and smooth track settling for a dual-stage servo system. In this scheme, a feedforward compensator can be used to cancel the error caused by the initial position and velocity of VCM during mode-switching.

Based on ZPET, a systematic pole/zero cancelation scheme is used in the design of the IES feedforward compensator.

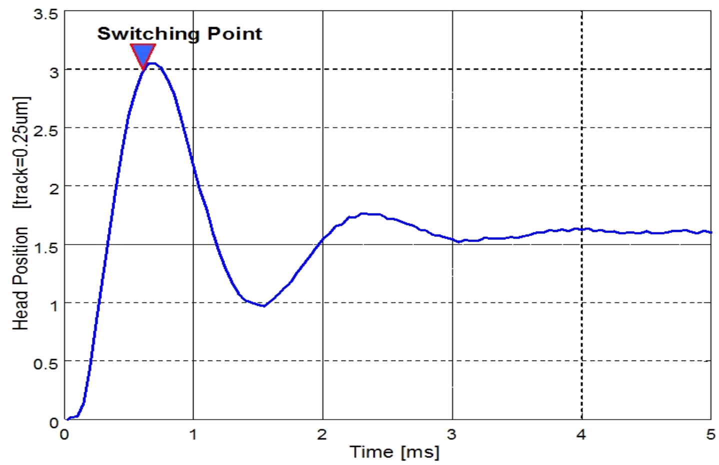

Figure 4.12: Seeking profile with FIR seeking controller.

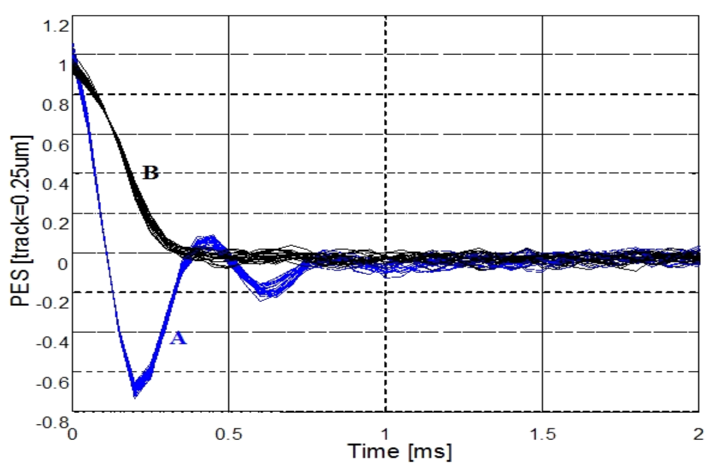

Figure 4.13: Experimental results with IES (A: no compensation; B: with compensation).

Both simulation and experiment results show that this method can improve settling performance significantly. In future, it is valuable to study the optimal switching conditions.

Chapter 5

Design Feedback Controller Using Advanced Loop Shaping

To shape the frequency responses of closed-loop transfer functions such as sensitivity/complementary sensitivity functions, H_∞ optimization together with frequency weighting is a commonly used method. However, the frequency weighting functions increase the system and controller complexities since the weighting functions usually are of high orders in order to formulate the desired specifications accurately. The process of choosing appropriate weighting function is also tedious and time-consuming.

The KYP lemma [65] establishes the equivalence between a frequency domain inequality (FDI) for a transfer function and a linear matrix inequality associated with its state space realization. It provides a solution to characterize various properties of dynamic systems in the frequency domain in terms of linear matrix inequalities. The standard KYP Lemma is only applicable for the infinite frequency range, while the generalized KYP Lemma [66] establishes the equivalence between a frequency domain property and a linear matrix inequality over a finite frequency range, which allows designers to impose expected performance requirements over selected finite or infinite frequency ranges. Therefore, the generalized KYP is very suitable for analysis and synthesis problems in practical applications where different specifications over different frequency ranges are required.

The KYP Lemma-based loop shaping method does not count for overall positioning error minimization which can be translated into the H_2 optimal control problem by taking into consideration the disturbance and noise models. On the other hand, the H_2 control design which incorporates all disturbance and noise models can result in an average performance across the entire frequency range and a high order controller. Thus, it usually does not have the flexibility to specifically reject disturbances in certain frequency ranges, which however may be the dominant factors that influence the overall performance. Therefore, there is a need to suppress disturbances of specific frequencies when minimizing the positioning error, which is the motivation to incorporate the KYP lemma-based method with the H_2 control method. With the selected specific disturbances handled by the KYP Lemma-based design, the H_2 control is formulated with a lower order disturbance model, excluding the disturbances covered in the above design. This will not only reduce the computation time in the H_2 control design, but also result in a lower order controller.

In this chapter, the generalized KYP lemma is applied to design a feedback control such that the sensitivity function can attenuate the disturbances at some specific frequency ranges. Unlike the standard KYP lemma, the matrix inequality in the generalized KYP lemma involves a matrix variable which is not necessarily positive definite, and thus the Schur complement cannot be applied to convexify the controller design. To overcome this difficulty, the Youla parametrization approach is used to parameterize the closed-loop transfer function. The search for the coefficients of the parameter $Q(z)$ is then converted to a linear matrix inequality problem within the generalized KYP lemma framework. Next, considering the system with an augmented disturbance model, the generalized KYP lemma is combined the H_2

method to design a controller for minimization of tracking error as well as attenuation of dominant disturbances at certain frequencies. Lastly, the two methods are applied to design track-following controller for our STW experiment platform.

5.1 Control Design Using Generalized KYP Lemma

5.1.1 Problem Description

It is known that the power spectrum of PES in Figure 2.16 is given by

$$S_e = |P(z)S(z)|^2 S_{d_1} + |S(z)|^2 S_{d_2} + |S(z)|^2 S_n, \tag{5.1.1}$$

where the sensitivity function $S(z)$ shows the disturbance rejection capability of the servo loop. It becomes rather significant to design a controller such that the sensitivity function reject dominant disturbances with known frequencies.

The problem can be stated as: *To design a dynamic feedback controller $C(z)$ for plant $P(z)$ such that the closed-loop system is stable and for some prescribed positive scalars r_i and frequency ranges $(f_{i1},\ f_{i2}),\ i = 1, ..., N,$ such that*

$$|S(f)| < r_i, \quad when\ f_{i1} \leq f \leq f_{i2}. \tag{5.1.2}$$

A smaller r_i means the less contribution of the disturbance in frequency range (f_{i1}, f_{i2}) to the error.

5.1.2 Generalized KYP Lemma

Figure 5.1 shows a equivalent system where the transfer function from w to z is the same as the sensitivity function, $S(z)$, in Figure 2.16. The state-space model of the plant under consideration is denoted as $(A_p,\ B_p,\ C_p,\ D_p)$. The state-space representation of the system in Figure 5.1 is given by

$$x(k+1) = A_p x(k) + B_p u(k), \tag{5.1.3}$$

$$z(k) = -C_p x(k) + w(k) - D_p u(k), \tag{5.1.4}$$

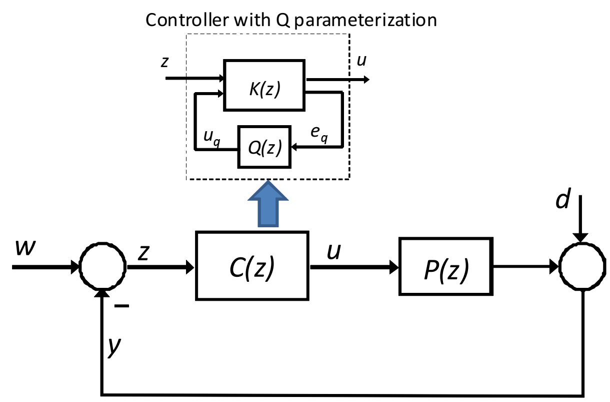

Figure 5.1: Equivalent system for KYP analysis.

where $x \in R^n$ is the state vector of dimension n, $z \in \mathcal{R}^p$ is the controlled output vector of dimension p, $w \in \mathcal{R}^q$ is the disturbance vector of dimension q, $u \in R^r$ is the control input vector of dimension r, A_p is the state matrix of dimension $n \times n$, B_p is the input matrix of dimension $n \times r$, C_p is the output matrix of dimension $p \times n$, and D_p is the feedthrough matrix of dimension $p \times r$.

Let a state-space representation of the controller $C(z)$ be given by (A_c, B_c, C_c, D_c). Assuming that $D = 1 + D_c D_p$ is invertible, then a state-space representation of the sensitivity function can be given by $(\tilde{A},\ \tilde{B},\ \tilde{C},\ \tilde{D})$, where

$$\tilde{A} = \begin{bmatrix} A_p - B_p D^{-1} D_c C_p & B_p D^{-1} C_c \\ -B_c C_p + B_c D_p D^{-1} D_c D_p & A_c - B_c D_p D^{-1} C_c \end{bmatrix}, \tag{5.1.5}$$

$$\tilde{B} = \begin{bmatrix} B_p D^{-1} D_c \\ B_c - B_c D_p D^{-1} D_c \end{bmatrix}, \tag{5.1.6}$$

$$\tilde{C} = \begin{bmatrix} -C_p + D_p D^{-1} D_c C_p & - D_p D^{-1} C_c \end{bmatrix}, \tag{5.1.7}$$

$$\tilde{D} = 1 - D_p D^{-1} D_c. \tag{5.1.8}$$

A special case of the generalized KYP lemma that relates the bounded realness of the sensitivity function over finite frequency ranges to its state space representation is given below [66].

Lemma 5.1.1 *Consider the sensitivity function* $S(z) = \tilde{C}(zI - \tilde{A})^{-1}\tilde{B} + \tilde{D}$ *with* $\tilde{A}$ *being stable. Then, for a given scalar* $r > 0$, $|S(e^{j\theta})| \leq r$ *over a finite frequency range if and only if there exist Hermitian matrices* U *and* $V \geq 0$ *such that*

$$\begin{bmatrix} \begin{bmatrix} \tilde{A} & \tilde{B} \\ I & 0 \end{bmatrix}^* \Sigma \begin{bmatrix} \tilde{A} & \tilde{B} \\ I & 0 \end{bmatrix} + \begin{bmatrix} 0 & 0 \\ 0 & -r^2 \end{bmatrix} & \begin{bmatrix} \tilde{C} & \tilde{D} \end{bmatrix}^* \\ \begin{bmatrix} \tilde{C} & \tilde{D} \end{bmatrix} & -I \end{bmatrix} \leq 0, \tag{5.1.9}$$

where

(i) for low frequency range $|\theta| \leq \theta_l$,

$$\Sigma = \begin{bmatrix} -U & V \\ V & U - (2cos\theta_l)V \end{bmatrix}; \tag{5.1.10}$$

(ii) for middle frequency range $\theta_1 \leq \theta \leq \theta_2$,

$$\Sigma = \begin{bmatrix} -U & e^{j\theta_c}V \\ e^{-j\theta_c}V & U - (2cos\theta_d)V \end{bmatrix},$$
$$\theta_c = (\theta_1 + \theta_2)/2, \quad \theta_d = (\theta_2 - \theta_1)/2; \tag{5.1.11}$$

(iii) for high frequency range $|\theta| \geq \theta_h$,

$$\Sigma = \begin{bmatrix} -U & -V \\ -V & U + (2cos\theta_h)V \end{bmatrix}. \tag{5.1.12}$$

For a given controller $C(z)$, the above gives a necessary and sufficient condition to evaluate whether $|S(z)| \leq r$ over some given frequency range in terms of an LMI. However, (5.1.9) is no longer an LMI when the controller $C(z) = (A_c,\ B_c,\ C_c,\ D_c)$ is to be designed, since $\tilde{A}$ and $\tilde{B}$ involve the unknown parameters $A_c,\ B_c,\ C_c$ and D_c. Further, it is not possible to convert to an LMI via Schur complement as the matrix Σ is not definite.

5.1.3 YOULA Parametrization

Let $K(z)$ be a state feedback controller with a state estimator, i.e.,

$$\hat{x}(k+1) = A_p\hat{x}(k) + B_pu(k) + L(z(k) + C_p\hat{x}(k)), \tag{5.1.13}$$

$$u(k) = -M\hat{x}(k). \tag{5.1.14}$$

where L is the estimator gain, and M is state feedback gain. A set of sensitivity functions can be parameterized as [67]

$$S(z) = T_{11}(z) + T_{12}(z)Q(z)T_{21}(z), \tag{5.1.15}$$

where $Q(z)$ is a stable transfer function to be designed and

$$\begin{bmatrix} T_{11}(z) & T_{12}(z) \\ T_{21}(z) & 0 \end{bmatrix} = C_T(zI - A_T)^{-1}B_T + D_T,$$

$$\begin{bmatrix} A_T & B_T \\ C_T & D_T \end{bmatrix} = \left[\begin{array}{cc|cc} A_p & -B_pM & 0 & B_p \\ -LC_p & A_p - B_pM + LC_p & L & B_p \\ \hline -C_p & D_pM & 1 & -D_p \\ -C_p & C_p & 1 & 0 \end{array}\right]. \tag{5.1.16}$$

If $Q(z)$ has the state-space realization (A_q, B_q, C_q, D_q), the designed controller $C(z)$ is given by

$$A_c = \begin{bmatrix} A_p - B_pM + LC_p + B_pD_qC_p & B_pC_q \\ B_qC_p & A_q \end{bmatrix}, \tag{5.1.17}$$

$$B_c = \begin{bmatrix} L + B_pD_q \\ B_q \end{bmatrix}, \tag{5.1.18}$$

$$C_c = \begin{bmatrix} -M + D_qC_p & C_q \end{bmatrix}, \tag{5.1.19}$$

$$D_c = D_q. \tag{5.1.20}$$

The controller $C(z)$ is now of the structure as shown in Figure 5.1.

Denote the state-space representations of $T_{11}(z)$ and $T_{12}(z)T_{21}(z)$ by $(A_{t11}$, B_{t11}, $C_{t11}, D_{t11})$ and (A_t, B_t, C_t, D_t), respectively, a state space model of $S(z)$ can be written as from (5.1.15)

$$\tilde{A} = \begin{bmatrix} A_{t11} & 0 & 0 \\ 0 & A_t & 0 \\ 0 & B_qC_t & A_q \end{bmatrix}, \tag{5.1.21}$$

$$\tilde{B} = \begin{bmatrix} B_{t11} \\ B_t \\ B_q D_t \end{bmatrix}, \tag{5.1.22}$$

$$\tilde{C} = \begin{bmatrix} C_{t11} & D_q C_t & C_q \end{bmatrix}, \tag{5.1.23}$$

$$\tilde{D} = D_{t11} + D_q D_t. \tag{5.1.24}$$

Let $Q(z)$ be an FIR filter, such that

$$Q(z) = q_0 + q_1 z^{-1} + q_2 z^{-2} + ... + q_\tau z^{-\tau}, \tag{5.1.25}$$

$$q = [q_0 \;\; q_1 \;\; q_2, \; ... \; , \; q_\tau], \tag{5.1.26}$$

which is to be designed so that the required bounded realness of the sensitivity function is satisfied. It is known that a state-space realization for $Q(z)$ can be given by

$$\begin{aligned} A_q &= \begin{bmatrix} 0 & I_{\tau-1} \\ 0 & 0 \end{bmatrix}, \quad B_q = \begin{bmatrix} 0_{(\tau-1)\times 1} \\ 1 \end{bmatrix}, \\ C_q &= [q_\tau \;\; q_{\tau-1} \;\; \cdots \;\; q_1], \quad D_q = q_0, \end{aligned}$$

where $I_{\tau-1}$ is the identity matrix of dimension $(\tau-1)\times(\tau-1)$ and $0_{(\tau-1)\times 1}$ is the zero matrix of dimension $(\tau-1)\times 1$. Note that the filter parameter q to be designed only appears in C_q and D_q. From (5.1.21)-(5.1.24), we know that q exists in $\tilde{C}$ and $\tilde{D}$ only. In this case, (5.1.9) defines an LMI in terms of the variables U, V, and q. As such, U, V, and the design parameter q can be computed via a convex optimization.

5.1.4 Design Procedures Using KYP Lemma

The KYP lemma-based control design can be carried out according following steps:

Step 1. Compute M and L using Matlab commands

$$M = dlqr(A_p, B_p, C_p^T C_p, R),$$

$$L = A_p \cdot dlqe(A_p, B_p, -C_p, W_d, W_v),$$

where R is the weighting for the control input in the cost function

$$J = \sum (\hat{x}^T C_p^T C_p \hat{x} + u^T R u)$$

for linear quadratic regulator design, and W_d and W_v are the variance matrices of process noise and measurement noise for the Kalman estimator design. In the KYP lemma-based control design, R, W_d, and W_v can be chosen as identity matrices.

Step 2. Compute $T_{11}(z)$, $T_{12}(z)$, and $T_{21}(z)$ from (5.1.16).

Step 3. Obtain the state-space model $(\tilde{A}, \tilde{B}, \tilde{C}, \tilde{D})$ in (5.1.21)-(5.1.24).

Step 4. Based on disturbance spectrum, specify the positive scalars r_i and frequency points $f_i (i = 1, ..., N)$ for the sensitivity function

$$|S(f_i)| < r_i, \quad f_{i1} \leq f_i \leq f_{i2}, \tag{5.1.27}$$

where f_{i1} and f_{i2} define the frequency range. For each specification on the resultant sensitivity function in the frequency range, construct the LMI (5.1.9) in terms of the variables U, V, and q, with $r = r_i$.

Step 5. Obtain q, U, and V by solving these LMIs using Matlab LMI toolbox. If the LMIs are not solvable, the specifications given in Step 4 are to be adjusted.

Step 6. Obtain the controller parameters from (5.1.17)-(5.1.20).

5.2 H_2 Optimal Control

KYP lemma can be used to shape the loop transfer function to attenuate specific disturbances. However, it can not achieve overall minimization of tracking error which can be achieved by H_2 optimal control.

5.2.1 H_2 Norm

The H_2 norm of a matrix transfer function $G(s)$ analytic in $Re(s) > 0$ (open right-half plane) is defined as

$$\|G\|_2 := \sqrt{\sup_{\sigma>0}\{\frac{1}{2\pi}\int_{-\infty}^{+\infty} Trace[G^*(\sigma + j\omega)G(\sigma + j\omega)]d\omega\}}, \tag{5.2.28}$$

or equivalently [68]

$$\|G\|_2 = \sqrt{\frac{1}{2\pi}\int_{-\infty}^{+\infty} Trace[G^*(j\omega)G(j\omega)]d\omega}. \tag{5.2.29}$$

Although $\|G\|_2$ can be computed from its definition, there are some simple alternatives taking advantage of a state-space representation of $G(s)$.

Lemma 5.2.1 *Consider a system $G(s)$ with a state-space representation (A, B, C, D). If A is stable and $D = 0$, we have [69]*

$$\|G\|_2^2 = Trace(B^T Y_2 B) = Trace(C X_2 C^T), \tag{5.2.30}$$

where X_2 and Y_2 are the controllability and observability Gramians that can be obtained from the following Lyapunov equations

$$AX_2 + X_2A^T + BB^T = 0, \tag{5.2.31}$$
$$A^T Y_2 + Y_2 A + C^T C = 0. \tag{5.2.32}$$

We also consider a discrete-time linear time-invariant system $G(z)$ with the following state-space representation

$$x(k+1) = Ax(k) + Bw(k), \tag{5.2.33}$$
$$z(k) = Cx(k) + Dw(k), \tag{5.2.34}$$

where $x \in \mathcal{R}^n$ is the state vector of dimension n , $z \in \mathcal{R}^p$ is the controlled output vector of dimension p , $w \in \mathcal{R}^q$ is the disturbance vector of dimension q. Let T_{zw}

denote the transfer function from the input w to the output z. Then the H_2 norm is defined as

$$\|T_{zw}\|_2 = \sqrt{\frac{1}{2\pi}Trace[\int_{-\pi}^{\pi} T_{zw}^{*}(e^{j\omega})T_{zw}(e^{j\omega})d\omega]}. \tag{5.2.35}$$

By Parseval's Theorem, $\|T_{zw}\|_2$ can equivalently be defined as

$$\|T_{zw}\|_2 = \sqrt{Trace[\sum_{k=0}^{\infty} g(k)g^T(k)]}, \tag{5.2.36}$$

where $g(k)$ is the impulse response of T_{zw}.

Let the input w to the system be a wide-band stationary stochastic process. The H_2 norm of T_{zw} can also be interpreted as the RMS value of the output $z(k)$ when the system is subject to a white noise having zero mean and unit variance. That is

$$\|T_{zw}\|_2 = \sqrt{E[\mathbf{z}^T\mathbf{z}]}. \tag{5.2.37}$$

The H_2 norm for the discrete-time system T_{zw} can be computed as

$$\|T_{zw}\|_2 = \sqrt{Trace(D^TD + B^TY_2B)} = \sqrt{Trace(DD^T + CX_2C^T)}, \tag{5.2.38}$$

where Y_2 and X_2 are the reachability and observability Gramians that can be obtained from the following Lyapunov equations

$$AY_2A^T - Y_2 + BB^T = 0, \tag{5.2.39}$$

$$A^TX_2A - X_2 + C^TC = 0. \tag{5.2.40}$$

The following theorem presents an alternative LMI approach for bounding the H_2 norm of the discrete-time system T_{zw}.

Lemma 5.2.2 *Consider a discrete-time transfer function T_{zw} of realization (A, B, C, D). Given a scalar $\mu > 0$, $\|T_{zw}\|_2^2 < \mu$ if and only if there exist $X_2 = X_2^T$ and $Y_2 = Y_2^T$*

such that $Trace(\Pi) < \mu$ *and*

$$\begin{bmatrix} \Pi & CX_2 & D \\ X_2C^T & X_2 & 0 \\ D^T & 0 & I \end{bmatrix} > 0, \tag{5.2.41}$$

$$\begin{bmatrix} Y_2 & AY_2 & B \\ Y_2A^T & Y_2 & 0 \\ B^T & 0 & I \end{bmatrix} > 0. \tag{5.2.42}$$

Observe that (5.2.41) and (5.2.42) are linear in X_2 and Y_2, and hence can be solved by employing the LMI Tool [70] in Matlab. The H_2 norm of the system can be computed by minimizing μ using the function **mincx.m** in Matlab Optimization Toolbox.

5.2.2 Continuous-time H_2 Optimal Control

We consider the closed-loop system described by the block diagram in Figure 5.2. The continuous-time linear time-invariant plant $P(s)$ is described by the following state-space equations:

$$\dot{x}(t) = Ax(t) + B_1w(t) + B_2u(t), \tag{5.2.43}$$

$$z(t) = C_1x(t) + D_{11}w(t) + D_{12}u(t), \tag{5.2.44}$$

$$y(t) = C_2x(t) + D_{21}w(t) + D_{22}u(t), \tag{5.2.45}$$

where $x \in \mathcal{R}^n$ is the state, $y \in \mathcal{R}^m$ is the measurement output, $z \in \mathcal{R}^p$ is the controlled output, $w \in \mathcal{R}^q$ is the disturbance input, $u \in \mathcal{R}^r$ is the control input, and A, B_1, B_2, C_1, D_{11}, D_{12}, C_2, and D_{21} are constant matrices of appropriate dimensions. We assume $D_{22} = 0$ without loss of generality [71].

Introduce the following dynamic output feedback controller $C(s)$

$$\dot{x}_c(t) = A_cx_c(t) + B_cy(t), \tag{5.2.46}$$

$$u(t) = C_cx_c(t) + D_cy(t). \tag{5.2.47}$$

Denote $\xi = [x^T \;\; x_c^T]^T$. From (5.2.43)-(5.2.45) and (5.2.46)-(5.2.47), the closed-loop system is given by

$$\begin{aligned} \dot{\xi}(t) &= \bar{A}\xi(t) + \bar{B}w(t), && (5.2.48) \\ z(t) &= \bar{C}\xi(t) + \bar{D}w(t), && (5.2.49) \end{aligned}$$

where

$$\bar{A} = \begin{bmatrix} A + B_2 D_c C_2 & B_2 C_c \\ B_c C_2 & A_c \end{bmatrix}, \; \bar{B} = \begin{bmatrix} B_2 D_c D_{21} + B_1 \\ B_c D_{21} \end{bmatrix}, \quad (5.2.50)$$

$$\bar{C} = [C_1 + D_{12} D_c C_2 \quad D_{12} C_c], \quad \bar{D} = D_{12} D_c D_{21} + D_{11}. \quad (5.2.51)$$

The continuous-time H_2 control problem is to find a proper and real rational controller $C(s)$ that stabilizes P internally and minimizes the H_2 norm of the closed-loop transfer function matrix T_{zw} from w to z in (5.2.48)-(5.2.49).

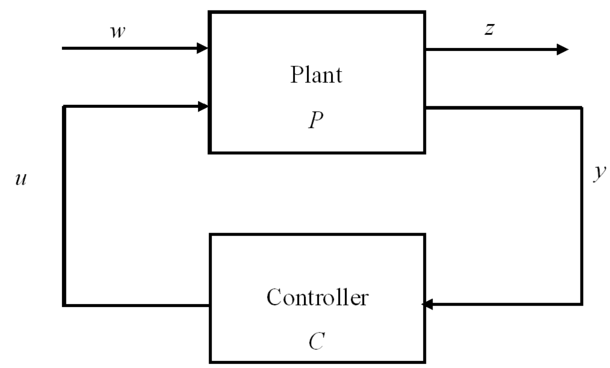

Figure 5.2: Configuration of standard optimal control.

Assume that the system (5.2.43)-(5.2.45) satisfies the following condition

Assumption 3.1

(1). D_{12} is of full column rank;

(2). The subsystem (A, B_2, C_1, D_{12}) has no invariant zeros on the imaginary axis;

(3). D_{21} is of full row rank;

(4). The subsystem $(A,\ B_1,\ C_2,\ D_{21})$ has no invariant zeros on the imaginary axis.

Let $X_2 \geq 0$ and $Y_2 \geq 0$ be the solutions of the following Riccati equations

$$A^T X_2 + X_2 A - (X_2 B_2 + C_1^T D_{12})(D_{12}^T D_{12})^{-1}(X_2 B_2 + C_1^T D_{12})^T$$
$$+C_1^T C_1 = 0, \tag{5.2.52}$$
$$Y_2 A^T + A Y_2 - (Y_2 C_2^T + B_1 D_{21}^T)(D_{21} D_{21}^T)^{-1}(Y_2 C_2^T + B_1 D_{21}^T)^T$$
$$+B_1 B_1^T = 0. \tag{5.2.53}$$

According to the H_2 optimal control theory, an H_2 optimal controller can be obtained as [72]

$$A_c = A + B_2 F + K C_2, \quad B_c = -K, \quad C_c = F, \quad D_c = 0, \tag{5.2.54}$$

where

$$F = -(D_{12}^T D_{12})^{-1}(D_{12}^T C_1 + B_2^T X_2),$$
$$K = -(Y_2 C_2^T + B_1 D_{21}^T)(D_{21} D_{21}^T)^{-1}. \tag{5.2.55}$$

The minimal H_2 norm of the transfer function T_{zw} is given by

$$\|T_{zw}\|_2 = \sqrt{Trace(B_1^T X_2 B_1) + Trace[(A^T X_2 + X_2 A + C_1^T C_1) Y_2]}. \tag{5.2.56}$$

If any condition among (1)-(4) in Assumption 3.1 is not satisfied, the so-called perturbation method is applied [72] so that the above design method is still applicable to find an appropriate controller.

5.2.3 Discrete-time H_2 Optimal Control

Consider the discrete-time linear time-invariant system $P(z)$ with the following state-space representation

$$x(k+1) \quad = \quad Ax(k) + B_1 w(k) + B_2 u(k), \tag{5.2.57}$$

$$z(k) = C_1x(k) + D_{11}w(k) + D_{12}u(k), \tag{5.2.58}$$

$$y(k) = C_2x(k) + D_{21}w(k) + D_{22}u(k), \tag{5.2.59}$$

where $x \in \mathcal{R}^n$ is the state, $y \in \mathcal{R}^m$ is the measurement output, $z \in \mathcal{R}^p$ is the controlled output, $w \in \mathcal{R}^q$ is the disturbance input, $u \in \mathcal{R}^r$ is the control input, and A, B_1, B_2, C_1, D_{11}, D_{12}, C_2, and D_{21} are constant matrices of appropriate dimensions. $D_{22} = 0$ is also assumed for brevity but without loss of generality.

Introduce the following dynamic output feedback controller $C(z)$,

$$x_c(k+1) = A_cx_c(k) + B_cy(k), \tag{5.2.60}$$

$$u(k) = C_cx_c(k) + D_cy(k). \tag{5.2.61}$$

Denote $\xi = [x^T \ \ x_c^T]^T$. From (5.2.57)-(5.2.59) and (5.2.60)-(5.2.61), the closed-loop system is given by

$$\xi(k+1) = \bar{A}\xi(k) + \bar{B}w(k), \tag{5.2.62}$$

$$z(k) = \bar{C}\xi(k) + \bar{D}w(k), \tag{5.2.63}$$

where

$$\bar{A} = \begin{bmatrix} A + B_2D_cC_2 & B_2C_c \\ B_cC_2 & A_c \end{bmatrix}, \ \bar{B} = \begin{bmatrix} B_2D_cD_{21} + B_1 \\ B_cD_{21} \end{bmatrix}, \tag{5.2.64}$$

$$\bar{C} = [C_1 + D_{12}D_cC_2 \quad D_{12}C_c], \quad \bar{D} = D_{12}D_cD_{21} + D_{11}. \tag{5.2.65}$$

The discrete-time H_2 control problem is to find a proper and real rational controller $C(z)$ that stabilizes $P(z)$ internally and minimizes the H_2 norm of the transfer function matrix $T_{zw}(z)$ from w to z of the closed-loop system (5.2.62)-(5.2.63).

The counterpart of the Riccati equations (5.2.52)-(5.2.53) for discrete-time systems is as follows.

$$A^TX_2A - (A^TX_2B_2 + C_1^TD_{12})(D_{12}^TD_{12} + B_2^TX_2B_2)^{-1}(A^TX_2B_2 + C_1^TD_{12})^T$$

$$+C_1^T C_1 = 0, \tag{5.2.66}$$

$$AY_2A^T - (AY_2C_2^T + B_1D_{21}^T)(D_{21}D_{21}^T + C_2Y_2C_2^T)^{-1}(AY_2C_2^T + B_1D_{21}^T)^T$$
$$+B_1B_1^T = 0. \tag{5.2.67}$$

A discrete-time H_2 optimal controller can then be obtained as (5.2.54). And the minimal H_2 norm of the transfer function T_{zw} is given by

$$\|T_{zw}\|_2 = \sqrt{Trace(B_1^T X_2 B_1) + Trace[(A^T X_2 A + C_1^T C_1)Y_2]}. \tag{5.2.68}$$

A parametrization of all H_2 controllers is developed in terms of LMIs as in the following theorem which linearizes the H_2 norm conditions (5.2.41)-(5.2.42) for synthesis.

Theorem 5.2.3 *[73] Consider system (5.2.57)-(5.2.59). There exists a controller (5.2.60)-(5.2.61) such that $\|T_{zw}\|_2^2 < \mu$ if and only if the following linear matrix inequalities and equality admit a solution:*

$$Trace(\Pi) < \mu, \tag{5.2.69}$$
$$\begin{bmatrix} \Pi & C_1X + D_{12}E & C_1 + D_{12}D_cC_2 \\ * & X + X^T - P_2 & I + Z^T - J \\ * & * & Y + Y^T - H \end{bmatrix} > 0, \tag{5.2.70}$$
$$\begin{bmatrix} P_2 & J & AX + B_2E & A + B_2D_cC_2 & B_1 + B_2D_cD_{21} \\ * & H & U & YA + WC_2 & YB_1 + WD_{21} \\ * & * & X + X' - P_2 & I + Z' - J & 0 \\ * & * & * & Y + Y^T - H & 0 \\ * & * & * & * & I \end{bmatrix} > 0, \tag{5.2.71}$$

and

$$D_{11} + D_{12}D_cD_{21} = 0, \tag{5.2.72}$$

where $*$ denotes an entry that can be deduced from the symmetry of the matrix, the matrices X, E, Y, W, U, D_c, Z, J, and the symmetric matrices P_2, H and Π are the variables. A feasible H_2 controller is obtained by choosing N_1 and M_1 nonsingular such that $N_1M_1 = Z - YX$ and calculating

$$C_c = (E - D_cC_2X)M_1^{-1}, \quad D_c = D_c, \tag{5.2.73}$$
$$B_c = N_1^{-1}(W - YB_2D_c), \tag{5.2.74}$$
$$A_c = N_1^{-1}[U - Y(A + B_2D_cC_2)X - N_1B_cC_2X - YB_2C_cM_1]M_1^{-1}. \tag{5.2.75}$$

5.3 Combine H_2 and KYP Lemma

5.3.1 Problem Formulation

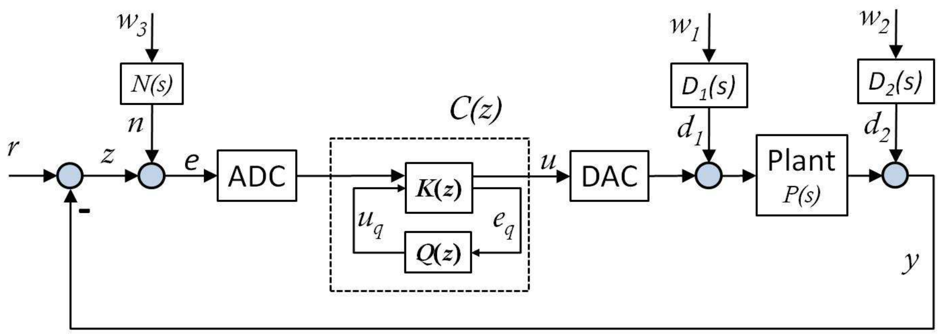

Figure 5.3: H_2 control scheme with Q parametrization for controller design.

In the previous section, specifications on sensitivity function $S(z)$ are described as

$$|S(f_i)| < r_i, \quad f_{i1} < f_i < f_{i2}, \ i = 1, \ 2, \cdots, \ m \tag{5.3.76}$$

where $r_i < 1$ is a positive scalar, and f_{i1} and f_{i2} define the frequency range.

Such an upper-bound specification as in (5.3.76) will lead to a problem when the frequency f_i is larger than and especially near the 0-dB crossover frequency of $S(z)$. The 0-dB crossover frequency of $S(z)$ will be pushed away towards a higher frequency, which tends to destabilize the system and degrade the system performance at high frequencies. In view of this, a lower-bound specification

$$|S(f_i)| \geq 1, \quad f_{i1} \leq f_i \leq f_{i2} \tag{5.3.77}$$

is required, where f_{i1} is beyond the 0-dB crossover frequency.

The problem of the specific disturbance rejection by imposing such performance specifications in (5.3.76) can be solved by using the KYP lemma-based control design method in previous section. However, as shown in Figure 5.3 which is associated with Fig. 2.17, the performance of servo system is affected by various kinds of disturbances and sensing noise. The KYP lemma-based control design cannot include all disturbances and noises which contribute to the position error. In view of this, we also need to take into account the overall performance of the servo control system, which is represented as the so-called TMR in HDD servo. The TMR is contributed by by $w = \begin{bmatrix} w_1 & w_2 & w_3 \end{bmatrix}^T$ through $D_1(s)$, $D_2(s)$, and $N(s)$. It is expressed by the standard deviation σ_z of z, and

$$\sigma_z = \|T_{zw}\|_2 , \tag{5.3.78}$$

where w is white noise with zero mean and identity covariance matrix, and T_{zw} is the transfer function from w to z.

The problem can be stated as: *To design a dynamic feedback controller $C(z)$ for plant $P(z)$ such that the closed-loop system is stable and satisfy the specifications in (5.3.76) and (5.3.77), and minimizing σ_z in (5.3.78)* simultaneously.

5.3.2 Design Controller for Specific Disturbance Rejection and Overall Error Minimization

Let $(A_p,\ B_p,\ C_p,\ D_p)$ and (A_c, B_c, C_c, D_c) be the state-space model of plant $P(z)$ and controller $C(z)$ respectively. In order to convexify matrix inequalities, the Youla parametrization approach with the $Q(z)$ in a FIR filter form is applied and the controller structure is shown in Figure 5.3. $K(z)$ is an observer based controller that can be designed using the LQG method as in (5.1.13)-(5.1.14).

For the presentation of the KYP lemma, we denote

$$\sigma(S, \Pi) := \begin{bmatrix} S \\ I \end{bmatrix}^* \Pi \begin{bmatrix} S \\ I \end{bmatrix} \tag{5.3.79}$$

where $S(z) = S(e^{j\theta})$, I stands for an identity matrix, and Π a Hermitian matrix of the form

$$\Pi = \begin{bmatrix} \Pi_{11} & \Pi_{12} \\ \Pi_{12}^* & \Pi_{22} \end{bmatrix}, \tag{5.3.80}$$

which specifies the frequency domain property to be investigated.

5.3.3 Q Parametrization to Meet Specifications for Disturbance Rejection

A. Specification (5.3.76)

Recall from (5.1.15)-(5.1.16) that a set of sensitivity functions $S(z)$: $(\tilde{A},\ \tilde{B},\ \tilde{C},\ \tilde{D})$ can be Q-parameterized. According to the denotation (5.3.79)-(5.3.80), the specification $|S(z)| \leq r$ is written as $\sigma(S,\ \Pi) \leq 0$ with

$$\Pi = \begin{bmatrix} \Pi_{11} & \Pi_{12} \\ \Pi_{12}^{*} & \Pi_{22} \end{bmatrix} = \begin{bmatrix} 1 & 0 \\ 0 & -\,r^2 \end{bmatrix}. \tag{5.3.81}$$

Thus based on the KYP lemma, $\left|S\left(e^{j\theta}\right)\right| \leq r$ for the frequency range $\theta_1 \leq \theta \leq \theta_2$ can be achieved by solving the following matrix inequality

$$\begin{bmatrix} \tilde{A} & \tilde{B} \\ I & 0 \end{bmatrix}^{*} \Sigma \begin{bmatrix} \tilde{A} & \tilde{B} \\ I & 0 \end{bmatrix} + \begin{bmatrix} \tilde{C} & \tilde{D} \\ 0 & I \end{bmatrix}^{*} \Pi \begin{bmatrix} \tilde{C} & \tilde{D} \\ 0 & I \end{bmatrix} \leq 0, \tag{5.3.82}$$

which is equivalent to

$$\begin{bmatrix} \begin{bmatrix} \tilde{A} & \tilde{B} \\ I & 0 \end{bmatrix}^{*} \Sigma \begin{bmatrix} \tilde{A} & \tilde{B} \\ I & 0 \end{bmatrix} + \begin{bmatrix} 0 & 0 \\ 0 & -r^2 \end{bmatrix} & \begin{bmatrix} \tilde{C} & \tilde{D} \end{bmatrix}^{*} \Pi_{11} \\ \Pi_{11} \begin{bmatrix} \tilde{C} & \tilde{D} \end{bmatrix} & -\Pi_{11} \end{bmatrix} \leq 0, \tag{5.3.83}$$

where

$$\Sigma = \begin{bmatrix} -U & e^{j\theta_c} V \\ e^{-j\theta_c} V & U - (2\cos\theta_d)\, V \end{bmatrix}, \tag{5.3.84}$$

$$\theta_c = {(\theta_1 + \theta_2)}/{2}, \quad \theta_d = {(\theta_2 - \theta_1)}/{2}, \tag{5.3.85}$$

since $\Pi_{11} > 0$. U and V are Hermitian matrices and $V \geq 0$.

To convexify the matrix inequality (5.3.83), we shall give a state-space realization of $S(z) = T_{11}(z) + T_{12}(z)\, Q(z)\, T_{21}(z)$. Denote the state-space representation of $T_{11}(z)$ and $T_{12}(z)T_{21}(z)$ by $(A_{t11},\ B_{t11},\ C_{t11},\ D_{t11})$ and $(A_t,\ B_t,\ C_t,\ D_t)$, respectively. A state-space model of $S(z)$ can be written as (5.1.21)-(5.1.24).

B. Specification (5.3.77)

Similarly, according to the denotation (5.3.79)-(5.3.80), the specification $|S(z)| \geq r$ is equivalent to $\sigma(S, \Pi) \leq 0$ with

$$\Pi = \begin{bmatrix} \Pi_{11} & \Pi_{12} \\ \Pi_{12}^* & \Pi_{22} \end{bmatrix} = \begin{bmatrix} -1 & 0 \\ 0 & r^2 \end{bmatrix}. \tag{5.3.86}$$

However, because $\Pi_{11} < 0$, (5.3.82) can not be converted equivalently to (5.3.83), which means (5.3.82) is not possibly convexified according to the method in Section 5.3.3. Hence, we resort to the following specification

$$\sigma(S, \Pi) = a\mathcal{R}(S) + b\mathcal{I}(S) + c, \quad \Pi := \begin{bmatrix} 0 & a + jb \\ a - jb & 2c \end{bmatrix} \tag{5.3.87}$$

where $\mathcal{R}$ and $\mathcal{I}$ denote the real and the imaginary parts of $S(e^{j\theta})$. When a, b, and c are properly selected, $|S(z)| \geq r$ can be achieved. A simple selection is $a = 0$, $b = -1$, and $c = r$, and

$$\sigma(S, \Pi) = -\mathcal{I}(S) + r. \tag{5.3.88}$$

Thus $\sigma(S, \Pi) \leq 0$ means $\mathcal{I}(S) \geq r$, and subsequently $|S(z)| \geq r$. In this situation,

$$\Pi = \begin{bmatrix} \Pi_{11} & \Pi_{12} \\ \Pi_{12}^* & \Pi_{22} \end{bmatrix} = \begin{bmatrix} 0 & -j \\ j & 2r \end{bmatrix}, \tag{5.3.89}$$

where $\Pi_{11} = 0$ and (5.3.82) is equivalent to

$$\begin{bmatrix} \tilde{A} & \tilde{B} \\ I & 0 \end{bmatrix}^* \Sigma \begin{bmatrix} \tilde{A} & \tilde{B} \\ I & 0 \end{bmatrix} + \begin{bmatrix} 0 & \tilde{C}^* \Pi_{12} \\ \Pi_{12}^* \tilde{C} & \tilde{D}^* \Pi_{12} + \Pi_{12}^* \tilde{D} + \Pi_{22} \end{bmatrix} \leq 0 \tag{5.3.90}$$

which is a linear matrix inequality with unknown variables in $\tilde{C}$ and $\tilde{D}$ only. This can be solved using the same method as in Section 5.3.3 A.

It should be mentioned that $\mathcal{R}(S) \geq r$ can also be used to achieve $|S(z)| \geq r$, if it is suitable for a specific application. In this case,

$$\Pi = \begin{bmatrix} \Pi_{11} & \Pi_{12} \\ \Pi_{12}^* & \Pi_{22} \end{bmatrix} = \begin{bmatrix} 0 & -1 \\ -1 & 2r \end{bmatrix}, \tag{5.3.91}$$

and the linear matrix inequality (5.3.90) remains applicable.

5.3.4 Q Parametrization to Minimize H_2 Performance

Next we focus on the design of $Q(z)$ to minimize the H_2 norm $\|T_{zw}\|_2$. From Figure 5.3 we have

$$-z = N(z)\, w_3 + S(z)\left[P(z)\, D_1(z)\, w_1 + D_2(z)\, w_2 - N(z)\, w_3\right]. \tag{5.3.92}$$

Denote a state-space realization of $P(z)D_1(z)$, $D_2(z)$ and $N(z)$ by (A_1, B_1, C_1, D_1), (A_2, B_2, C_2, D_2), and (A_3, B_3, C_3, D_3), respectively. It follows from (5.1.15) and (5.1.21)-(5.1.24) that

$$x(k+1) = \bar{A}x(k) + \bar{B}w(k), \tag{5.3.93}$$

$$-z(k) = \bar{C}x(k) + \bar{D}w(k), \tag{5.3.94}$$

where,

$$\bar{A} = \begin{bmatrix} A_1 & 0 & 0 & 0 \\ 0 & A_2 & 0 & 0 \\ 0 & 0 & A_3 & 0 \\ \tilde{B}C_1 & \tilde{B}C_2 & -\tilde{B}C_3 & \tilde{A} \end{bmatrix}, \quad \bar{B} = \begin{bmatrix} B_1 & 0 & 0 \\ 0 & B_2 & 0 \\ 0 & 0 & B_3 \\ \tilde{B}D_1 & \tilde{B}D_2 & -\tilde{B}D_3 \end{bmatrix}, \tag{5.3.95}$$
$$\bar{C} = \begin{bmatrix} \tilde{D}C_1 & \tilde{D}C_2 & -\tilde{D}C_3 + C_3 & \tilde{C} \end{bmatrix}, \quad \bar{D} = \begin{bmatrix} \tilde{D}D_1 & \tilde{D}D_2 & -\tilde{D}D_3 + D_3 \end{bmatrix}.$$

The H_2 norm $\|T_{zw}\|_2$ can be minimized as

$$\min_{(\Xi=\Xi^T>0,\ \Omega=\Omega^T>0)} Trace(\Omega), \tag{5.3.96}$$

subject to

$$\bar{A}^T \Xi \bar{A} - \Xi + \bar{C}^T \bar{C} < 0, \tag{5.3.97}$$

$$\bar{B}^T \Xi \bar{B} + \bar{D}^T \bar{D} < \Omega, \tag{5.3.98}$$

or equivalently,

$$\begin{bmatrix} \bar{A}^T \Xi \bar{A} - \Xi & \bar{C}^T \\ \bar{C} & -I \end{bmatrix} < 0, \tag{5.3.99}$$

$$\begin{bmatrix} -\Omega + \bar{B}^T \Xi \bar{B} & \bar{D}^T \\ \bar{D} & -I \end{bmatrix} < 0, \tag{5.3.100}$$

where

$$\begin{aligned}
\bar{A} &= \begin{bmatrix} A_1 & 0 & 0 & 0 & 0 & 0 \\ 0 & A_2 & 0 & 0 & 0 & 0 \\ 0 & 0 & A_3 & 0 & 0 & 0 \\ B_{t11}C_1 & B_{t11}C_2 & -B_{t11}C_3 & A_{t11} & 0 & 0 \\ B_tC_1 & B_tC_2 & -B_tC_3 & 0 & A_t & 0 \\ B_qD_tC_1 & B_qD_tC & -B_qD_tC_3 & 0 & B_qC_t & A_q \end{bmatrix}, \\
\bar{B} &= \begin{bmatrix} B_1 & 0 & 0 \\ 0 & B_2 & 0 \\ 0 & 0 & B_3 \\ B_{t11}D_1 & B_{t11}D_2 & -B_{t11}D_3 \\ B_tD_1 & B_tD_2 & -B_tD_3 \\ B_qD_tD_1 & B_qD_tD_2 & -B_qD_tD_3 \end{bmatrix}, \\
\bar{C} &= \Big[\left(D_{t11} + D_qD_t\right) C_1 \quad \left(D_{t11} + D_qD_t\right) C_2 \\
&\quad \left(D_{t11} + D_qD_t\right) C_3 \quad C_{t11} \quad D_qC_t \quad C_q \Big], \\
\bar{D} &= \Big[\left(D_{t11} + D_qD_t\right) D_1 \quad \left(D_{t11} + D_qD_t\right) D_2 \\
&\quad - \left(D_{t11} + D_qD_t\right) D_3 + D_3 \Big].
\end{aligned} \tag{5.3.101}$$

Note that the $Q(z)$ coefficients $q_i(i = 0, 1, \ldots, \tau)$ only appear in C_q and D_q. Therefore from (5.1.21)-(5.1.24) and (5.3.101), we know that q_i exists only in $\tilde{C}$, $\tilde{D}$, $\bar{C}$, and $\bar{D}$. In this case, (5.3.83), (5.3.90), and (5.3.99)-(5.3.100) define the LMIs in terms of the variables U, V, Ξ, Ω, and q_i. Hence, the $Q(z)$ coefficients q_i can be computed via convex optimization.

With the solved $Q(z)$, the controller $C(z)$ in terms (A_q, B_q, C_q, D_q) is then given by

$$\begin{aligned}
A_c &= \begin{bmatrix} A_p - B_pM + LC_p + B_pD_qC_p & B_pC_q \\ B_qC_p & A_q \end{bmatrix}, \\
B_c &= \begin{bmatrix} L + B_pD_q \\ B_q \end{bmatrix}, \\
C_c &= \begin{bmatrix} -M + D_qC_p & C_q \end{bmatrix}, \\
D_c &= D_q.
\end{aligned} \tag{5.3.102}$$

5.3.5 Design Procedure

The design procedure for controller $C(z)$ in previous section can be summarized as follows.

Step 1. Design $K(z)$ from (5.1.13)-(5.1.14).

Step 2. Compute $T_{11}(z)$, $T_{12}(z)$ and $T_{21}(z)$ from (5.1.16), and obtain the state space model $(\tilde{A}, \tilde{B}, \tilde{C}, \tilde{D})$ in (5.1.21)-(5.1.24).

Step 3. Based on disturbance spectrum and bandwidth requirement, specify the positive scalars r_i and r_j, the frequency points $f_i\,(i = 1, \ldots, m)$, and f_j $(j = 1, \ldots, n)$ for the sensitivity function $S(z)$ such that

$$|S\,(f_i)| < r_i, \quad f_{i1} \leq f_i \leq f_{i2}, \tag{5.3.103}$$

and

$$|S\,(f_j)| > r_j, \quad f_{j1} \leq f_j \leq f_{j2}. \tag{5.3.104}$$

For each specification, construct the LMIs (5.3.83) and (5.3.90) in terms of the variables U, V, C_q, and D_q.

Step 4. Construct the LMIs (5.3.99)-(5.3.100) in terms of the variables Ξ, Ω, C_q, and D_q.

Step 5. Obtain $Q(z) : (A_q, B_q, C_q, D_q)$ by solving the above LMIs using the Matlab LMI toolbox.

Step 6. Obtain the controller $C(z)$ from (5.3.102).

5.4 Experimental Setup and Results

5.4.1 Servo Writing Technologies

Servo track writer (STW) is the process of writing servo patterns on magnetic disks. Position detection circuit in HDDs reads the servo patterns and demodulates the PES for HDD servo controller. As the track density of HDD is achieving $300,000$ TPI and keeps increasing toward the target of areal density 10 Tb/in^2, it is essential to improve the tracking performance of STW to support writing of qualified servo patterns at such a high track density. One of the major factors is the written-in RRO, which directly affects linear characteristics of the PES transfer curve and therefore the PES sensing noise [74] [75].

In STW technologies there are conventional STW (CSTW) [76], self STW (SSTW) [77] and media level STW (MLSTW) [78]. In both CSTW and MLSTW, the feedback servo loop is constructed on the arm position measured by an optical sensor. As such, the vibrations induced from disk, spindle, suspension, and slider are directly coupled into written-in RRO [79]. In SSTW, the servo system is closed with the feedback of PES, thus it includes all the system vibrations into the servo loop. In general, this configuration allows servo engineers to design optimal controller based on advanced loop shaping technology [19]. The authors in paper [80] discussed control strategies in STW for high TPI and proposed the idea of hybrid dual-stage servo for STW (HSSTW).

5.4.2 STW Experimental Platform with Hybrid Dual-stage Servo

Figure 5.4 shows the STW experimental platform with two disk platters. It is composed of MicroE optical positioning system, a specially designed arm with a PZT actuator embedded in between the arm and suspension, a fluid bearing spindle, load/unload ramp mechanism, and linear stages for regulation of z-height and skew angles of data heads and clock head. A balancing clamp was designed for the spindle to balance the disk-spindle pack [81]. The setup was placed on a vibration isolation table under clean-hood.

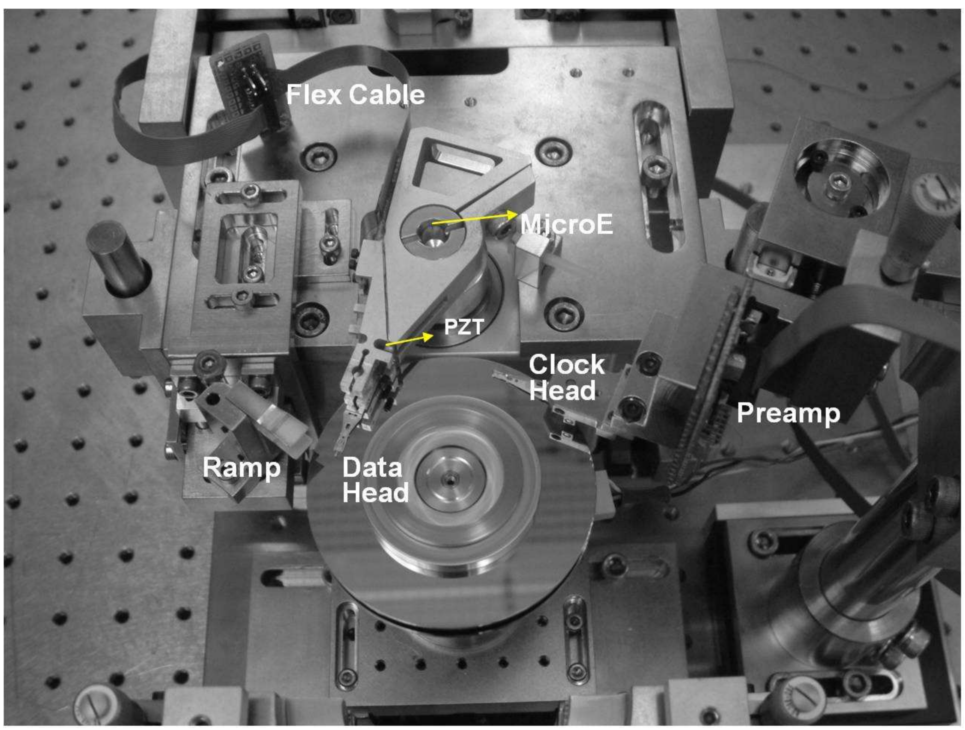

Figure 5.4: Dual stage STW experimental platform.

The disk platters used are of 2.5 inch in diameter, 1.33 mm thickness, made from glass substrate. The spindle speed is 5400 RPM, and the number of servo sectors in one revolution is 501.

5.4.3 System Functions of STW Platform

STW needs two essential functions to write well-aligned servo patterns on blank disk (1) The circumferential angular position of R/W head needs to be known precisely; (2) Ability to position R/W head in a radial direction accurately.

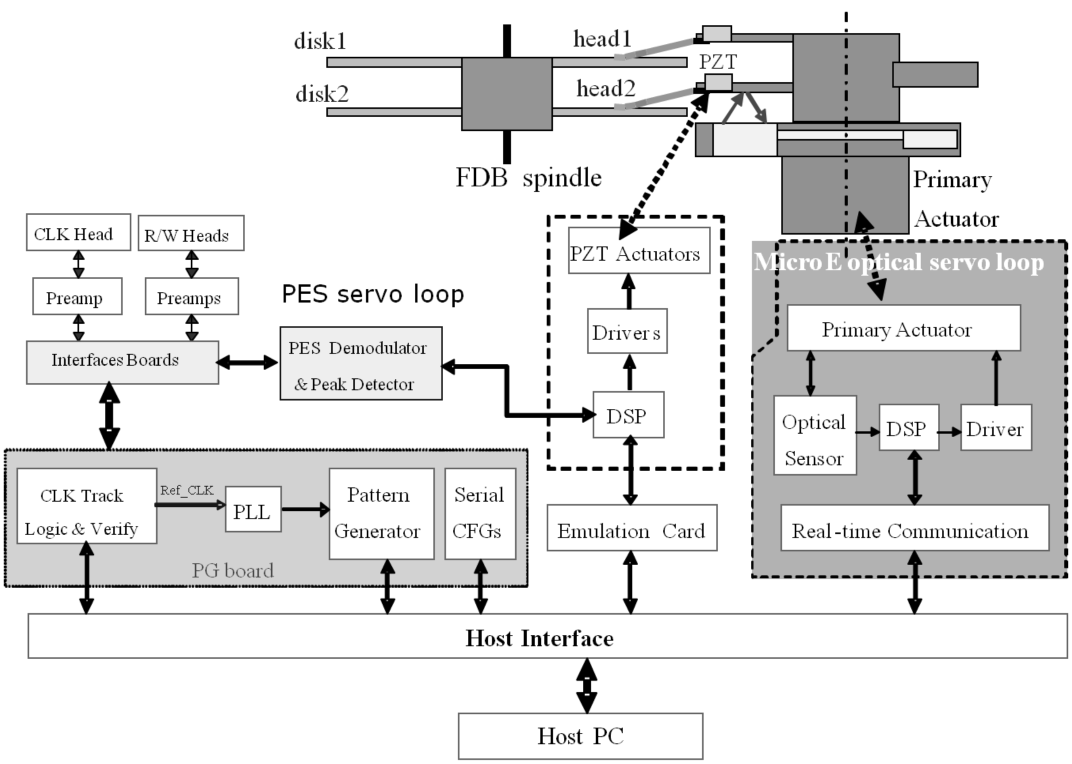

Figure 5.5: Functional block diagram of the HSSTW platform.

Figure 5.5 shows the functional block diagram of the experimental platform to support the above two essential functions. The first function is achieved by clock head together with phase-locked loop (PLL). A special sequence of clock timing mark (clock track) can be written at outer diameter and read back by clock head. All the servo patterns are generated synchronously aligned with clock track using

PLL. The clock tracks work as reference to tell the circumferential angular position, and the PLL is used to track the variations of spindle rotational speed.

In Figure 5.5, there are two servo loops to control the radial position of data head. MicroE optical positioning servo system controls the radial position of arm, while the PES servo loop with PZT actuator is used to control the position of data head more accurately. This will be discussed in details in the next section.

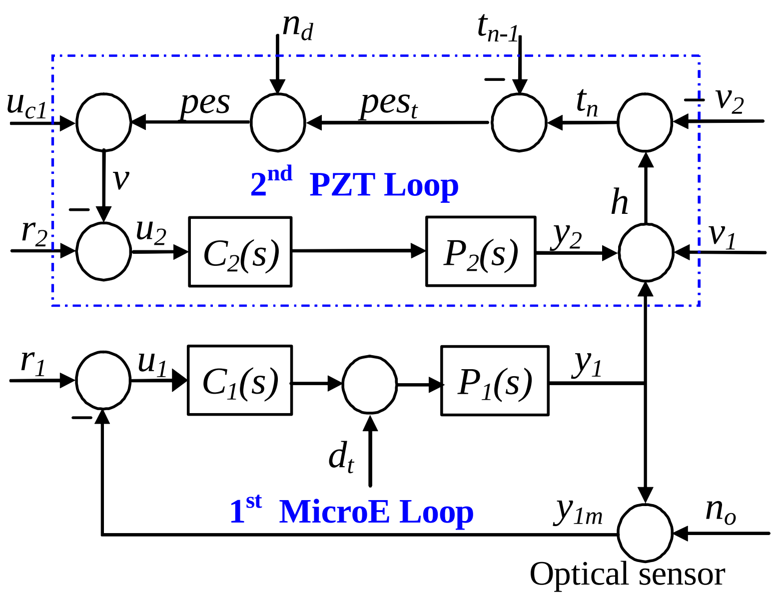

Figure 5.6: Hybrid dual-stage servo system.

5.4.4 Servo Mechanism of STW Platform

Figure 5.6 shows the block diagram of the hybrid dual-stage servo system ("hybrid" means the mixture of optical positioning and PES servo loop). In Figure 5.6, $P_1(s)$, $C_1(s)$, $P_2(s)$, and $C_2(s)$ are plants and controllers for MicroE actuator and PZT micro-actuator, respectively. y_1 is the position of the actuator arm, y_2 is the displacement of PZT, r_1 and r_2 are references for optical positioning, and PES servo loop, respectively. h is the position of R/W head, v_1 includes vibrations of suspension, slider, and head, v_2 includes vibrations of spindle and disk, and d_t is the torque disturbance due to air flow and external vibrations. t_n and t_{n-1} are the positions of the current and the previous servo track, respectively, and n_0 and n_d are the measurement noises of optical sensor and PES demodulator,respectively.

In perfect servo writing, t_{n-1} is expected to be zero, or written-in RRO will cause AC/DC squeeze [79]. It can be measured by synchronous averaging [47] of *pes* while positioning read head on $(n-1)^{th}$ track with only MicroE optical servo loop, i.e., PZT servo loop is off.

If a compensation signal $u_{c1} = t_{n-1}$ is injected, then

$$\begin{aligned} t_n &= h - v_2 \\ &= T_2(s)(r_2 - n_d) + S_2(s)(v_1 - v_2) + \\ &\quad S_2(s)T_1(s)(r_1 - n_0) + S_2(s)S_1(s)P_1(s)d_t, \end{aligned} \tag{5.4.105}$$

where $T_1(s)$ $S_1(s)$ and $T_2(s)$ $S_2(s)$ are the complementary sensitivity functions and sensitivity functions for the optical servo loop and the second servo loop respectively. In this configuration, the optical servo loop roughly moves the R/W head to the desired track, then enables the second loop to precisely control the head with reference to the previous ideal track , by decoupling the previous written-in error t_{n-1} from *pes* for writing current servo track.

(5.4.105) shows that no previous written-in error t_{n-1} is coupled into t_n, which means that there is no error propagation problem as that in SSTW [82]. Also note that the written-in errors due to $(v_1 - v_2)$, n_o, and d_t are all filtered by $S_2(s)$. Therefore, the written-in error induced from these vibrations will be reduced significantly using advanced loop shaping technologies such as in [19] [83].

The feedback signals for optical loop and PES loop are from independent sensors. As such, the two servo loops are completely decoupled. The measurement noise and torque disturbance in optical servo loop can be looked as a lumped output disturbance to the PZT servo loop. The performance of the MicroE optical positioning system is limited by the dynamic performance of the actuator, and its control firmware has very little flexibility to shape the loop transfer function. In this section, we focus on the controller design for the PZT micro-actuator loop.

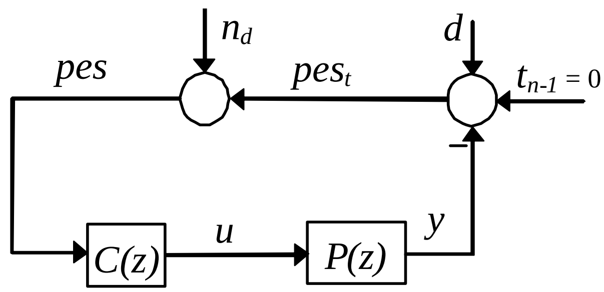

Figure 5.7: Equivalent PZT servo loop.

5.4.5 Measurement and Modeling of Vibrations and Noises

As discussed previously, the PES servo loop with PZT actuator is independent. Its equivalent discretized model is shown in Figure 5.7, where $d(t)$ is the lumped output disturbances. We measure the spectrum of non-repeatable runout(NRRO) of PES and decompose the spectrum model of $d(t)$ and $n_d(t)$ [47].

Figure 5.8 shows the spectrum of PES NRRO, where the low frequency modes (1, 2, 3) are due to the environmental vibrations such as vibrations of motors on clean-hood and ionizer, and air flow induced torque disturbance. The modes (4, 5, 6, 7) at the middle frequencies are caused by disk vibrations, and the other modes (8, 9) are suspension torsion and sway modes. These modes can be approximately modeled as $d = D(s) \times \omega$ with a white noise ω (σ=1) and

$$D(s) = 0.00163 \times \quad \frac{s^2 - 2.69s + 5.26e5}{s^2 + 0.75s + 3.95e5} \times \frac{s^2 - 585.6s + 3.76e6}{s^2 + 0.20s + 1.01e6} \times \frac{s^2 + 4161s + 2.0e7}{s^2 + 245s + 1.67e7} \times \frac{s^2 + 2402s + 5.63e8}{s^2 + 477s + 5.7e8}. \quad (5.4.106)$$

The straight baseline is generally due to the PES demodulation noise $n_d(t)$ ($\sigma = 5$

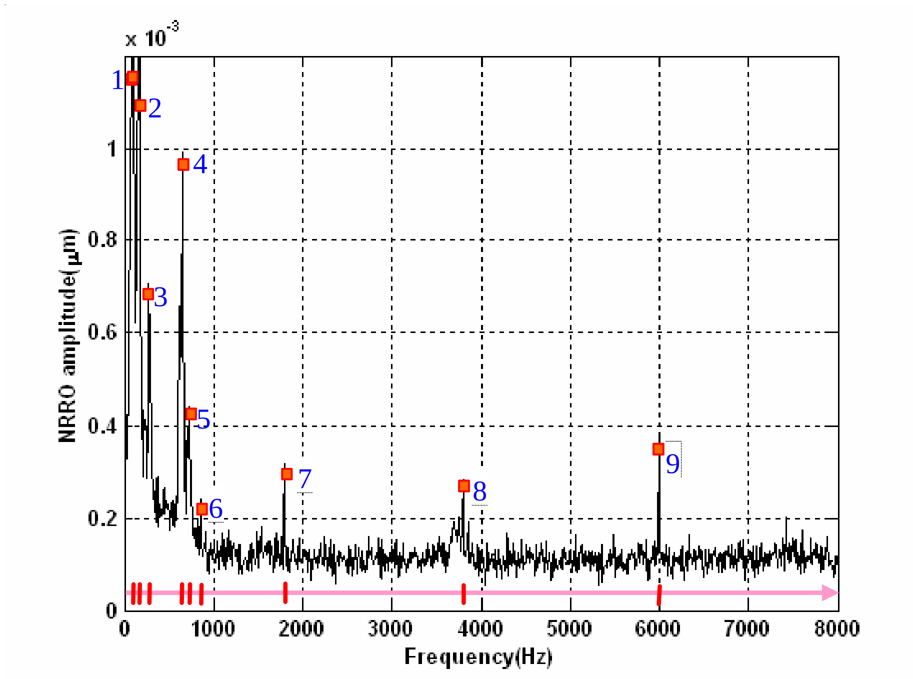

Figure 5.8: Spectrum of PES NRRO without the second loop.

nm). It can be assumed to be white.

The PES demodulation noise is caused by media noise, head noise, and electronic noise in demodulation circuits such as A/D converter. We can experimentally verify its spectrum model.

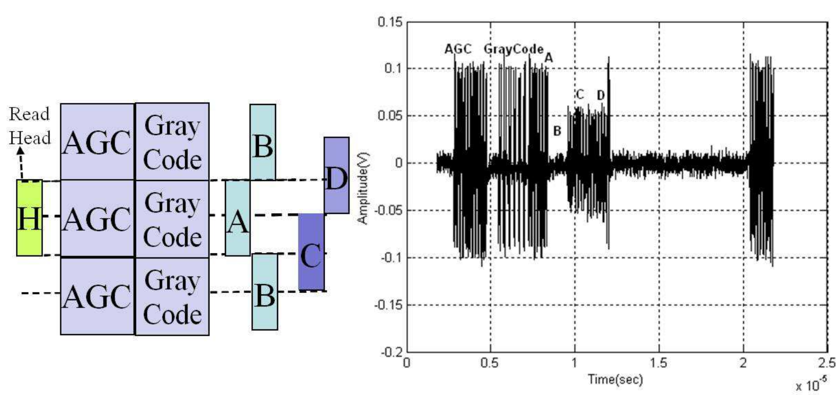

Figure 5.9: The format of servo bursts and typical servo pattern readback signal.

Figure 5.9 shows the conventional quadric servo bursts and the corresponding read back signal when position R/W head (block 'H') exactly over A servo bursts. The PES demodulated from the relative amplitude difference between A and B or C and D bursts tells the R/W head's off-track position. We can write a special servo pattern, which is the same as conventional one, but without A, B, C, and D servo bursts. Because the PES demodulation circuit still works well while the R/W head's off-track position is not sensed in PES, PES is all contributed by sensing noise. As such, its NRRO spectrum is exactly the spectrum of demodulation noise as shown in Figure 5.10 which has the same level as the straight baseline in Figure 5.8.

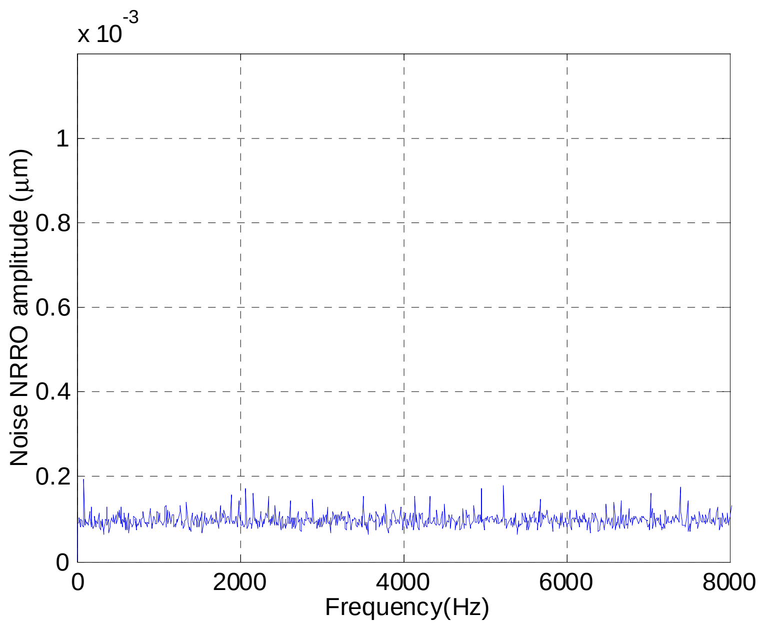

Figure 5.10: Spectrum of PES demodulation noise.

Suppose that $PES(k)$, $PES_t(k)$, $D(k)$, and $N_d(k)$ are the discrete Fourier transform results of pes, pes_t, d, and n_d, respectively. From Figure 5.7, we have

$$\begin{aligned} PES_t(k) &= S(k)D(k) - T(k)N_d(k), \\ S(k) &= \frac{1}{1+P(k)C(k)}, \\ T(k) &= \frac{P(k)S(k)}{1+P(k)C(k)}, \end{aligned} \tag{5.4.107}$$

where $S(k)$ is the sensitivity function of the servo loop, and $T(k)$ is the complementary sensitivity function. Usually, $D(k)$ and $N_d(k)$ are uncorrelated in practice, and the expected value of the spectral intensity $|PES_t(k)|^2$ is

$$E\{|PES_t(k)|^2\} = |S(k)|^2 E\{|D(k)|^2\} + |T(k)|^2 E\{|N_d(k)|^2\}.$$

As the mean value of pes_t is zero for a closed-loop servo with bias compensation, the expected variance of pes_t is [84],

$$\begin{aligned} \sigma^2_{pes_t} &\equiv E\{pes_t(n)^2\} = \frac{1}{N^2}\sum_{k=0}^{N-1} E\{|PES_t(k)|^2\} \\ &= \frac{1}{N^2}\sum_{k=0}^{N-1} |S(k)|^2 E\{|D(k)|^2\} + \frac{N_{d0}^2}{N}\sum_{k=0}^{N-1}|T(k)|^2, \end{aligned} \tag{5.4.108}$$

where N_{d0} is the RMS value of demodulation noise and N is number of samples which is sufficiently large.

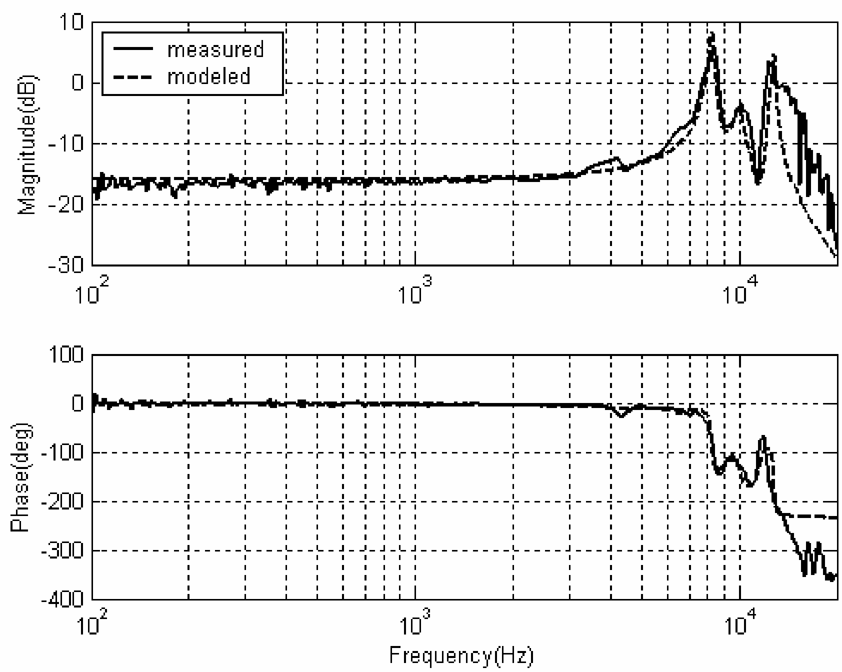

Figure 5.11: Frequency response for piezo chip.

(5.4.108) directly links the servo characteristic (sensitivity and complementary sensitivity function) and spectrum characteristics of disturbances and sensing noise with the tracking performance of servo system. It clearly shows that increasing bandwidth can reduce the RMS of pes_t induced from disturbances, but will enlarge the contributions from demodulation noise. Therefore, there exists an optimal servo bandwidth.

Figure 5.11 shows the modeled and the measured frequency responses of the PZT actuator. With the known plant model, we can use H_∞ loop shaping method to design series of controllers with different bandwidths and calculate the RMS of pes_t according to (5.4.108) with the known disturbances and noise models. As shown in Table 5.1, the optimal bandwidth (the 0 dB crossover frequency of open-loop transfer function) is around 885 Hz.

Table 5.1: Tracking accuracy for different servo bandwidth.

Open-loop Bandwidth (Hz)	$3\sigma_{pes_t}$ (nm)
360	8.6
770	7.6
885	7.1
1060	8.6
1160	9.7

5.4.6 Experimental Verification of the Controller Performance for PZT Loop

In (5.4.108), the RMS value of $|S(k)|$ cannot be made arbitrarily small by increasing the bandwidth as it is limited by Bode's integral theorem [85]. Disturbance observers [86] [87] can be designed for attenuating external vibrations at low frequencies. An appropriate controller design is required to shape the sensitivity function to have a sufficient attenuation for disturbances with known frequency ranges.

For comparison, we designed $C(z)$ using the following three methods: (1) phase-lead peak filter (PLPF) [88]; (2) generalized KYP lemma; (3) KYP lemma combined with H_2. The PLPF was applied to concern more on the attenuation of the significant fourth-mode of disturbance, while the KYP lemma was applied for better attenuation of those major disturbances distributed from 100 Hz to 1000 Hz in Figure 5.8. All three controllers were implemented on the STW experimental platform.

For the frequency responses of the microactuator shown in Figure 5.11, six resonant modes at 3.7, 4.9, 6.9, 9, 12.7, and 15 kHz are included in the model.

The disturbance distribution is reflected in the non-repeatable runout power spectrum of the measured PES in Figure 5.8. It is noticed that there is a vibration mode at 650 Hz due to disk vibration. The objective here is to use the above KYP method to design a linear dynamic output feedback controller $C(z)$ for the microactuator in Figure 5.6, such that its closed-loop system is stable and the disturbance centering at 650 Hz is suppressed sufficiently. A 45 kHz sampling rate is used in the servo control design. The control algorithm is implemented with the digital position error signal generated from DSP TMS320C6711. Currently due to the limitation by the DSP speed, the platform can support to implement a controller up to 10^{th} order .

Because 650 Hz is at a relative low frequency range, we involve the static part of the microactuator represented by a pade delay in the control design with the KYP lemma. After that, notch filters for the resonant modes at 3.7, 9, and 15 kHz will be used to compensate the dynamic part, which will not significantly change the obtained performance of the low frequency part. The 4.9 and 6.9 kHz resonant modes, seen in Figure 5.11, have relatively small magnitudes and can be ignored as long as they are not excited in the control loop. The resonant mode at 12.7 kHz is not considered in the control design as it is not excited easily and does not affect the whole loop stability when the 15 kHz mode is compensated.

The pade delay model is given by

$$P_{pade-delay} = -5.6234 \frac{s - 2 \cdot \pi \cdot 17000}{s + 2 \cdot \pi \cdot 17000}, \tag{5.4.109}$$

which is pre-compensated by the proportional-integral (PI) controller

$$Int(z) = 0.027(-\frac{z}{z-0.999} + 0.5). \qquad (5.4.110)$$

The desired specifications for the sensitivity function $S(z)$ are set as:

$$\begin{aligned} &Spec.(a) \quad |S(f)| < 0\ dB,\ f \leq 500\ Hz, \\ &Spec.(b) \quad |S(f)| < -10\ dB,\ 610\ Hz \leq f \leq 670\ Hz, \\ &Spec.(c) \quad |S(f)| < 9.54\ dB,\ f \geq 19\ kHz. \end{aligned}$$

Spec. (b) means to attenuate the disturbances centering at 650 Hz by 10 dB at least. The parameters of $Q(z)$ in (5.1.25) with $\tau = 1$ are attained by solving three LMIs of the form (5.1.9) corresponding to Spec. (a), (b) and (c). The resultant $C(z)$ is a 10^{th} order controller.

The phase-lead peak filter (PLPF) of the form in [88] with values $K = 0.4$, $\phi = -0.584$, $\omega_0 = 2\pi \times 650$, and $\xi = 0.0632$, is also applied to suppress the low frequency disturbances around 650 Hz. The comparison of the sensitivity functions is shown in Figure 5.12. It can be seen that the KYP method achieves better disturbance rejection from 60 Hz to 1 kHz, although they have almost the same rejection capability in the very narrow band around 650 Hz. However, the KYP method gives a poorer disturbance rejection performance for frequency below 60 Hz than the PLPF method.

In the comparison of open loop frequency response in Figure 5.13, the phase margin (PM) with the PLPF method is higher, while the bandwidth is lower. The gain margin (GM) is comparable with the KYP lemma method. Consistent with the sensitivity functions in Figure 5.12, the PES NRRO power spectrum comparison is shown in Figure 5.14 which clearly shows that the KYP lemma-based design gives a better disturbance rejection around 650 Hz than the PLPF although at 650 Hz they offer a similar performance.

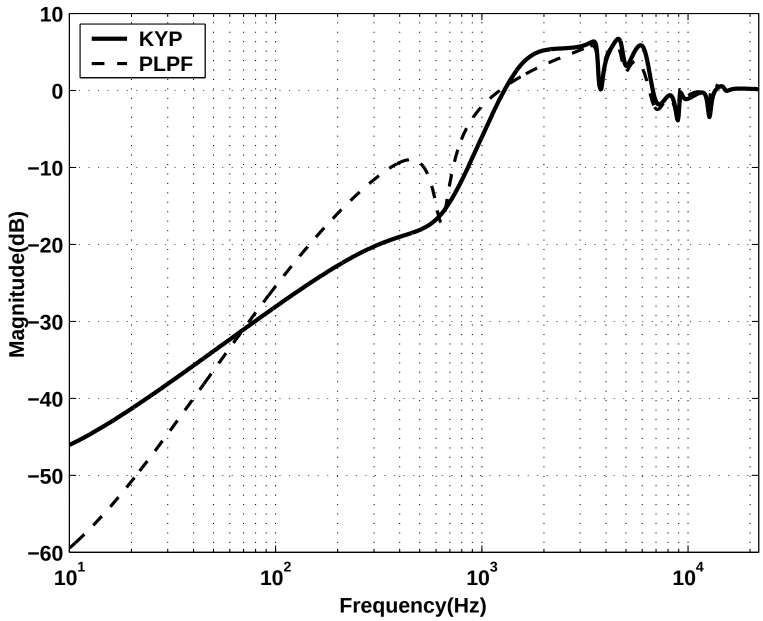

Figure 5.12: Sensitivity function simulated. (solid: KYP; dashed: PLPF).

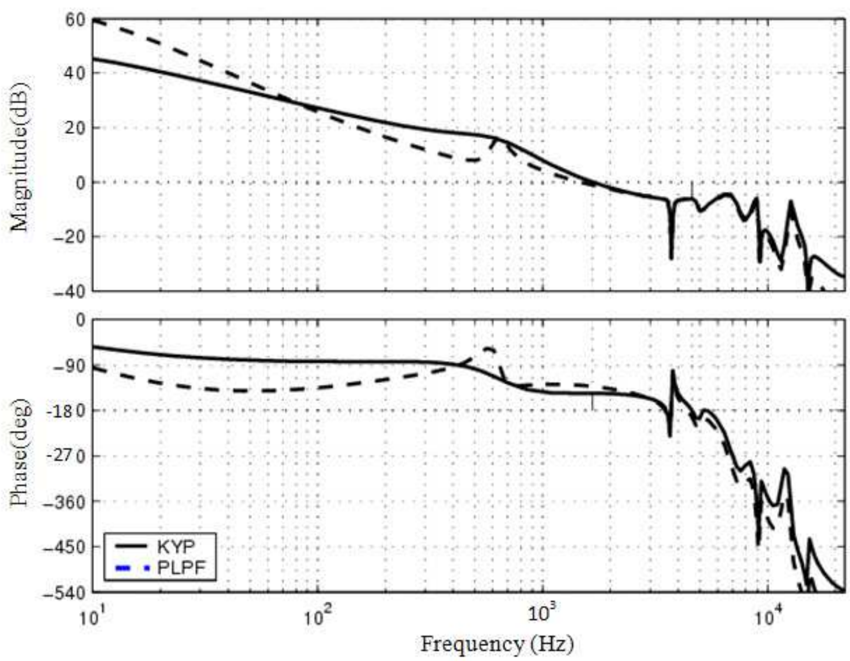

Figure 5.13: Open loop frequency response. (solid: KYP; dashed: PLPF).

From Figure 2.16, it is known that the spectrum of the true PES, y, is given by

$$\mathcal{S}_y = |P(z)S(z)|^2 \times |d_1|^2 + |S(z)|^2|d_2|^2 + |T(z)|^2 \times |n|^2 \quad (5.4.111)$$
$$= \mathcal{S}_e - |S(z)|^2 \times |n|^2 + |T(z)|^2 \times |n|^2, \quad (5.4.112)$$

where $\mathcal{S}_e$ is in (5.1.1), and $T(z) = 1 - S(z)$ is the closed-loop transfer function. As such, the 3σ value of the true PES can be assessed from the power spectrum $\mathcal{S}_e$ in Figure 5.14 with the known level of noise n. As a result, it is improved from 6.4 nm with the PLPF method to 6 nm with the KYP lemma method.

In the above design, only the first order $Q(z)$ is used. A higher order $Q(z)$ offers more design freedom and has the potential of achieving better results. However, the resultant sensitivity function has to comply with the Bode integral theorem for whatever $Q(z)$ is used, meaning that it is not possible to achieve disturbance rejection across the entire frequency range.

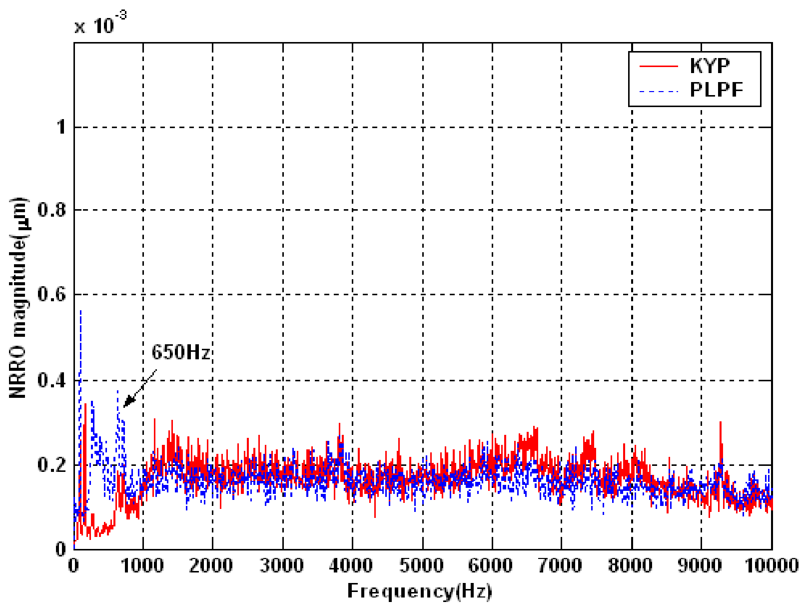

Figure 5.14: Spectra of PES NRRO with the secondary loop (solid: KYP; dashed: PLPF).

With considerations of both the disturbances in Figure 5.8 and minimization the position error signal, a suitable feedback controller, $C(z)$ has to be designed for the system so that the overall system is stable and the disturbance around 650 Hz is suppressed sufficiently, while ensuring that the H_2 norm of the position error signal is minimized. Hence, the desired specification of the sensitivity function $S(z)$ is $|S(f)| < -10$ dB for 610 Hz $\leq f \leq$ 670 Hz. The position error signal is to be minimized at the same time.

The parameters of a first-order FIR $Q(z)$ are obtained by solving the three LMIs (5.3.83), (5.3.99), and (5.3.100) with consideration of both H_2 minimization and suppression of the vibration around 650 Hz. The frequency response of the open-loop $C(z)P(z)$ and the sensitivity function $S(z)$ are depicted in Figure 5.15 and Fig. 5.16. It is seen that the hump of $S(z)$ is reduced to about 3 dB with the controller designed by the combined method, i.e., the combined H_2 optimization and specific disturbance rejection method. On the other hand, Figure 5.15 shows that the proposed combined method offers better stability margins although the open-loop crossover frequency is a bit lower.

Comparing the sensitivity functions in Figure 5.16 and Figure 5.17, the experimental results matched well with the simulation results. It also shows that the sensitivity function resulted from KYP+H_2 has lower hump than the one from KYP only from 2 to 4 kHz. This is also verified in the PES spectrum shown in Figure 5.18.

The performances for different controllers are summarized in Table 5.2. With the combined control design method using KYP and H_2, the servo loop can attenuate specific narrow band disturbances and minimize the tracking error as well.

Table 5.2: Performance with different controllers for PZT loop.

Design Method	$3\sigma_{pes_t}$ (nm)	Gain Margin (dB)	Phase Margin (deg)	Bandwidth (Hz)
No PZT loop	15.1	nil	nil	nil
PLPF	6.4	6	50	1400
KYP	6.0	7.9	36	1700
KYP+H_2	5.6	12.6	45.9	1560

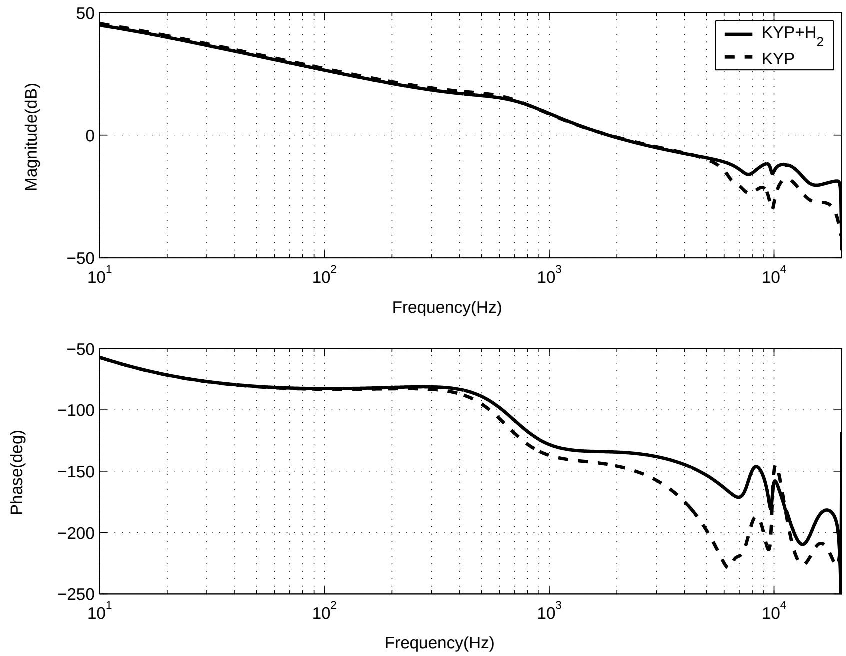

Figure 5.15: Frequency response of open-loop transfer functions. (solid: KYP+H_2; dashed: KYP).

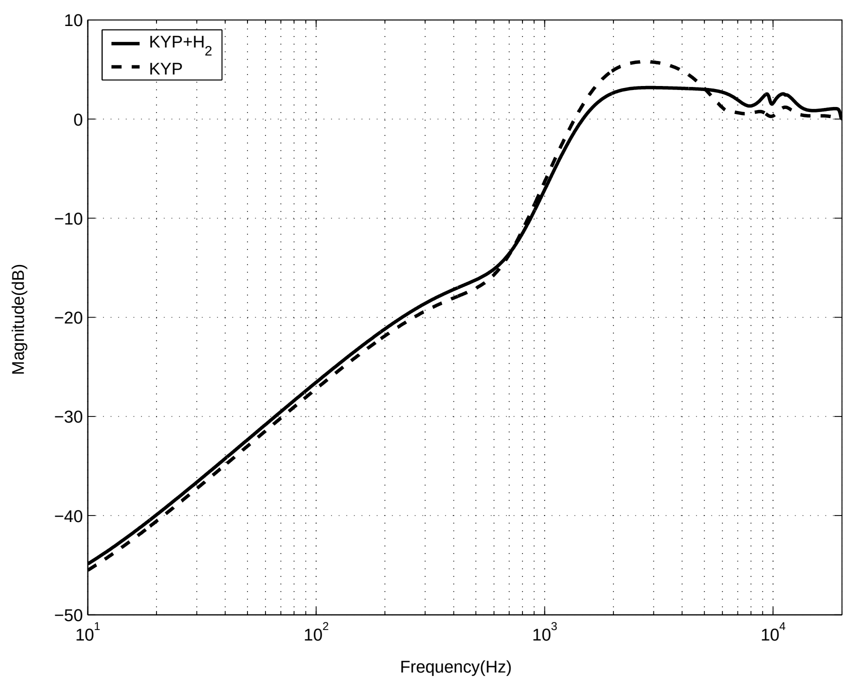

Figure 5.16: Simulations of sensitivity function. (solid: KYP+H_2; dashed: KYP).

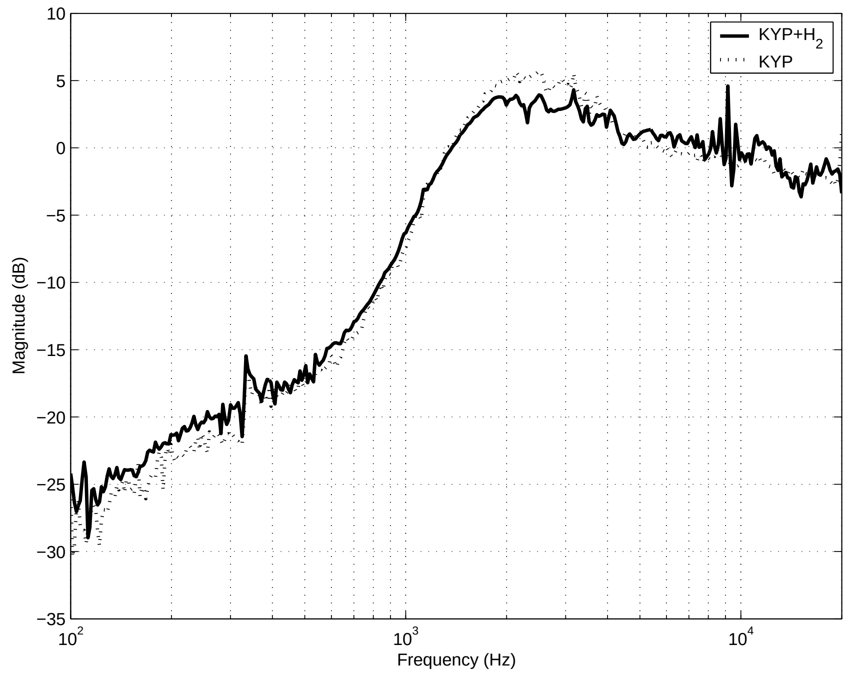

Figure 5.17: Sensitivity functions measured. (solid: KYP+H_2; dashed: KYP).

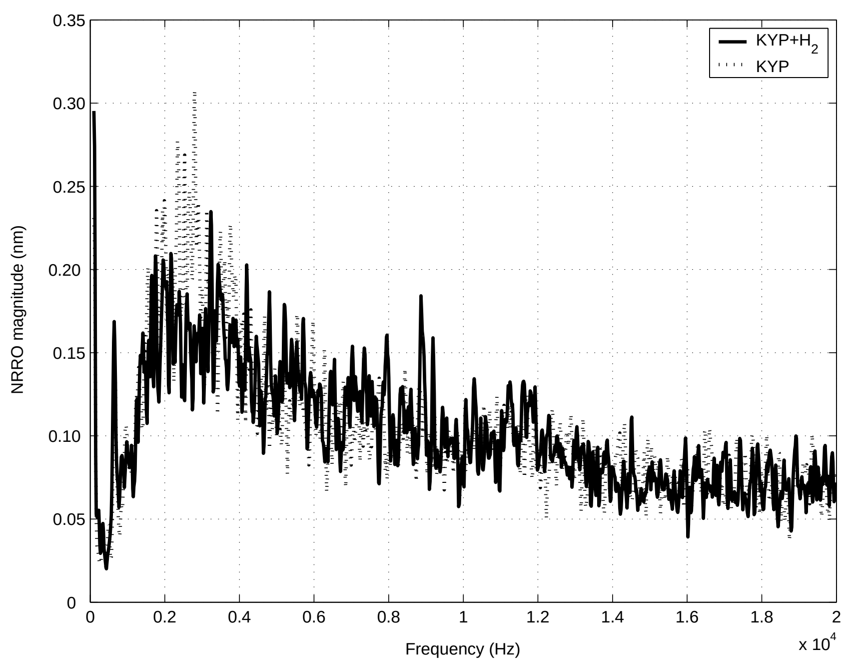

Figure 5.18: Spectra of PES NRRO with the secondary loop (solid: KYP+H_2; dashed: KYP).

Chapter 6

Conclusions and Future Work

6.1 Summary of Results

This dissertation gives a full picture of the servo control issues in HDDs which includes seeking, tracking, and settling. Meanwhile, it addresses some important issues regarding to the HDDs in consumer electronics applications, such as acoustic noise problem and residual vibrations problem in seeking, smooth settling problem in dual-stage servo control, and tracking accuracy problem in the existence of significant vibrations.

To reduce the seeking noise for HDDs in consumer electronics applications, we proposed a smooth pseudo-sinusoidal seek current profile for arbitrary seek length with minimum jerk in acceleration. A systematic method with a set of design parameters for the current profile is proposed to minimize the residual vibrations caused by the most significant resonant mode. The simulation results have shown the advantage and performance improvement of the proposed method over conventional PTOS method with respect to both the seek time and residual vibrations.

This dissertation presents an effective and easily implemented settling scheme, namely IES, to achieve fast and smooth track settling for dual-stage servo system. In this settling scheme, a feedforward compensator is used to cancel the error caused by the initial position and velocity of VCM actuator during mode-switching. Based on ZPET, a detailed pole/zero cancelation scheme is used in the design of the feedforward compensator. The experiment results show that settling time can be significantly reduced from 0.7 ms to 0.3 ms.

The dissertation also presents an advanced systematic loop shaping method using KYP Lemma to optimize the track-following controller with considerations of the spectrum models of torque disturbances, output disturbances and sensing noise. The Youla parametrization approach is first used to parameterize the closed-loop transfer function. The search for the coefficients of the parameter $Q(z)$ is then converted to a linear matrix inequality problem within the generalized KYP lemma framework. Next, considering the system with an augmented disturbance model, the generalized KYP lemma is combined the H_2 method to design a controller for minimization of tracking error as well as attenuation of dominant disturbances at certain frequencies. We applied this method to design a track-following controller and implemented it on our STW experiment platform. The performances for controllers using different design method are summarized in Table 6.1. With the combined control design method using KYP and H_2, the servo loop can achieve better tracking accuracy and provide better robustness with more gain margin and phase margin than the other methods. As such, we achieved servo-writing track density of $420,000$ TPI on the STW experiment platform.

Table 6.1: Performance of servo controllers using different design method.

Design Method	$3\sigma_{pes_t}$ (nm)	Gain Margin (dB)	Phase Margin (deg)	Bandwidth (Hz)
PLPF	6.4	6	50	1400
KYP	6.0	7.9	36	1700
KYP+H_2	5.6	12.6	45.9	1560

6.2 Future Work

For the smooth seeking using pseudo-sinusoidal current profile, we know that jerk in acceleration causes seeking noise from practical experience. The relationship between them is not rigorously proved. As such, the determination of the value for the frequency of sine wave in current profile is based on trial and error. Furthermore, the design parameters for current profile can be selected only to minimize the residual vibration induced from one of the most significant mode. In future, this method can be extend to reduce residual vibrations caused by multi-modes.

For the IES settling scheme for dual-stage servo systems, the feedforward compensator is designed for any initial position and velocity of VCM actuator as long as the micro-actuator is not saturated. In experimental implementation, we notice that the settling performance is different at different switching conditions. In future, it is valuable to study the optimal switching conditions for this settling scheme as we can chose when to switch from seeking mode to tracking mode in practice.

To achieve positioning accuracy of less than a few nanometers for future HDDs with areal density of multi-Tb/in^2, the servo mechanism in HDDs will integrate with different type of sensors to detect vibrations, such as PZT sensor for detecting suspension vibrations [83], strain-type sensors for detecting butterfly mode of VCM actuator [89], and accelerometers for detecting external rotational vibrations [10]. As such, the whole servo system becomes a complicated multi-sensing dual-stage servo system consisting of several components such as suspensions, sensors and actuators. For such a complicated system, the optimal control will not only take into account the dynamics of actuators and vibrations, it also need to take into account the dynamics of sensors. The combined design method using KYP and H_2 should be extended to solve a more complicated synthesis problem including the dynamics of sensors.

Author's Publications

1. J. L. Zhang, F. Hong, S. S. Ge, "The strategy of designing seek current profile to reduce acoustic noise and residual vibrations," *IEEE Transactions on Magnetics*, vol. 46, no. 6, pp. 1319-1323, 2010.

2. J. L. Zhang, C. L. Du, S. J. Jiang, "Measurement and modeling of disturbances in a servo track writer and advanced loop shaping to achieve higher track density ," *Transactions of the Institute of Measurement and Control*, vol. 32, no. 2, pp. 221-224, April, 2010.

3. J. L. Zhang, B. Hredzak, C. L. Du, G. Guo, "High density servo track writing using two-stage configuration," in *Proceedings of IEEE International Conference on Control Applications*, Singapore, pp. 124-129, 2007.

4. J. L. Zhang, F. Hong, S. S. Ge, "A novel settling controller for Dual-Stage servo systems ," *IEEE Transactions on Magnetics*, vol. 44, no. 11, pp. 3757-3760 , 2008.

5. B. Hredzak, F. Hong, S. S. Ge, J. L. Zhang and Z. M. He, "Modeling and compensation of pivot nonlinearity in hard disk drives," in *Proceedings of IEEE International Conference on Control Applications*, Singapore, pp. 108-113, 2007.

6. C. L. Du, L. H. Xie, J. L. Zhang, G. Guo, "Disturbance rejection for a data storage system via sensitivity loop shaping and adaptive nonlinear compensation," *IEEE/ASME Transactions on Mechatronics*, vol. 13, pp. 493-501,

2008.

7. C. L. Du, L. H. Xie, G. Guo, J. L. Zhang, Q. Li, "A generalized KYP lemma based control design and application for 425 kTPI servo track writing," in *Proceedings of the American Control Conference*, Minneapolis, Minnesota, pp. 1303-1308, 2006.

8. C. L. Du, L. H. Xie, J. L. Zhang, "Compensation of VCM actuator pivot friction based on an operator modeling method," *IEEE Transactions on Control Systems Technology*, vol. 18, pp. 918-926, 2010.

Bibliography

[1] W. C. Blount, "Fluid dynamic bearing spindle motors: Their future in hard disk drives," *http://www.hitachigst.com*, 2007.

[2] R. W. Wood, J. Miles, and T. Olson, "Recording technologies for Terabit per square inch systems," *IEEE Transactions on Magnetics*, vol. 38, no. 4, pp. 1711–1718, 2002.

[3] T. Yamaguchi and T. Atsumi, "HDD servo control technologies- what we have done and where we should go," in *Proceedings of the 17th World Congress, The International Federation of Automatic Control*, Coex, Korea, 2008, pp. 821–826.

[4] W. Messner and R. Ehrlich, "A tutorial on controls for disk drives," in *Proceedings of the American Control Conference*, Arlington, VA, 2001, pp. 408–420.

[5] J. Hoagg and D. Bernstein, "Nonminimum-phase zeros: Much to do about nothing," *IEEE Transactions on Control Systems*, vol. 27, pp. 45–57, 2007.

[6] C. Mohtadi and M. DPhil, "Bode's integral theorem for discrete-time systems," *IEE Proceedings, Control Theory and Applications*, vol. 137, no. 2, pp. 57–66, 1990.

[7] D. Abramovitch, T. Hurst, and D. Henze, "The PES pareto method: uncovering the strata of position error signals in disk drives," in *Proceedings of the American Control Conference*, Albuquerque, NM, June 1997, pp. 2888–2895.

[8] S. Baek and S. Lee, “Vibration rejection control for disk drives by acceleration feedforward control,” in *Proceedings of the IEEE Conference on Decision and Control*, Phoenix, AZ, 1999, pp. 5259–5262.

[9] J. Ishikawa and M. Tomizuka, “Pivot friction compensation using an accelerometer and a disturbance observer for hard disk drives,” *IEEE/ASME Transactions on Mechatronics*, vol. 3, no. 3, pp. 194–201, 1998.

[10] A. Jinzenji, T. Sasamoto, K. Aikawa, S. Yoshida, and K. Aruga, “Acceleration feedforward control against rotational disturbance in hard disk drives,” *IEEE Transactions on Magnetics*, vol. 37, no. 2, pp. 888–893, 2001.

[11] M. Kobayashi, T. Yamaguchi, T. Yoshida, and H. Hirai, “Multi-sensing servo with carriage-acceleration feedback for magnetic disk drives,” in *Proceedings of the IEEE Conference Decision and Control*, Philadelphia, PA, 1998, pp. 3038–3042.

[12] H. S. Chang, S. E. Baek, J. H. Park, and Y. K. Byun, “Modeling of pivot friction using relay function and estimation of its frictional parameters,” in *Proceedings of the American Control Conference*, San Diego, CA, 1999, pp. 3784–3789.

[13] M. K. Ciliz and M. Tomizuka, “Modeling and compensation of frictional uncertainties in motion control: a neural network based approach,” in *Proceedings of the American Control Conference*, Seattle, WA, 1995, pp. 3269–3273.

[14] S. S. Ge, T. H. Lee, and S. X. Ren, “Adaptive friction compensation of servo mechanisms,” *International Journal of Systems Science*, vol. 32, no. 4, pp. 523–532, 2001.

[15] G. Zames, “Feedback and optimal sensitivity: Model reference tranformations, multiplicative seminorms, and spproximate inverses,” *IEEE Transactions Automatic Control*, vol. 26, no. 2, pp. 301–320, 1981.

[16] B. Francies, *A Course in H_∞ Control Theory.* Springer-Verlag, Berlin: Lecture Notes in Control and Information Science 88, 1987.

[17] B. M. Chen, Z. L. Lin, and K. X. Liu, "Robust and perfect tracking of discrete time systems," in *Proceedings of the American Control Conference*, Arlington, VA, 2001, pp. 2594–2599.

[18] G. Cheng, K. Peng, B. M. Chen, and T. H. Lee, "A microdrive track following controller design using robust and perfect tracking control with nonlinear compensation," *Mechatronics*, vol. 15, no. 8, pp. 933–948, 2005.

[19] C. Du, L. Xie, J. N. Teoh, and G. Guo, "H_2 control for head positioning in axial and radial dimensions for self-servo track writing," *IEEE Transactions on Control Systems Technology*, vol. 16, no. 1, pp. 177–181, 2008.

[20] G. Herrmann, S. S. Ge, and G. Guo, "Practical implementation of a neural network controller in a hard disk drive," *IEEE Transactions on Control Systems Technology*, vol. 32, no. 4, pp. 146–154, 2005.

[21] G. Herrmann, S. Ge, and G. Guo, "A neural network controller augmented to a high performance linear controller and its application to a HDD-track following servo system," in *Proceedings of the 16th IFAC World Congress*, Prague, Czech Republic, 2005.

[22] Y.-C. Chang, "Adaptive fuzzy-based tracking control for nonlinear SISO systems via VSS and H_∞ approaches," *IEEE Transactions on Fuzzy Systems*, vol. 9, no. 2, pp. 278–292, 2001.

[23] B.-S. Chen, C.-H. Lee, and Y.-C. Chang, "H_∞ tracking design of uncertain nonlinear SISO systems: adaptive fuzzy approach," *IEEE Transactions on Fuzzy Systems*, vol. 4, no. 1, pp. 32–43, 1996.

[24] N. Aramcibia, T. Tsao, and S. Gibson, "Adaptive tuning and control of a hard disk drive," in *Proceedings of the American Control Conference*, New York, USA, 2007, pp. 1526–1530.

[25] H. Taghirad and E. Jamei, "Robust performance verification of adaptive robust controller for hard disk drives," *IEEE Transactions on Industrial Electronics*, vol. 55, no. 1, pp. 448–456, 2008.

[26] D. Wu, G. Guo, and T.-C. Chong, "Adaptive compensation of microactuator resonance in hard disk drives," *IEEE Transactions on Magnetics*, vol. 36, no. 5, pp. 2247–2250, 2000.

[27] K. Ohno and T. Hara, "Adaptive resonance mode compensation for hard disk drives," *IEEE Transactions on Industrial Electronics*, vol. 53, no. 2, pp. 624–630, 2006.

[28] C. I. Kang and C. H. Kim, "An adaptive notch filter for suppressing mechanical resonance in high track density disk drives," *Microsystem Technologies*, vol. 11, pp. 638–652, 2005.

[29] K. P. Tee, S. S. Ge, and E. H. Tay, "Adaptive resonance compensation for hard disk drive servo systems," in *Proceedings of the 46th IEEE Conference Decision and Control*, New Orleans, LA, 2007, pp. 3567–3572.

[30] G. Franklin, J. Powell, and M. Workman, *Digital control of dynamic systems.* Reading, Mass.: Addsion-Wesley Publishing Company, 1990.

[31] H. Ho, "Fast servo bang-bang seek control," *IEEE Transactions on Magnetics*, vol. 33, no. 6, pp. 4522–4527, Nov. 1997.

[32] G. X. Guo, T. Huang, K. Tay, S. Weerasooriya, and A. Al-Mamun, "A DSP based hard disk drive servo test stand," *IEEE Transactions on Magnetics*, vol. 34, no. 2, pp. 480–482, March 1998.

[33] S. Hara, T. Hara, L. Yi, and M. Tomizuka, "Novel reference signal generation for two-degree-of-freedom controllers for hard disk drives," *IEEE/ASME Transactions on Mechatronics*, vol. 5, no. 1, pp. 73–78, March 2000.

[34] L. Yi and M. Tomizuka, "Two-degree-of-freedom control with robust feedback control for hard disk servo systems," *IEEE/ASME Transactions on Mechatronics*, vol. 4, no. 1, pp. 17–24, March 1999.

[35] S. Nakagawa, T. Yamaguchi, I. Fujimoto, Y. Hori, Y. Ito, and Y. Hata, "Multi-rate two-degree-of-freedom control for fast and vibration-less seeking of hard disk drives," in *Proceedings of the American Control Conference*, Arlington, VA, June 2001, pp. 2797–2802.

[36] A. Al-Mamun, T. Suthasun, and T. H. Lee, "Simplified multi-rate control for reduced residual vibration - frequency domain analysis," in *Proceedings International Conference on Measurement and Control*, Pittsburgh, USA, May 2001.

[37] S. Zeng, R. Lin, and L. Xu, "Novel method for minimizing track seeking residual vibrations of hard disk drives," *IEEE Transactions on Magnetics*, vol. 37, no. 3, pp. 1146–1156, May 2001.

[38] D. Oh, S. Lee, and S. Baek, "Adaptive feedforward rejection of microactuator resonance in disk drive dual-stage actuator servo," in *Asia-Pacific Magnetic Recording Conference*, Singapore, 2000, pp. TP11, 1–2.

[39] N.-C. P. Dong-Woohn Kim, Jin Koo Lee and Y. P. Park, "Vibration analysis of HDD actuator with equivalent finite element model of vcm coil," *Journal of Mechanical Science and Technology*, vol. 17, no. 5, pp. 679–690, 2003.

[40] L. Guo and Y. Chen, "Disk flutter and its impact on HDD servo performance," *IEEE Transactions on Magnetics*, vol. 37, no. 2, pp. 866–870, 2001.

[41] G. Guo and J. Zhang, "Feedforward control for reducing disk-flutter-induced track misregistration," *IEEE Transactions on Magnetics*, vol. 39, no. 4, pp. 2103–2108, 2003.

[42] Trendfocus, "Annual trendfocus report," *http://www.trendfocus.com*, 2008.

[43] R. Evans, J. Griesbach, and W. Messner, "Piezoelectric microactuator for dual-stage control," *IEEE Transactions on Magnetics*, vol. 35, no. 2, pp. 977–982, 1999.

[44] Y. Chen, K. Moore, J. Yu, and T. Zhang, "Iterative learning control and repetitive control in hard disk drive industry - a tutorial," in *Proceedings of the 2006 IEEE International Conference on Decision and Control*, San Diego, USA, 2006, pp. 1–15.

[45] J. L. Zhang, S. Weerasooriya, T. Huang, and T. S. Low, "Modified AFC runout cancellation and its influence on track following," in *Proceedings of the International Conference on Industrial Electronics, Control and Instrumentation*, Japan, 1997, pp. 35–40.

[46] A. Sacks, M. Bodson, and W. Messner, "Advanced methods for repeatable runout compensation," *IEEE Transactions on Magnetics*, vol. 31, no. 2, pp. 1031–1036, 1995.

[47] R. Ehrlich and D. Curran, "Major HDD TMR sources and projected scaling with TPI," *IEEE Transactions on Magnetics*, vol. 35, no. 2, pp. 885–891, 1999.

[48] G. F. Franklin, J. D. Powell, and A. Emami-Naeini, *Feedback Control of Dynamic Systems*, 4th ed. Upper Saddle River, NJ: Prentice Hall, 2002.

[49] V. Venkataramanan, B. Chen, T. Lee, and G. Guo, "A new approach to the design of mode switching control in hard disk drive servo systems," *Control Engineering Practice*, vol. 10, no. 9, pp. 925–939, 2002.

[50] P. Meckel and K. Kudo, "Input shaping technique of reduce vibration for disk-drive heads," *ASME, Advances in Information Storage Systems*, vol. 5, pp. 45–58, 1993.

[51] Y. Mizoshita, S. Hasegawa, and K. Takaishi, "Vibration minimized access control for disk drives," *IEEE Transactions on Magnetics*, vol. 32, no. 3, pp. 1793–1798, 1996.

[52] D. K. Miu and S. P. Bhat, "Minimum power and minimum jerk position control and its applications in computer disk drives," *IEEE Transactions on Magnetics*, vol. 27, no. 6, pp. 4471–4475, 1991.

[53] B. Schardt and E. Schreck, "Flying height measurement while seeking in hard disk drives," *IEEE Transactions on Magnetics*, vol. 34, pp. 1765–1767, 1998.

[54] L. Guo, J. Chang, and X. Hu, "Track-following and seek/settle control schemes for high density disk drives with dual-stage actuators," in *Proceedings IEEE/ASME International Conference Advanced Intelligent Mechatronics*, Como, Italy, 2001, pp. 1136–1141.

[55] M. Kobayashi and R. Horowitz, "Track seek control for hard disk dual-stage servo systems," *IEEE Transactions on Magnetics*, vol. 37, no. 2, pp. 949–954, 2001.

[56] G. X. Guo, Q. Hao, and T. S. Low, "A dual-stage control design for high track per inch hard disk drives," *IEEE Transactions on Magnetics*, vol. 37, no. 2, pp. 860–865, 2001.

[57] M. Kobayashi, S. Nakagawa, and S. Nakamura, "A phase-stabilized servo controller for dual-stage actuators in hard disk drives," *IEEE Transactions on Magnetics*, vol. 39, no. 2, pp. 844–850, 2003.

[58] Z. M. Li, K. X. Liu, B. M. Chen, and T. H. Lee, "Robust and perfect tracking control design of a hard disk drive with a dual-stage actuator," in *Proceedings of the American Control Conference*, Arlington, VA, 2001, pp. 3849–3854.

[59] T. Yamaguchi, Y. Soyama, H. Hosokawa, K. Tsuneta, and H. Hirai, "Improvement of settling response of disk drive head positioning servo using mode switching control with initial value compensation," *IEEE Transactions on Magnetics*, vol. 32, no. 3, pp. 1767–1772, 1996.

[60] T. Yamaguchi, K. Shishida, S. Tohyama, and H. Hirai, "Mode switching control design with initial value compensation and its application to head positioning control on magnetic disk drives," *IEEE Transactions on Industrial Electronics*, vol. 43, no. 1, pp. 65–73, 1996.

[61] W. Singhose, W. Seering, and N. Singer, "Residual vibration reduction using vector diagrams to generate shaped inputs," *ASME Journal of Mechnical Design*, vol. 116, pp. 654–659, 1994.

[62] T. Singh and W. Singhose, "Tutorial on input shaping/time delay control of maneuvering flexible structures," in *Proceedings of the American Control Conference*, Alaska, USA, 2002, pp. 1717–1731.

[63] T. Yamaguchi, "A mode-switching controller with initial value compensation for hard disk drive servo control," *Control Engineering Practice*, vol. 5, no. 11, pp. 1525–1532, 1997.

[64] M. Tomizuka, "Zero phase error tracking algorithm for digital control," *ASME Journal of Dynamic Systems, Measurement, and Control*, vol. 109, pp. 65–68, 1987.

[65] A. Rantzer, "On the Kalman-Yakubovic-Popov lemma," *Systems and Control Letter*, vol. 28, no. 1, pp. 7–10, 1996.

[66] T. Iwasaki, G. Meinsma, and M. Fu, "Generalized S-procedure and finite frequency KYP lemma," *Mathematical Problems in Engineering*, vol. 6, pp. 305–320, 2000.

[67] S. Boyd and C. H. Barratt, *Linear Controller Design: Limits of Performance*. Eaglewood Cliffs: Prentice Hall, 1991.

[68] B. A. Francis and J. C. Doyle, "Linear control theory with an H_∞ optimality criteron," *SIAM Journal on Control and Optimization*, vol. 25, pp. 815–844, 1987.

[69] K. Zhou and J. C. Doyle, *Essentials of Robust Control*. Prentice Hall Inc., 1989.

[70] T. Coleman, M. Branch, and A. Grace, *Optimization Toolbox For Use with Matlab*. The MathWorks Inc. Natick, Mass, 1999.

[71] K. Glover, D. J. N. Limebeer, J. C. Doyle, and E. M. Kasenally, "A characterization of all solutions to the four block general distance problem," *SIAM Journal on Control and Optimization*, vol. 27, pp. 283–324, 1991.

[72] A. Saberi, P. Sannuti, and B. Chen, *H_2 Optimal Control*. Prentice-Hall, Englewood Cliffs, NJ, 1995.

[73] M. C. de Oliviera, J. Geromel, and J. Bernussou, "An LMI optimization approach to multiobjective controller design for discrete-time systems," in *Proceedings of the 38th IEEE Conference Decision and Control*, Phoenix, AZ, 1999, pp. 3611–3616.

[74] H. Ho and T. Doan, "Distortion effects on servo position error transfer function," *IEEE Transactions on Magnetics*, vol. 33, no. 4, pp. 2569–2572, 1997.

[75] M.-T. Ho, A. Datta, and S. P. Bhattacharyya, "Control system design using low order controllers: constant gain, PI and PID," in *Proceedings of the American Control Conference*, Albuquerque, New Mexico, 1997, pp. 571–578.

[76] Y. Uematsu, M. Fukushi, and K. Taniguchi, "Development of the pushpin free STW," *IEEE Transactions on Magnetics*, vol. 37, no. 2, pp. 964–968, 2001.

[77] M. Schultz, "A self-servowrite clocking process," *IEEE Transactions on Magnetics*, vol. 37, no. 2, pp. 1878–1880, 2001.

[78] K. Takaishi and Y. Uematsu, "Hard disk drive servo technology for media-level servo track writing," *IEEE Transactions on Magnetics*, vol. 39, no. 2, pp. 851–856, 2003.

[79] J. L. Zhang, B. Hredzak, and C. L. Du, "High density servo track writing using two-stage configuration," in *Proceedings of the IEEE International Conference on Control Applications*, Singapore, 2007, pp. 124–129.

[80] G. Guo and J. Zhang, "Control strategies for writing servo tracks narrower than 5 micro inches," in *Proceedings of the of 2003 JSME-IIP/ASME-ISPS Joint Conference on Micromechatronics for Information and Precision Equipment*, Singapore, 2003, pp. 1–5.

[81] B. Hredzak, G. Guo, and J. Zhang, "Investigation of the effect of hard disk drive unbalance on repeatable and non-repeatable runout," in *Proceedings of 2003 IEEE International Conference on Power Electronics and Drive Systemsl*, Singapore, 2003, pp. 1359–1363.

[82] H. Ye, V. Sng, C. Du, J. Zhang, and G. Guo, "Radial error propagation issues in self servo track writing technology," *IEEE Transactions on Magnetics*, vol. 38, no. 5, pp. 2180–2182, 2002.

[83] Y. Li, R. Horowitz, and R. Evans, “Vibration control of a PZT actuated suspension dual-stage servo system using a PZT sensor,” *IEEE Transactions on Magnetics*, pp. 932–937, 2003.

[84] R. Ehrlich, J. Adler, and H. Hindi, “Rejecting oscillatory, non-synchronous mechanical disturbance in hard disk drives,” *IEEE Transactions on Magnetics*, vol. 37, no. 2, pp. 646–650, 2001.

[85] D. Abramovitch, T. Hurst, and D. Henze, “An overview of PES Pareto method for decomposing daseline noise sources in hard disk position error signals,” *IEEE Transactionsctions on Magnetics*, vol. 34, no. 1, pp. 17–23, 1998.

[86] G. Herrmann, S. S. Ge, and G. Guo, “Practical implementation of neural network controller in a hard disk drive,” *IEEE Transactions Control Systems Technology*, vol. 13, no. 1, pp. 146–154, 2005.

[87] S. S. Ge, B. Ren, and T. H. Lee, “Hard disk drive control in mobile applications,” *System Science and Complexity*, vol. 20, pp. 215–225, 2007.

[88] J. Zheng, C. Du, G. Guo, Y. Wang, J. Zhang, Q. Li, and B. Hredzak, “Phase lead peak filter method to high TPI servo track writer with microactuators,” in *Proceedings of the American Control Conference*, Minneapolis, MN, 2006, pp. 1309–1314.

[89] F. Huang, T. Semba, W. Imaino, and F. Lee, “Active damping in HDD actuator,” *IEEE Transactions on Magnetics*, vol. 37, no. 2, pp. 847–849, 2001.